UNIVERSITÉ DU LUXEMBOURG

PhD-FSTM-2022-117
The Faculty of Science, Technology
and Medicine

DISSERTATION

Presented on 15/09/2022 in Esch-sur-Alzette
to obtain the degrees of

DOCTEUR DE L'UNIVERSITÉ DU LUXEMBOURG EN SCIENCES DE L'INGÉNIEUR

by

Sofia FARINA
born on September 5th 1992 in Bologna, Italy

Modelling Astrocytic Metabolism in Actual Cell Morphologies

Dissertation defence committee:

Dr Olivier Francis, Chairman
Professor, University of Luxembourg

Dr Alexander Skupin, Vice Chairman
Professor, University of Luxembourg

Dr Stéphane P. A. Bordas, dissertation supervisor
Professor, University of Luxembourg

Dr Padmini Rangamani, member
Professor, University of California San Diego

Dr Kevin Thurley, member
Professor, University of Bonn

Declaration

I hereby declare that, the contents and organization of this dissertation constitute my own original work and does not compromise in any way the rights of third parties, including those relating to the security of personal data.

Sofia Farina, Friday 7th October, 2022

"Nature is written in mathematical language."
Galielo Galilei

Acknowledgements

The word philosophy originates from ancient Greek from φίλος (*phílos*) "beloved" and σοφία (*sophía*) "wisdom", thus love for wisdom. Literally, this Ph.D. journey is about my love for wisdom and self-love.

First, I have to thank my supervisor, Stéphane, who gave me the chance to follow this journey. Since day one, he showed me constant support and excitement for the project. I am so thankful and grateful to him for having gifted me with the chance to work here and doing what I love. His energy and thirst for knowledge was really inspiring.

Second, I want to thank my co-supervisor, Alex. He welcomed me in the biomedical world, teaching me and making me part of the team. I enjoyed our weekly meetings, and he was always patient and kind in explaining to me. He encouraged me with positive feedback even when the results weren't great. I am very thankful to have had the possibility to learn from him.

I thank my jury members. Thanks to Professor Padmini Rangamani and Professor Kevin Thurley for being my external examiners and taking their time to read my work. A special thank goes to Professor Olivier Francis for being the chairman of my jury but, mostly, for all his jokes that made these four years run faster.

In particular, I thank Jack, Susanne and Valérie. Thanks to Jack for all his help and fruitful discussions. Thanks to Susanne for being part of my CET and all her help and kindness. Thanks to Valérie, because I haven't only found a great researcher but also a dear friend.

A journey without companions is definitely much harder, and I had the luck to have not one but two teams to count on. Thanks to Legato team for sharing all these years in the office, Friday nights and Halloween parties. I have found wonderful people who made the rainy days of Luxembourg more bearable. Thanks to Arnaud, Hussein, Paul, Pratik, Raphaël, Saurabh, Chintan, Jakub, Anas, Stéphane, Henry, Marie, and all the others. Thanks to ICS team for welcoming me and sharing all the group meetings, retreats, bowling and BBQ. Thanks to Sonja, Silvia, Michela, Thais, Corrado, Cristina, Françoise, Melanie, Dimi and all the others.

I also want to thank all the friends I encountered in Luxembourg and supported me. Thanks to Anita, for all the breaks, to Benjamin, for climbing and, to Giuseppe, for the endless chat.

I had the luck to receive love and support from many countries. I thank my best friend, Giacomo, who told me long time ago to embrace my pace. Of course, I didn't listen. Of course, he was right. Thanks to Lucia, she was really a life saviour in the first period of the PhD. Thanks to Ginevra, Marco, Angela, Camilla, Giovanna, Isabella, Alessandra. Thanks to all other friends, past and present, that I did not mention if I am here is also thanks to them. Thanks to all my friend from Asclepios: Yann, Manon, Wen, Cici, Shuman, Raphael, Pawel; knowing you inspired me to start this journey.

Thanks to my family-in-lay, Dagmar, Dieter and Janina, for welcoming me in their family.

Thanks to my family. Thanks to my Dad, Roberto, my brother, Luca, my mum, Chiara, my aunt, Dada, my uncle, Stefano and my beloved Nonna.

Last, and above all, thanks to my future husband, Julian. I am immensely gratitude to have met him. He believed in me, supported me all these years. He was patient and loving and helped me to overcome obstacles. He was by my side all along in bad and good times. He is the most kind hearted, caring,

loving, independent and reliable partner. It's thanks to him if this journey is also about love.

Financial Support

This work is part of the Doctoral Training Unit Data-driven computational modelling and applications (DRIVEN) funded by the Luxembourg National Research Fund under the PRIDE programme (PRIDE17/12252781).

Abstract

The human brain is the most structurally and biochemically complex organ, and its broad spectrum of diverse functions is accompanied by high energy demand. In order to address this high energy demand, brain cells of the central nervous system are organised in a complex and balanced ecosystem, and perturbation of brain energy metabolism is known to be associated with neurodegenerative diseases such as Alzheimer's (AD) and Parkinson's disease. Among all cells composing this ecosystem, astrocytes contribute metabolically to produce the primary energy substrate of life, ATP, and lactate, which can be exported to neurons to support their metabolism. Astrocytes have a star-shaped morphology, allowing them to connect on the one side with blood vessels to uptake glucose and on the other side with neurons to provide lactate. Astrocytes may also exhibit metabolic dysfunctions and modify their morphology in response to diseases. A mechanistic understanding of the morphology-dysfunction relation is still elusive. This thesis developed and applied a mechanistic multiscale modelling approach to investigate astrocytic metabolism in physiological morphologies in healthy and diseased human subjects.

The complexity of cellular systems is a significant obstacle in investigating cellular behaviour. Systems biology tackles biological unknowns by combining computational and biological investigations. In order to address the elusive

connection between metabolism and morphology in astrocytes, we developed a computational model of central energy metabolism in realistic morphologies. The underlying processes are described by a reaction-diffusion system that can represent cells more realistically by considering the actual three-dimensional shape than classical ordinary differential equation models where the cells are assumed to be spatially punctual, i.e. have no spatial dimension. Thus, the computational model we developed integrates high-resolution microscopy images of astrocytes from human post-mortem brain samples and simulates glucose metabolism in different physiological astrocytic human morphologies associated with AD and healthy conditions.

The first part of the thesis is dedicated to presenting a numerical approach that includes complex morphologies. We investigate the classical finite element method (FEM) and cut finite element method (CutFEM) for simplified metabolic models in complex geometries.

Establishing our image-driven numerical method leads to the second part of this thesis, where we investigate the crucial role played by the locations of reaction sites. We demonstrate that spatial organisation and chemical diffusivity play a pivotal role in the system output. Based on these new findings, we subsequently use microscopy images of healthy and Alzheimer's diseased human astrocytes to build simulations and investigate cell metabolism.

In the last part of the thesis, we consider another critical process for astrocytic functionality: calcium signalling. The energy produced in metabolism is also partially used for calcium exchange between cell compartments and mainly can drive mitochondrial activity as a main ATP generating entity. Thus, the active cross-talk between glucose metabolism and calcium signalling can significantly impact the metabolic functionality of cells and requires deeper investigation. For this purpose, we extend our established metabolic model by a calcium signalling module and investigate the coupled system in two-dimensional geometries.

Overall, the investigations showed the importance of spatially organised metabolic modelling and paved the way for a new direction of image-driven-meshless modelling of metabolism. Moreover, we show that complex morphologies play a crucial role in metabolic robustness and how astrocytes' morphological changes to AD conditions lead to impaired energy metabolism.

Contents

Abbreviations

Concentrations

GLC Glucose

ATP Adenosine triphosphate

FUM Fumarate

ISOC Isocitrate

MAL Malate

NADH Nicotinamide adenine dinucleotide reduced

NAD Nicotinamide adenine dinucleotide oxidised

OAA Oxaloacetate

SCoA Succinyl-coenzyme A

SUC succinate

ADP Adenosine diphosphate

GLY Glyceraldehyde 3-phosphate

PYR Pyruvate

LAC Lactate

Ca^{2+} Calcium

AcCoA Acetyl coenzyme A

αKG α-ketoglutarate

CIT Citrate

Reactions

HXK hexokinase, phosphoglucose isomerase, phosphofructose kinase and the fructose bisphosphate aldolase

PYRK glyceraldehyde phosphate dehydrogenase, phosphoglycerate kinase, phosphoglycerate mutase, enolase and the pyruvate kinase

SL Succinyl-coenzyme A Synthetase

SDH Succinate dehydrogenase

FH Fumarate hydratase

MDH Malate dehydrogenase

OX Oxidative phosphorylation

ANT Adenine nucleotide translocator

ERout IP_3 receptors and leakage from ER

SERCA Ca^{2+}-ATPase pump

NCX Sodium-calcium exchanger

MCU Mitochondrial calcium uniporter

Mito TCA cycle and oxidative phosphorylation activity

Hyd ATP hydrolysis

CS Citrate synthase

LDH Lactate dehydrogenase

act ATP-consuming cellular activity

PyrEx Pyruvate exchange

pdh pyruvate dehydrogenase complex

ACO Aconitase

IDH Isocitrate dehydrogenase

KGDH α-ketoglutarate dehydrogenase

Math Symbols

$[\cdot]$ Concentration

$\mathcal{G}_{\cdot}$ Gaussian function

$\mathcal{K}_{\cdot}$ Spatial reaction rate

Ω Domain

$D_{[\cdot]}$ Diffusion coefficient

$K_{\cdot}$ Reaction rate

Other Symbols

$\Delta\psi$ Membrane potential

CutFEM Cut Finite Element Method

PDEs Partial Differential Equations

CNS Central Nervous System

GFAP Glial fibrillary acidic protein

ODEs Ordinary Differential Equations

OXPHOS oxidative phosphorylation

CHAPTER 1

Introduction

Alzheimer's disease (AD) is a age-associated progressive neurological disorder and the most predominant cause of dementia. As a consequence of the population ageing, the expected number of people affected by AD is forecast to increase to approximately 135 million world-wide in 2050 [49] compared to 43.8 million [163] in 2016. Dementia is the main symptom of people suffering from neurodegenerative diseases, including AD, causing memory loss and learning difficulties. Due to neurological effects, these diseases will have an impact not only on public health but also on the families of patients, placing the utmost importance on research in this field.

There are many unknowns on neurodegenerative diseases. Mechanisms in our brain get dysfunctional, leading to neuronal death, which is the underlying cause of dementia. Typically, a brain suffering from neurodegeneration exhibits an altered level of metabolic energy [172]. Energy is our brain's fuel, and cellular metabolism is the brain's energetic supply. Therefore, it is fundamental to investigate the metabolic behaviour of brain cells in neurodegeneration and when and how it plays a role in disease development.

The complexity of the brain requires researchers from different fields to collaborate to unravel its mystery. Thus, scientists with different backgrounds,

including biologists, computer scientists, statisticians, physicians and mathematicians, merge their knowledge to support scienctific advancements. As a mathematician, my contribution to the field lies in creating computational models which help to investigate biological mechanisms by *in silico* experiments.

In this first chapter, we introduce the motivation and objectives of this work. First, we discuss the fundamental role of metabolism in the brain, which can be disrupted in neurodegenerative diseases. Subsequently, we present Systems Biology as an approach to study these diseases by bridging different disciplines. Next, we motivate and develop the overarching research question aimed at addressing the main objectives of this thesis:

What is the relationship between morphology and metabolic dysfunctions in astrocytes affected by neurodegenerative diseases?

Last, we present the structure of the manuscript and the scientific contributions of this thesis to the community.

1.1 Motivation

Metabolism is the process that transforms nutrients into usable energy in living organisms. It is fundamental for life. At rest, our brain consumes most of the energy produced by cellular metabolism [132]. Ideally, the cells composing our central nervous system (CNS) live in a perfectly balanced ecosystem where each cell contributes to the well-being of the brain through its functionality and interdependence. Fundamental to the brain's energetic symphony are astrocytes [210], a type of glial cells which are metabolic mediators between neurons and the blood vessels. More precisely, the metabolism of neurons is tied to the lactate supply function of astrocytes [175]. However, in the case of neurodegenerative diseases, the harmony of this ecosystem is undermined. Cells display dysfunctional behaviour, including metabolic dysfunctions. For example, in Alzheimer's Disease (AD), energy production is impaired [34], and thus, the brain is in energy deficiency.

Typically, neurodegenerative diseases are hard to detect initially, and the diagnosis often comes when dementia is already in a moderate state. Dementia is associated by loss of brain tissue that looks atrophied. Under the microscope,

a lower number of neurons is visible compared to a healthy sample. For decades, the investigation of neurodegenerative diseases has been neuron-centric and only recently the focus has moved to other cell types, such as astrocytes. There are still many unknowns in the genesis and development of these diseases and the potential toxicity or rescuing contribution of different cell types. The mystery of these open questions brings researchers from different disciplines to collaborate to tackle the unknowns from different angles.

Systems Biology [128] is an interdisciplinary subject born in the early 2000s that combines experimental data, computational techniques, and mathematical tools to investigate biological phenomena. Mathematical models describe physical processes by equations. An example of a famous mathematical model in biology is the Hodgkin-Huxley model, representing the action potential in neurons which received the Nobel prize in 1963 [115]. The strength of these models lies in simplifying reality and focusing only on the main features. This helps to understand complex biological systems including individual cells that orchestrate all their functionality simultaneously.

Most previously proposed dynamic metabolic models describe the process in time as uni-dimensional through sets of ordinary differential equations (ODE) [16, 15, 71]. Since metabolism is a fast process with typical timescales of seconds to a few minutes, an ODE system can represent an excellent approximation to describe the fast change in the average concentration of the metabolites, and more or less detailed models can describe the metabolic process of cells. However, it might be a limitation to describe a complex system in time without considering the complex domain of the cell. Hence, it might be more suitable to describe them by reaction-diffusion systems since it automatically includes the spatial domain in more than one spatial dimension. The direction of the next generation of metabolic models intends to describe the chemical reactions as a function of space and time, thus, incorporating geometrical information. Cellular geometries have probably developed during evolution into shapes optimised for their functionality. Geometric-based models might help to address the unexplained role of morphological changes in astrocytes in neurodegeneration [42]. Such approaches may provide the research community with models closer to reality, which would not be possible without the progress made in the computational community with the advent of powerful computers and new computational techniques enabling the simulation of complex models.

This thesis was born as an interdisciplinary project between two research teams at the University of Luxembourg (UL), the Integrative Cell Signalling group of Luxembourg Centre for Systems Biomedicine and the Department of Engineering. This work focuses on astrocytes that have become a centre of attention for their many functionalities and morphology in recent years. The goal of this thesis is to investigate the relationship between cellular morphology and metabolism in AD through computational modelling. The project aims to combine the scientific resources within the two groups involved in bridging the knowledge on solving partial differential equations with finite element methods in systems biology.

1.2 Objectives

Astrocytes, as metabolic supporters, provide neurons with lactate as energy substrate. They have a very complex and ramified morphology that undergoes significant changes in the presence of neurodegenerative diseases. This thesis aims to examine astrocytic morphologies in neurodegeneration linked to their role as metabolic supporters for neurons. The goal is to obtain a mechanistic model of glucose metabolism, which is solved spatially in complex geometries. To achieve this objective, we developed a model that describes the principal pathways of cellular metabolism as a reaction-diffusion system. Thus, we take into account more than one spatial dimension. For this purpose, we first address the research question (Chapter 3): Which computational approach is best suited to deal with the complex morphologies of cells directly from cellular images and keeping stability and robustness in focus?

In the second part (Chapter 4), we investigate the system's behaviour by addressing the questions: how relevant are the spatial organisation of reaction sites inside the cell and different geometries for the output of the metabolic system? How is the physiological morphology of astrocytes relevant to their metabolic role? How can our model be used in physiological geometries to study neurodegeneration in AD?

In the last part, we investigate calcium signalling as a fundamental process for astrocytic communication and coupling with glucose metabolism as the main contributor to cellular energy. Therefore, the last question we start to

investigate in this work (Chapter 5) is: what is the interplay between glucose metabolism and calcium signalling in a spatially resolved domain of a cell?

1.3 Thesis Structure

Chapter 2 presents the interdisciplinary scientific background where we introduce the biological context, the state-of-the-art in systems biology with required modelling instruments and an overview of numerical methods to solve such models.

In Chapter 3, we introduce a spatially resolved metabolic model described by a reaction-diffusion system. Although our metabolic processes are more coarse-grained than models presented in literature [71], we capture the primary metabolic process by a simple mathematical formulation. The strength of our model is the possibility of focusing on the relationship between metabolism and cellular morphologies. To address the challenge of using complex geometries as the domain for the model, we investigate a numerical approach to solve it within complex morphologies of cells. The cut finite element method (CutFEM) proposed by Hansbo [111] and Burman [58] can disentangle the geometry from the finite element mesh. Hence, we compare the classic finite element method with the cut finite element method for our reaction-diffusion system. Our results show the ability of CutFEM to incorporate complex geometries while ensuring the same results as classic FEM. Moreover, we provide an open-source code that is easily accessible to a non-expert. This chapter was published as a journal article in AMSES [97].

Chapter 4 presents a detailed investigation of how the spatial orchestration of enzymatic sites inside cells and different geometries impact the dynamics of the metabolic system. Our results in two dimensions highlight the relevance of refining the next generation of metabolic models with spatial orchestration. Next, we show how to incorporate confocal microscopic cellular images to define the simulation domain. Last, we investigate Alzheimer's Disease related metabolic dysfunctionality in authentic astrocytic human morphologies. Our results suggest the fundamental role of astrocytic geometries in enhancing the robustness of the system. The work presented in this chapter is part of our article under review [99].

In Chapter 5, we incorporate a calcium-signalling model [225] into the metabolic model presented before. The coupling of these two models aims to investigate the impact of calcium signalling on the cellular energetic state and lactate production in a spatially resolved model. We investigate the coupled model in two dimensional domains. Our preliminary results show the stabilizing effect of the calcium regulation on the metabolic profiles and the crucial role of chemical diffusion as a buffering effect.

Last, we discuss and summarise the results obtained from the different chapters in Chapter 6, and conclude by discussing possible future directions.

1.4 Publications

My project has led to the following scientific contributions.

Articles

Peer reviewed Journal article:

- Farina, S., Claus, S., Hale, J. S., Skupin, A., and Bordas, S. (2021). A cut finite element method for spatially resolved energy metabolism models in complex neuro-cell morphologies with minimal remeshing. *Advanced Modeling and Simulation in Engineering Sciences*, 8(1):1–32

Submitted pre-prints:

- Farina, S., Voorsluijs, V., Fixemer, S., Bouvier, D., Claus, S., Bordas, S., and Skupin, A. (2022b). Mechanistic multiscale modelling of energy metabolism in human astrocytes indicates morphological effects in alzheimer's disease. (Under review)

In preparation:

- Farina, S.,*et. al.* (2022). Astrocytic metabolism and calcium signalling cross-talk in a spatially resolved model. (In preparation)

Conferences

Presentations as speaker:

- Farina, S., Claus, S., Hale, J. S., Komin, N., Skupin, A., and Bordas, S. (2020). A cutfem method for a spatially resolved energy metabolism model in complex cellular geometries. WCCM
- Farina, S., Voorsluijs, V. e., Claus, S., Skupin, A., and Bordas, S. (2022c). A cutfem method for a mechanistic modeelling of astrocytic metabolsim in 3d physiological morphologies. ECCOMAS
- Farina, S., Voorsluijs, V., Fixemer, S., Bouvier, D., Claus, S., Bordas, S., and Skupin, A. (2022a). 3d modelling of a spatially resolved energy metabolism in physiological astrocytic morphology. ECMTB

Invited Talks

- Farina, S. (2022) A mechanistic multiscale metabolic model in human astrocytes. EMIx Workshop , Simula Lab, Oslo (Norway).

CHAPTER 2

Scientific Background

This chapter is devoted to the interdisciplinary scientific background of the work presented in this thesis. First, we give the biological context by introducing astrocytes, their functions, and their central role in neurodegenerative diseases. To investigate the unknown mechanisms in biology, we present subsequently the recent interdisciplinary approach of systems biology. After discussing the state of the art in modelling metabolism and calcium, we give some of the fundamental tools used for modelling. Last, we discuss different numerical techniques to solve such models.

2.1 Astrocytes

The fundamental units of our central nervous system (CNS) are neurons. They have the role of transmitting information through the whole body by communicating with each other. A neuron communicates with another via action potential (electrical signals) and chemical messengers exchanged in the synapses. However, the CNS is composed not only of neurons but mostly of glial cells. The most abundant glial cells are multitasking cells, named

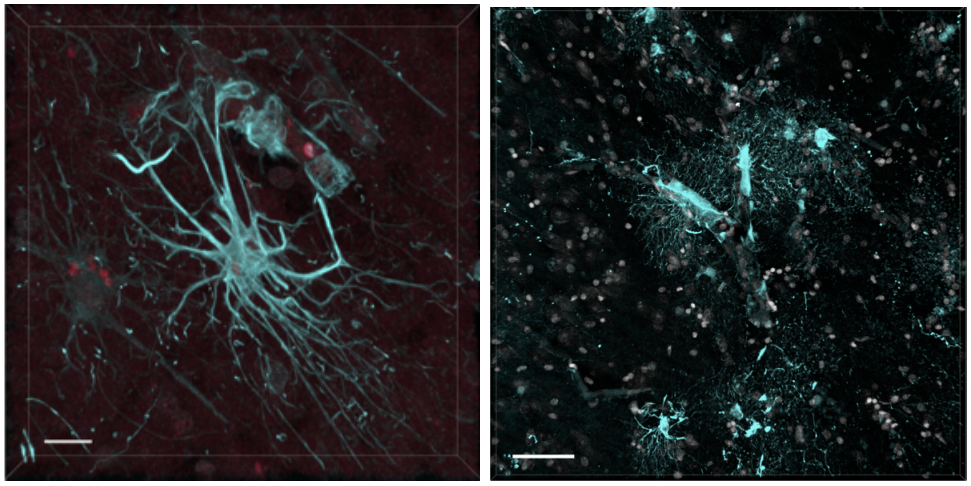

Fig. 2.1 Confocal microscopic images taken from a human CA1 hippocampus. (Left) Protoplasmic astrocyte stained with GFAP. Scalebar: $15\mu m$ (Right) Fibrous astrocytes stained with GFAP. Scalebar: $20\mu m$ (Images provided by Sonja Fixemer).

astrocytes [210] (Figure 2.1). Their name refers to their particular star-like shape and was given in 1895 by the anatomist Mihály Lenhossék. Astrocytes are a very heterogeneous group of cells that can be divided into subgroups depending on the brain region and exhibit a brain location-dependent density [224]. They display multiple processes, the density of which helps differentiate between different classes of astrocytes. The two main sub-classes are *protoplasmic* and *fibrous* astrocytes, which differ by anatomical location and morphologies. Protoplasmic astrocytes (Figure 2.1) are found in the grey matter and have a very high density of long processes [59]. Fibrous astrocytes (Figure 2.1) are located in the white matter and exhibit a lower branch density than the protoplasmic astrocytes. Furthermore, protoplasmic astrocytes' processes enwrap synapses, while fibrous' ones typically contact Nodes of Ranvier, which are spots on the axon where the insulating myelin layer is interrupted. Both kinds of astrocytes have thin processes that make contact with blood vessels.

For completeness, we also mention the existence of other sub-groups as the *interlaminar* astrocytes, characterised by a vertical cable that originates in layer one of the cerebral cortex and extends in layers three-four, and *varicose* astrocyte similar to the interlaminar with long feet but present in layer five-six.

Each astrocyte has its spatial domain [60], and they are linked to each other through gap junctions, forming an intricate, interconnected network

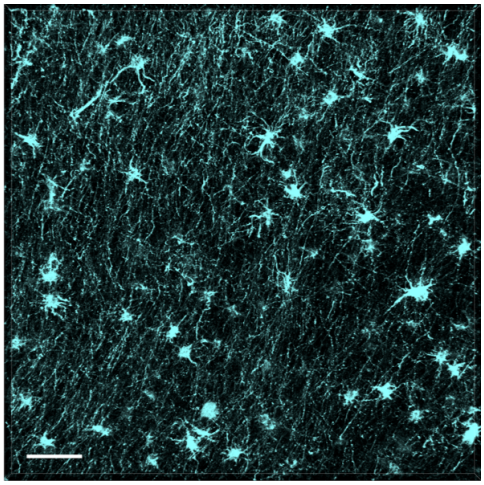

Fig. 2.2 Confocal microscopic image of human protoplasmic astrocytes from a Lewy body patient taken from CA1 hippocampus stained with GFAP. Scalebar: $50\mu m$ (Image provided by Sonja Fixemer).

(Figure 2.2). A single protoplasmic astrocyte has five to ten stem branches, each of which has fine processes that spread through the astrocytic spatial domain and can contact over 100,000 synapses [109].

2.1.1 Functions

Astrocytes have many functions strictly linked to their morphology and intermediate location between neurons and blood vessels (Figure 2.3). For example, they can regulate blood flow by increasing or decreasing blood vessel diameters [106, 118]. They promote the blood-brain barrier (BBB) [237, 91] preventing the spread of harmful substances inside the brain.

In development, astrocytes guide the migration of developing axons [184] and developing synapses [66]. After the establishment of the brain, they contribute essentially to brain homeostasis, including the ion balance in the brain. In particular, since they are in contact with synapses, they are fundamental in regulating the concentration of $[K^+]$ which may accumulate in the extracellular space after the occurrence of an action potential [228]. In relationship with the synaptic activity, there is active bi-directional communication between astrocytes and neurons during the neuronal activity, which led to the definition of the tripartite synapses [177]. Astrocytes communicate with cytosolic calcium

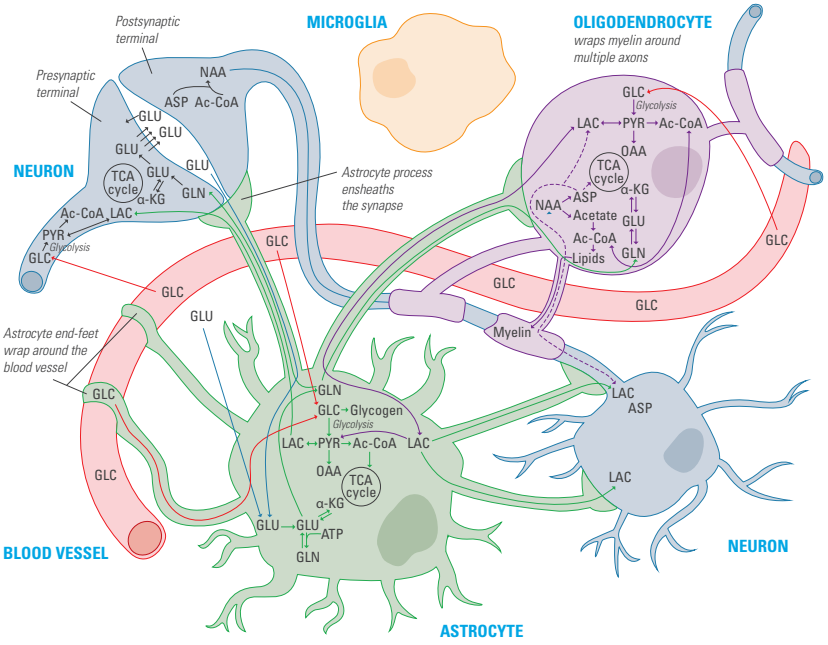

Fig. 2.3 Representation of the metabolic relationship of an astrocyte (green), blood vessel (red), oligodendrocyte (purple) and neurons (blue). (Image provided by Michela Bernini and Melanie Sengupta)

changes as discussed later (Section 2.1.4). In the presence of synaptic activity, astrocytes display cytosolic calcium elevation. Through these changes in calcium, they can detect neurotransmitters released from the neuron and release their neurotransmitters or gliotransmitters, which can then modify the electrophysiological excitability of neurons [176]. This definition adds astrocytes as crucial players in transmitting information between neurons.

Furthermore, their location between neurons and blood vessels is fundamental to neuronal metabolic processes [24] (Figure 2.3). Astrocytic metabolism is crucial for the neuronal one, coupling even more tightly the astrocytic-neuron relationship. They take up glucose from blood vessels and metabolise it by glycolysis. The main product of glycolysis is pyruvate which is either consumed by the enzyme lactate dehydrogenase (LDH) to produce lactate or transported into mitochondria. Inside the mitochondria, the tricarboxylic acid (TCA) cycle and Oxidative Phosphorylation (OXPHOS) produce the main energetic resource of the cell: ATP. On the other hand, lactate produced can be provided to neurons. This process is known as the astrocyte-neuron lactate shuttle (ANLS) [175].

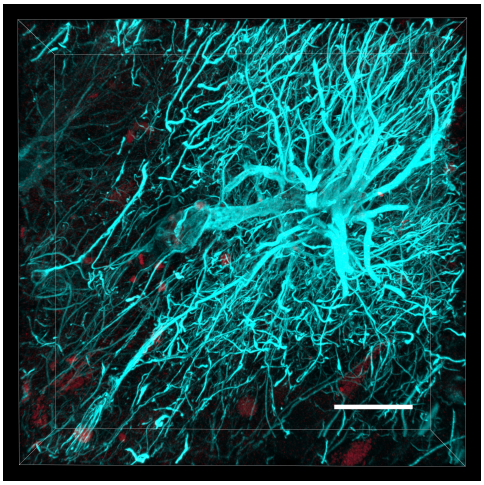

Fig. 2.4 Confocal microscopic image of a reactive protoplasmic astrocyte in Alzheimer's Disease acquired from CA1 subregion of a human hippocampus. Scalebar: $30\mu m$ (Image provided by Sonja Fixemer).

Whereas both neurons and astrocytes perform metabolism, due to the high energy demand, neuronal metabolism relies more on the more efficient mitochondrial mechanisms of the TCA cycle and OXPHOS. Thus, neuronal metabolism is more oxygen-dependent. On the other hand, astrocytes rely more on glycolysis to produce ATP [220, 197]. Moreover, astrocytes store part of the glucose as glycogen and represent the biggest glycogen storage in the brain [51, 50]. Glycogen is a polysaccharide of glucose which can be used to produce lactate required for neurons or their maintenance.

All the mentioned functions clearly establish the centrality of these cells for the homeostasis of the brain and neurons.

2.1.2 Reactivity

In the presence of injuries, pathological conditions or perturbations in cellular homeostasis, astrocytes respond with a "reactive" profile [94] presenting morphological, molecular and functional changes (Figures 2.2 and 2.4). This cellular response is visible in most brain disorders like neurodegenerative diseases, epilepsy, and brain cancer.

However, reactive astrocytes exhibit a different range of reactivity. Morphologically, reactive astrocytes can show hypertrophy, over branching, dysmorphic

processes [174, 43] and process polarisation towards the injury [21]. Physiologically, they can gain or lose functions and modulate their dynamics with neighbouring cells. Molecularly, they over-express Glial fibrillary acidic protein (GFAP), a marker for reactivity, and several genes are up or down-regulated depending on the disease. An open question is whether reactive astrocytes are protective or toxic for their micro-environment and the brain [42]. A first classification divides reactive astrocytes into two groups: A1, neuro-toxic and A2, neuro-protective [135]. Further, recent studies suggest a much broader and heterogeneous classification of reactive astrocytes [76] which is more in agreement with experiments showing how the reactive astrocytes respond differently to injuries depending on the distance [21, 11] or by the location [149].

In severe brain injuries, astrocytes respond, creating a glial scar at the side of the lesion [213], a compact and dense interconnected net of processes formed not only by reactive astrocytes but also by microglia, endothelial cells and fibroblasts and basal membrane. The glial scar is fundamental to prevent the spreading of the damage. However, the thick matrix produced by the glial scar might prevent the regeneration of neuronal axon [188].

In conclusion, astrocyte reactivity is involved in many diseases. Since this cellular state can last for a long time during the different stages of the disease, it is essential to understand how reactive astrocytes impact disease progression and investigate if their neurotoxicity might trigger or speed up the development of diseases [42].

2.1.3 Metabolism

Section 2.1.1 presented the fundamental role of astrocytes as metabolic mediators, which is the astrocytic function of interest in this thesis. Metabolism is the process performed by cells of our body to transform nutrients into ATP, the energy substrate, and lactate (Figure 2.5). As pointed in Chapter 1, ATP is essential for each living system. There are two ways that cells produce ATP: from glycolysis and the majority from the mitochondria. To start the production of ATP cells require glucose. Glucose is the nutrient that astrocytes take up from blood vessels through glucose transporters.

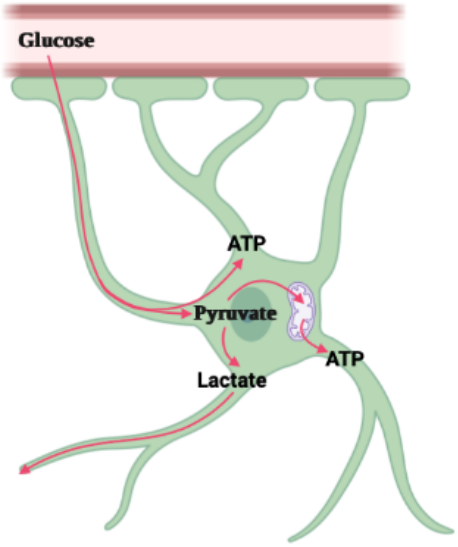

Fig. 2.5 A schematic representation of the main metabolic products in an astrocytes. Glucose is uptaken from the blood vessels. Glycolysis transforms glucose into pyruvate and ATP. Pyruvate goes through pyruvate oxidation and is transformed into Acetil coenzyme A (AcCoA). AcCoA starts the TCA cycle inside mitochondria. TCA cycle and Oxidative Phosphorylation produces the majority of ATP. Pyruvate is also used by the lactate dehydrogenase to produce lactate which is partially exported to neurons. (Image created with bioender.com.)

In eukaryotic cells, glycolysis is the first step of glucose metabolism which happens in the cytosol and is an anaerobic process. Thus, it does not require oxygen. A coarse-grain description consists of the breakdown of the sugar and ATP into pyruvate and ATP. As a matter of fact, glycolysis requires first ATP-consumption and eventually produces ATP. For each molecule of glucose consumed, the cell gain two molecules of ATP. In more detail, the first stage is the phosphorylation of glucose consuming ATP by the hexokinase into glucose-6-phosphate, which is then isomerised to fructose-6-phosphate by phosphohexose isomerase. Next, it is phosphorylated to fructose-1,6-biphosphate by phosphofructokinase. The enzyme aldolase catalyses the consumption of fructose-1,6-biphosphate into glyceraldehyde 3-phosphate. The phosphorylation of the latter by glyceraldehyde-3-phosphate dehydrogenase produces bisphosphoglycerate. The latter is further phosphorylated by phosphoglycerate kinase into phosphoglycerate and one molecule of ATP. Enolase catalyses the conversion of phosphoglycerate into phosphoenolpyruvate. Finally, pyruvate kinase catalyses the production of pyruvate and ATP.

The pyruvate produced from glycolysis is partially fermented and is catalysed by the lactate dehydrogenase, producing lactate. This process happens also in low or absence of oxygen. On the other hand, part of the pyruvate is carried from the cytosol to the matrix of mitochondria through a process called pyruvate oxidation [150].

Mitochondria are organelles that can be found in nearly every eukariotic cell. They have a double membrane and enclosing a volume that is called the matrix where the main energy (ATP) production is happening. The pyruvate oxidation produces acetyl coenzyme A (AcCoA) and transfers the metabolic process from the cytosol into the matrix. AcCoA starts the TCA cycle, which is a closed-loop of chemical reactions meaning that some products of the reactions are used to keep the loop going.

The metabolites of the TCA cycle function as electron carriers driving the electron transport chain of the OXPHOS in the inner membrane of mitochondria. There, the primary production of energy in form of ATP is happening by oxidation and reduction reactions that release chemical energy.

2.1.4 Calcium Signalling

Astrocytes are, in contrast to neurons, not electrically excitable cells. Therefore, they are not able to fire an action potential. However, they show a form of excitability regulating cytosolic calcium concentration (Ca^{2+}) [65]. Calcium is a central second messenger that translates external signals into intracellular responses in many if not all cell types. Calcium signalling of astrocytes also orchestrates the communication with neighbouring cells. Astrocytes can display different calcium dynamics: small and rapid transients in the cytosolic calcium concentration within their thin processes; larger locally-propagating waves; and slow calcium transients encompassing the whole cell. Calcium changes in astrocytes can be spontaneous [171] or induced by stimuli including neurotransmitters like glutamate [45]. Thus, synaptic activity during which neurotransmitters are released causes cytosolic calcium elevation in astrocytes.

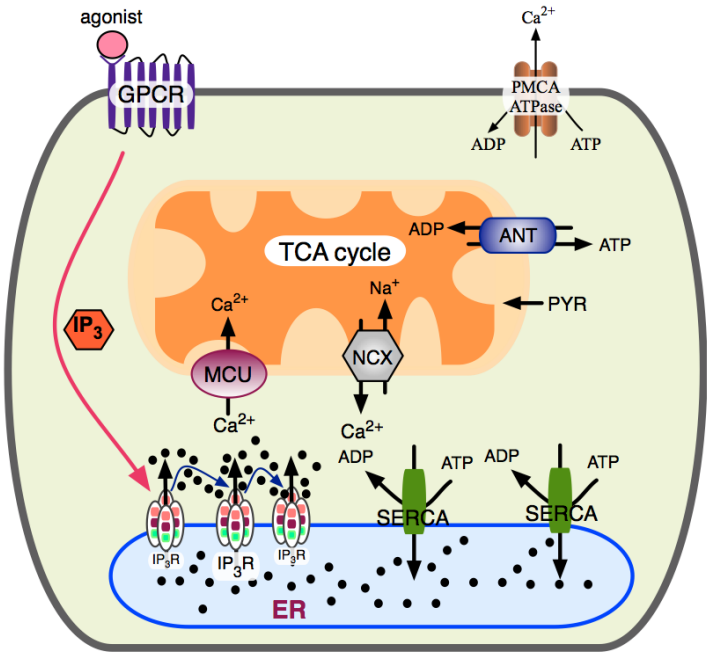

Fig. 2.6 Schematic representation of calcium Ca^{2+} exchange inside the cell. (Image provided by Mahsa Moein)

Regarding calcium, this thesis investigates the crosstalk of calcium signalling and metabolism. Within the cell, calcium is exchanged between three main compartments: endoplasmatic reticulum (ER), mitochondria, and extracel-

lular space (Figure 2.6). ER is the primary storage of Ca^{2+} for cells. High levels of Ca^{2+} are toxic for the cell. Thus cytosol generally keeps a low Ca^{2+} concentration [30].

There is active crosstalk between Ca^{2+} and ATP, which occurs between cytosol, mitochondria and the ER. The leading player in changes in the Ca^{2+} concentration is the ER which uptake large amounts of Ca^{2+} from the cytosol and can release it quickly. SERCA pumps pump calcium from the cytosol to the ER at the cost of ATP. Ca^{2+} is released into the cytosol from the ER by IP_3 receptor (IPR) and ryanodine receptor (RyR). IPR and RyR are activated by Ca^{2+} itself, inducing the calcium-induced calcium release (CIRC) mechanism where a high calcium level induces further calcium release into the cytosol [93]. IPR is additionally activated by IP_3 molecules generated by the phospholipase C (PLC)upon stimulation of G-protein coupled receptors (GPCR) in the plasma membrane by, e.g. neurotransmitters or other agonists.

As discussed in Section 2.1.3, mitochondria are the primary energy producer. However, crucial enzymes in the Krebs cycle require calcium for activation. Hence, Ca^{2+} is imported into mitochondria by the mitochondrial calcium uniporter (MCU) [196] and released by the sodium/calcium exchanger (NCLX). Spatially, mitochondria are typically located near the ER generating region with a high Ca^{2+} gradient [75].

Calcium signalling is a complex process, and the cell must balance the cytosolic Ca^{2+}. Moreover, there is a clear interaction between Ca^{2+} and cellular energy. Thus, further investigation of the crosstalk between these two processes is necessary.

2.1.5 Neurodegenerative Diseases

In the previous paragraphs, we established the central role that astrocytes play in the well-being of the CNS (Section 2.1.1) and that their involvement in neurodegenerative diseases leads to a reactive response (Section 2.1.2) impairing their normal functions. Dysfunctional behaviour of astrocytes in several diseases has been reviewed in different studies [1, 167] and also with a particular focus on metabolic dysfunctions [62].

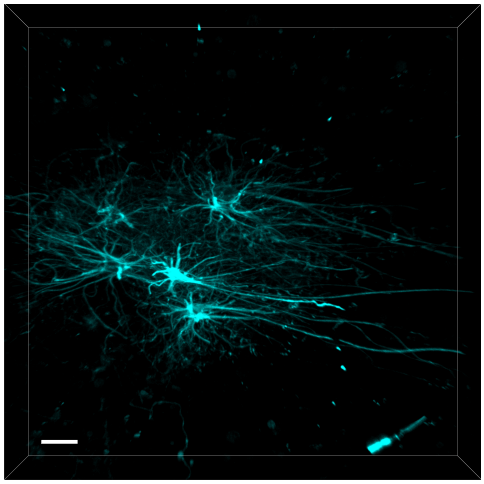

Fig. 2.7 Confocal microsopic image of amyloid-β plaque associated astrocytes acquired from human AD patient. The astrocytes surround the plaque and they contribute to the reactive glial net. Scalebar: $30\mu m$. (Image provided by Sonja Fixemer).

Alzheimer's Disease is the most common neurodegenerative disease and leads to the death of neurons in the brain. Even though causes are still not fully understood, it is known that β-amyloid plaques and neurofibrillary tangles impact the development of the disease [44]. Tangles cause damage inside of the neurons, while plaques are localised in the extracellular space. On the membrane of the neurons, there is a protein called amyloid precursor protein (APP). Typically, APP is cleaved by α-secretases, and the fragments produced are soluble in the extracellular space. However, if β-secretases cleave APP, then the fragment produced is a monomer called β-amyloid, which is not soluble. The accumulation of β-amyloid in the extracellular space generates β-amyloid plaques. While the detailed mechanisms are still elusive, these plaques are toxic for neurons and the brain environment because they can disrupt neuronal communications and attach to blood vessels, causing amyloid angiopathy [154, 223]. While plaques disrupt the normal neuronal behaviour from the outside, neurofibrillary tangles act from the inside. Microtubules are filaments inside the neurons that provide structural support and are used to transport cellular entities including vehicles of neurotransmitters and nutrients. Typically, the protein τ binds to these microtubules to stabilise them. However, in AD τ proteins abnormally detach and stick together, forming neurofibrillary tangles. The detachments of the protein τ disrupt the structure of neurons,

which eventually degenerate. As a result, neuronal communication with the neighbouring neurons is reduced and destroyed [183].

Various dysfunctions have been noticed in astrocytic functions in the presence of AD [1]. Astrocytes can internalise β-amyloid suggesting a protective mechanism [161, 181], which might cost them metabolic impairments as presented in [6] or altered calcium signalling [112]. Moreover, they appear to be responding with a morphological response moving their processes to surround the plaque [230] (Figure 2.7).

The main metabolic dysfunctions associated with AD [62, 13, 74, 238] are (i) impairment in up-taking glucose from the blood vessels [159], (ii) mitochondrial dysfunction [136, 156, 178], as well as (iii) dysfunctional behaviour in glycolysis and lactate dehydrogenase [33]. Impaired behaviours in astrocytes are not only limited to AD but also other neurodegenerative diseases, such as Hungtington's Disease [168], Parkinson's Disease [36] and Amyotrophic lateral sclerosis [233, 101].

2.2 Systems Biology

Studying complex biological or physical phenomena is always challenging when different phenomena coincide, which is typically the case for investigating a complex system such as a cell. Modelling is a valuable tool for investigating complex phenomena by integrating experiments and computational research [128]. A new discipline was established in early 2000 to address the complexity of biomedical research that merges experimental data, computational and mathematical tools: systems biology [128, 127].

Systems biology approaches can be described as hypothesis-driven experimental and mathematical modelling cycles (Figure 2.8). It starts by observing the natural physical phenomena and deciding the relevant features to include or to study through experiments. These features are used to simplify reality and create a model that captures such phenomena mechanistically in a simple manner. Since natural phenomena obey physical and mathematical laws, a mathematical formulation can be used to translate the simplified model into a mathematical framework. The advancements in computers and computer

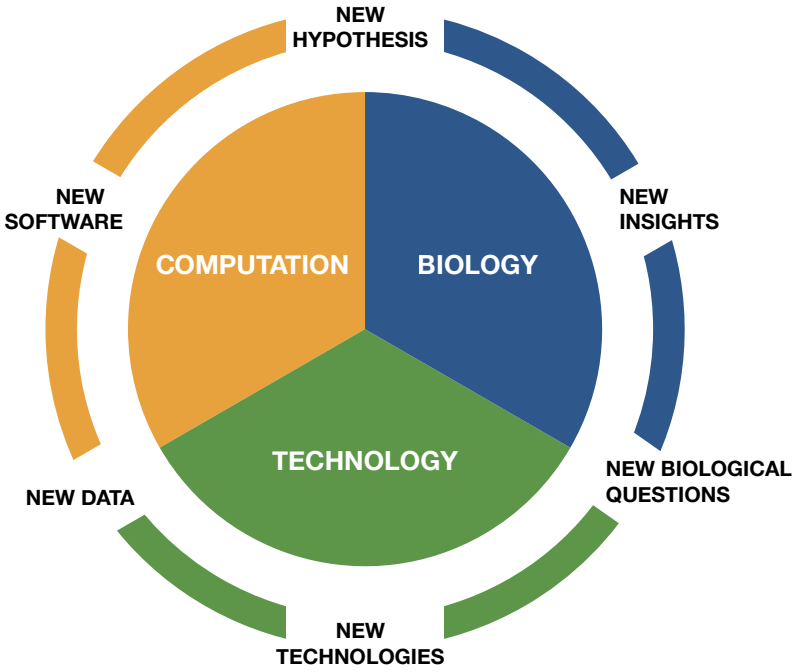

Fig. 2.8 This chart shows the circular process of systems biology, where biology, technology and computation are subsequently applied to improve knowledge of biological phenomena. New biological insights open new biological questions. The aid of new technologies helps investigate these questions. The data obtained are then used in new software leading to a new biological hypothesis. The loop can then start over to test this hypothesis.

science have enabled us to envision an alternative way to solve problems by obtaining numerical solutions instead of analytical solutions. The next step requires validating those numerical solutions, which can be done by comparing the solutions with experimental data. When the solution is validated, we can use mathematical and statistical tools to investigate the robustness of the results, which may highlight new insight into the biological phenomena. Last, the loop can start again to improve the description of the phenomena or to test a new hypothesis.

2.2.1 Modelling Cell Metabolism

Systems biology has been widely used to investigate the metabolic process in living cells [234]. Models contribute to studying metabolic diseases [72] and discovering new therapies [77]. In the literature, there are several approaches [234]. For example, a modelling approach based on associated gene functions for metabolism is the genome-scale model. These models reconstruct the metabolic pathways using stoichiometry and then analyse the interactions of the entire metabolic network at steady state by flux-balance analysis [133, 187]. Examples of these models in astrocytes have been proposed [147], also considering the coupling with neurons [61].

On the other hand, a more quantitative description of the metabolism is given by kinetic models that describe the enzymatic activity and mass balances leading to a system of ordinary differential equations (ODEs) for the evolution of metabolite concentrations over time. Focusing on astrocytes, compartmentalised metabolic models have been proposed to study the astrocytic-neuron interaction [15, 16, 71, 123]. Both of these approaches describe metabolism in a pretty detailed manner with many parameters and chemical reactions, and they provide a good approximation of the average metabolic concentration behaviour, which is a fast process. However, in biology, chemical concentrations inside the cell are not heterogeneous. Reactions happen in specific locations. For example, mitochondria are neither homogeneously distributed nor ionic pumps along the cell membrane. These observations point to the missing component in these modelling approaches, the spatial dimension, which cannot be neglected in the next generation of models as reviewed in [2].

The importance of space geometry has started to be considered by different scientists in different contexts: in excitable cells [92], in calcium signalling either in dendritic spine [25] or in astrocyte [125].

In conclusion, most of the proposed metabolic approaches assume steady-state concentrations or spatial homogeneity. However, in reality, cellular processes are better described by a reaction-diffusion system. Thus, in this thesis, we want to investigate the potential effects of the reaction-diffusion system as a potentially more realistic approach than previously proposed models. In particular, the interplay between the cellular geometry (morphology), spatial dimension and metabolism had not yet been investigated before this thesis.

2.2.2 Modelling Calcium Signalling

The importance of calcium dynamics in astrocytes discussed in Section 2.1.4 has been under scientific investigation for decades, and many models have been proposed [169]. The modelling approaches to investigate calcium dynamics are very broad [87] ranging from deterministic to stochastic approaches, and spatially homogeneous [79, 134, 78] to spatially distributed [169, 202] systems. These modelling approaches can address the different scales: from molecules to single cells and neuron-astrocyte networks.

The exchange of cytosolic calcium comes with the expense of ATP as discussed in Section 2.1.4. Some mathematical models focus on the interplay between Ca^{2+} and mitochondria, such as [143, 144, 73, 31]. Geometric-based models for astrocytes and calcium dynamics have also been investigated in literature as in [202, 166, 222]. However, the field lacks a model to investigate the interplay of the metabolic process and calcium signalling within a spatial modelling framework.

2.3 Modelling Tools

After presenting the state-of-the-art models for metabolic processes (Section 2.2.1) and calcium dynamics (Section 2.2.2), we introduce the mathematical formulations used to include the spatial component. As previously discussed,

cells can be seen as complex systems governed by reaction-diffusion equations. Thus, the necessity is not to describe the model through a set of ODEs but using partial differential equations (PDEs) that include partial derivatives in space and can be solved in two and three-dimensional domains. For further reading, we refer the readers to [160].

2.3.1 Reaction-Diffusion System

Mathematically, a reaction and diffusion model is described by a parabolic partial differential equation [200]. In chemistry, it describes the changes in space and time of a chemical concentration. The partial differential equation gives the general formulation for the concentration of a chemical specie u:

$$\frac{\partial u}{\partial t} = D\Delta u + R(u), \tag{2.1}$$

where Δu is the Laplacian of the concentration u. Thus, the sum of all the second partial derivatives $\Delta u = \sum_{i=1}^{d} \frac{\partial^2}{\partial x_i^2}$ where d is the spatial dimension.

The left-hand side of Equation (2.1) describes the change in time of the concentration of the chemical species through the temporal partial derivative, $\frac{\partial u}{\partial t}$. While on the right-hand side, the first term, $D\Delta u$, describes the diffusion of the chemical through the second spatial derivative of the specie concentration multiplied by a diffusion coefficient D, and the second term, $R(u)$, is a function describing the chemical reactions where u is involved.

Equation (2.1) has a unique solution when it is supplemented with boundary conditions and the initial value for the concentration.

In 1952, Turing [219] contributed significantly to biochemistry, suggesting that chemicals can diffuse and react in a way that produces steady-state heterogeneous spatial chemical patterns.

2.3.2 Fick's Law

The first term on the right-hand-side of Equation 2.1 comes from the first Fick's law [102]. It describes the diffusion of concentration relating its gradient to the diffusive flux. The flux moves from regions of higher concentration to regions

with lower concentration:

$$J = -D\nabla u \tag{2.2}$$

We can now derive Fick's second law by applying the conservation of mass equation. Thus, we require the system to be closed.

$$\frac{\partial u}{\partial t} + \nabla \cdot J = 0 \Rightarrow \frac{\partial u}{\partial t} + \nabla \cdot (-D\nabla u) = 0 \; . \tag{2.3}$$

Assuming that the diffusion coefficient is a constant D, we can change the differentiation order:

$$\nabla \cdot (-D\nabla u) = -D\nabla \cdot \nabla u = -D\Delta u \; .$$

Substituting in Equation (2.3), we obtain Fick's second law:

$$\frac{\partial u}{\partial t} - D\Delta u = 0 \; . \tag{2.4}$$

2.3.3 Law of Mass Action

A possibility for the reaction term, $R(u)$, of Equation (2.1) is to describe the chemical kinetics following the law of mass action [226, 124], one of the fundamental laws of chemical kinetics. The law of mass action describes the product accumulation rate as the probability of collision of the reactants. Mathematically, considering two reactants, A and B, that react to produce C:

$$\mathrm{A} + \mathrm{B} \xrightarrow{k} \mathrm{C} \; .$$

The rate of accumulation of the product [C] is considered as the concentrations of the reactants multiplied by a rate constant k that depends on the reaction and on the temperature:

$$\frac{\mathrm{d}[\mathrm{C}]}{\mathrm{d}t} = k[\mathrm{A}][\mathrm{B}] \; .$$

It follows that the reaction term of Equation (2.1) of the concentration [C] is $R([\mathrm{C}]) = k[\mathrm{A}][\mathrm{B}]$.

2.4 Numerical Methods

Numerical methods have been developed to solve engineering, physics and science problems that cannot be solved analytically, which is often the case in systems biology due to the complexity of the systems under consideration.

2.4.1 Finite Element Methods

In the latter half of the 20^{th} century, finite element methods (FEM) have become a leading numerical tool for solving partial differential equations [116]. In brief, it discretises the continuum space into a finite number of finite elements and reduces the solution of the PDEs into the solution of an algebraic system.

First, the problem is stated through a PDE. For example, we consider Equation 2.1 in a bounded domain Ω, which is well posed with an initial condition at an initial time and a boundary condition. For the boundary conditions, we consider pure Neumann, requiring that there is no flux on the boundary of the domain ($\partial\Omega$). The problem is then to find the concentration $u : \Omega \times [0, T] \to \mathbb{R}$ that satisfies:

$$\begin{cases} \frac{\partial u}{\partial t} = D\Delta u + R(u) \quad \text{in} \quad \Omega \times (0, T] \\ u(t = 0) = u_0 \quad \text{in} \quad \Omega \\ \nabla u \cdot n = 0 \quad \text{on} \quad \partial\Omega \times (0, T] \end{cases} \tag{2.5}$$

This differential form of the problem is called the *strong formulation*. However, FEM solves the *weak formulation* which is an integral form equivalent to the strong form. The weak form is obtained by multiplying the strong form with an admissible *test function*, integrating it over the domain and applying Divergence Theorem. The general idea behind transforming the strong form into the weak form is that the solution and the test function live in a Hilbert space. In a Hilbert Space, the solution continuity is relaxed since it does not need to be fully differentiable, but it is a set of functions which share the same weak derivative. Since we are working with a class of equivalence of functions, it is much easier to build a basis to generate the Hilbert space compared to a classical differentiable space.

In our example, the weak formulation of Equation 2.5 requires finding u in a suitable Hilbert space V, such that for all admissible test functions v, u satisfies:

$$\int_\Omega \frac{\partial u}{\partial t} v \, \mathrm{d}x = \int_\Omega D\Delta u v \, \mathrm{d}x + \int_\Omega R(u) v \, \mathrm{d}x. \tag{2.6}$$

Integrating by parts:

$$-\int_\Omega D\Delta u v \, \mathrm{d}x = \int_\Omega D\nabla u \nabla v \, \mathrm{d}x - \int_{\partial\Omega} D\frac{\partial u}{\partial n} v \, \mathrm{d}s.$$

Since we have specified pure Neumann boundary condition (Equation 2.5), the boundary terms vanish. We substitute it, and the weak form becomes:

$$\int_\Omega \frac{\partial u}{\partial t} v \, \mathrm{d}x = -\int_\Omega D\nabla u \nabla v \, \mathrm{d}x + \int_\Omega R(u) v \, \mathrm{d}x. \tag{2.7}$$

The theorem of Lax Milgram [17] ensures the existence of the weak solution by requiring that the bilinerear form associated to equation (2.7) is bounded and coercive. In particular, the proof for parabolic equations can be found in [232].

After deriving the weak formulation, the problem needs to be discretised. In parabolic equations, we need to discretise the problem in time and space.

In our example, the time interval is then discretised using a finite difference scheme [209]. The time is divided into subintervals, where Δt denotes the time step's size. The subscript i indicates the solution of the concentration at the time t_n. Using a backward Euler method to approximate the continuous time, we obtain the discretisation of the time derivative:

$$\frac{\partial u}{\partial t} \approx \frac{u_{n+1} - u_n}{\Delta t}.$$

The spatial domain is discretised in finite elements generating the so-called *mesh*. The *nodes* are the points on the finite elements where the unknown function is calculated by solving the weak form. By interpolation, the values at the nodal points (nodes) are used to approximate the values between the nodes. The function used to make the interpolation is called *shape function*. A

general formulation of the discretised solution u_h of the weak problem for a chosen vector space with shape functions ϕ_i has the form:

$$u_h(x) = \sum_{i=1}^{N} \phi_i(x) u_i, \tag{2.8}$$

where u_i are the unknowns at the ith nodal point with $i = 1, \cdots, N$. Moreover, boundary conditions need to be taken into account in some nodes.

The discretised problem of Equation 2.7 leads to a sequence of problems which seek for the solution,u_{n+1}, at the time t_{n+1} knowing the solution at the previous time step, u_n, for all test functions, v:

$$\int_\Omega \frac{u_{n+1} - u_n}{\Delta t} v \, \mathrm{d}x = -\int_\Omega D \nabla u_{n+1} \nabla v \, \mathrm{d}x + \int_\Omega R(u_{n+1}) v \, \mathrm{d}x. \tag{2.9}$$

We can then rewrite Equation 2.9, more compactly:

$$F_{n+1}(u_{n+1}, u_n; v) = 0 \quad \forall v$$

where

$$F_{n+1}(u_{n+1}, u_n; v) = \int_\Omega (\Delta t^{-1}(u_{n+1} - u_n) + D \nabla u_{n+1} \nabla v - R(u_{n+1}) \mathrm{d}x$$

In conclusion, we search the solution u_{n+1} in the form of Equation 2.8. This discretisation leads to a system of equations defined by the interpolation matrix where the unknowns are the nodal points that can be solved using direct or iterative solvers [185].

The accuracy of the solution is assessed in terms of error [54, 88, 53] and convergence. As the mesh is refined, the approximated solution u_h converges to the exact solution and convergence is ensured by Céa's Lemma [64].

2.4.2 Unfitted Methods

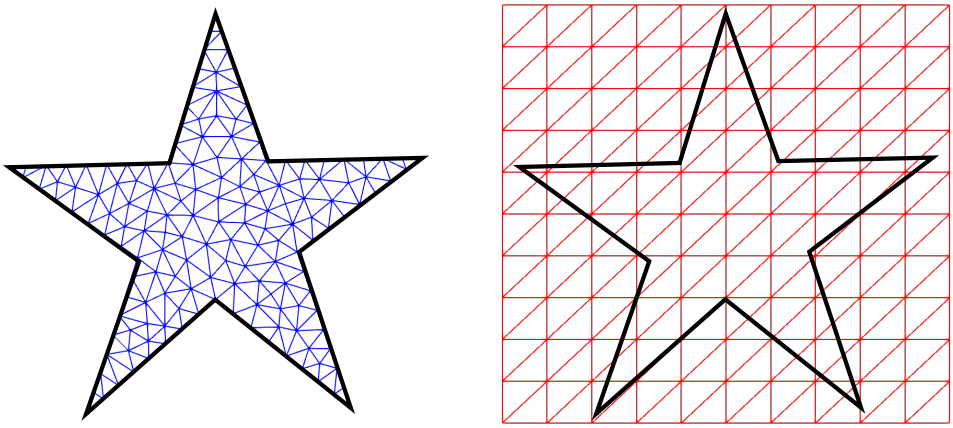

Fig. 2.9 In classic FEM, the mesh is built to conform to the boundary of the star (right). While unfitted methods embeds the star in a background mesh allowing the finite elements to get cut by the boundaries (left).

Unfitted methods were proposed to address problems where generating the finite element mesh is challenging such as for highly complex geometries, fracture propagation or large deformations, and might lead to numerical errors. Classical finite elements require the mesh to conform to the boundary as well as internal features such as material interfaces and cracks (Figure 2.9). On the other hand, unfitted methods were created to overcome difficulties in meshing the space [162] by allowing the boundary of the domain to be independent of the mesh (Figure 2.9).

Babuška [18] was the first to suggest partition of unity to enrich the finite element approximations with a priori knowledge about the exact solution to allow arbitrary function to be reproduced exactly by the finite element spaces. The partition of unity allows to describe a topological space as a collection of non-negative functions. These functions have the properties that every point has only finitely many nonzero values, and their sum is one.

Following the partition of unity idea, the Generalised Finite Element Method (GFEM) proposed by Strouboulis *et al.* [214, 215] uses special numerically computed functions and enrichments to include the a priori information. Similarly, the extended finite element method (XFEM) [82, 151] uses local enrichment on a portion of the mesh to restrict the effect of localised features in the surround-

ing and was the first method to address discontinuities without remeshing or, at least, with minimal remeshing [40].

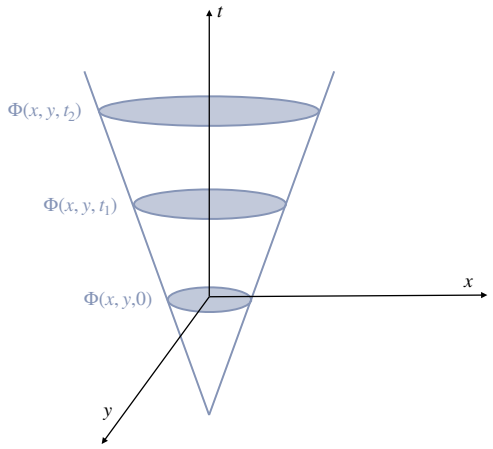

Fig. 2.10 A level set function describes an evolving surface Φ. The front of the evolving surface is defined implicitly as the zero level set $\Phi(x, y, t = 0) = 0$. Different time produce different values of the front as the intersection of Φ with the plane t.

While partition of unity provides a great advantage in working with unfitted mesh, it might also lead to numerical problems [3]. The matrix of the system can be ill-conditioned, meaning that the solution of the system is inaccurate. Ill-conditioning problems can arise depending on how the interface intersects the finite elements. Thus, it requires treatments with pre-conditioning [23, 152, 108, 152, 5, 3].

For this reason, an extension of XFEM was proposed in the cut finite element method (CutFEM) [111, 58]. Both XFEM and CutFEM can define the object geometry with a level set function [206] (Figure 2.10) which has already been used to model biological phenomena [82, 83].

Opposite to XFEM, CutFEM allows the interface to cut the finite element mesh arbitrarily, adding a stabilisation term in the weak form, such as the ghost penalty technique [57]. The addition of this term ensures the coercivity property, required for the solution existence by the theorem of Lax Milgram, and the control of the conditioning number. This is the key difference with XFEM, where it is necessary the addition of pre-conditioning to ensure the coercivity. Lastly, boundary conditions are applied using Nitsche's method [164].

The recently introduced Φ-FEM [90] appeared as an unfitted method where the solution is found by multiplying the level set function with the finite element function. In this way, the Dirichlet boundary condition is imposed on the solution.

Unfitted methods proved their ability to disentangle geometry and mesh, allowing them to generate the meshing independently from the geometry, and therefore complex domains such as images can be used directly in simulations. From the proposed methods, CutFEM is the one that ensured proper conditioning of the system even with a complex morphology such as an astrocyte. Moreover, the CutFEM library is based on the finite element software FEniCS [138] which is an open-source software to solve PDEs using FEM. Dolfin, a Python package with an efficient C++ core, allows us to solve abstract scientific models using finite element methods with a few lines of code.

Other libraries include open XFEM ++, AMIE [85], getFEM [194], FreeFEM [114], Deal.ii [12].

2.4.3 Other Methods

For completeness, we point out that other approaches exist to solve partial differential equations in literature. Proposed before the advent of FEM, the finite difference method [209] approximates the derivatives with finite differences and does not require the weak formulation. It discretised the spatial domain in a grid of finite points and the time interval. The solution is found in each point of the grid, solving an algebraic system that contains the finite differences and the values at the neighbouring points. This method was used in our work for time discretisation.

Moreover, we indicate generalised finite difference methods as a meshless methods proposed in [216]. GFDM uses classical FDM on an irregular grid. However, the position of the grid points requires some treatments to avoid singularity and ill-conditioning [27].

Boundary Element Methods (BEM) [46, 20] solve the PDEs by formulating them as integral equations. Compared to FEM, BEM requires to discretise only at the boundary. Thus, the advantage of BEM is its computationally higher efficiency compared to FEM. Hence, BEM is a good method in problems where

there is a good knowledge of the solution and it is possible to calculate the Green's functions which is not always an easy task.

In contrast with the finite difference method, Finite Volume Methods (FVM) [95] use integration to approximate the solution. It requires that conservation law holds through the volume elements based on fluxes using the divergence theorem. FVM is primarily used in computational fluid dynamics.

The last method we suggest as an alternative approach is isogeometric analysis (IGA) [117] which incorporates NURBS basis functions into finite element frameworks. Since the NURBS are the building block of CAD geometries, IGA can provide seamless coordination between CAD software and FEA packages. In addition, NURBS basis functions can exactly represent conic sections. However, in IGA, geometries and finite element analysis are strictly linked. The basis functions defining the CAD geometries are used as the basis functions for the FEA. Even if CAD geometry can deal with complex shapes, it generally requires patching together pieces of the geometry. This patching might generate geometrical artefacts, a current open problem in IGA. Moreover, local refinement is not straightforward in IGA [120], which can make the identity between the geometrical space and the solution space an undesired constraint. This led to the GIFT concept [14] where the geometry and "field approximation" can be chosen arbitrarily, whilst keeping the exact boundary description provided by CAD.

In conclusion, in this last section, we presented different numerical methods to solve partial differential equations. In particular, these methods can be used to solve models based on reaction-diffusion systems (Section 2.3). Moreover, since we discussed the importance of geometry-based modelling as the next direction for metabolic models (Section 2.2), we focused on methods that allow to incorporate easily complex geometries.

CHAPTER 3

CutFEM for a Spatially Resolved Energy Metabolism Model

As presented in Chapter 1, our goal is to incorporate physiological cellular morphologies into a metabolic model. In our first manuscript [97] presented in this chapter, we focused on the numerical approach to implement a spatial energy metabolism model. For this purpose, we compared the standard finite element method (Section 2.4.1) to the cut finite element method (CutFEM) as one of the unfitted methods discussed in Section 2.4.2. In this framework, we also introduced a dynamic model for energy metabolism which is mathematically described by the tools presented in Section 2.3. The comparison showed that CutFEM leads to comparable results as the classic finite element method with the ability to incorporate implicitly complex geometry. The framework is explained below in detail to allow the usage also by non-experts in Computational Sciences. As the first author of this manuscript, I contributed to the development of the model, the implementation, the preparation of the images and the writing of the manuscript.

Abstract

A thorough understanding of brain metabolism is essential to tackle neurodegenerative diseases. Astrocytes are glial cells which play an important metabolic role by supplying neurons with energy. In addition, astrocytes provide scaffolding and homeostatic functions to neighboring neurons and contribute to the blood-brain barrier. Recent investigations indicate that the complex morphology of astrocytes impacts upon their function and in particular the efficiency with which these cells metabolize nutrients and provide neurons with energy, but a systematic understanding is still elusive. Modelling and simulation represent an effective framework to address this challenge and to deepen our understanding of brain energy metabolism. This requires solving a set of metabolic partial differential equations on complex domains and remains a challenge. In this paper, we propose, test and verify a simple numerical method to solve a simplified model of metabolic pathways in astrocytes. The method can deal with arbitrarily complex cell morphologies and enables the rapid and simple modification of the model equations by users also without a deep knowledge in the numerical methods involved. The results obtained with the new method (CutFEM) are as accurate as the finite element method (FEM) whilst CutFEM disentangles the cell morphology from its discretisation, enabling us to deal with arbitrarily complex morphologies in two and three dimensions.

3.1 Introduction

We propose to test and verify a simple numerical framework to solve a simplified model of metabolic pathways, representative of cellular metabolism in the brain. Metabolic models can aid the understanding of cell behaviour. Most metabolic models involve the solution of a system of ODEs [71] leaving open the question of how the geometry and spatial organization affect cell behaviour. This work presents a method that is a first step towards extending existing models to answer this question. The method, based on recent developments in unfitted finite element methods is general, and can deal with an arbitrary number of coupled reaction diffusion equations and handle complex cell morphologies. Thanks to the versatility of the automatic code infrastructure provided by

FEniCS, the code is well-suited to newcomers to finite element methods interested in modelling biological systems.

To test the new framework, we address complex cell geometries in two and three dimensions and compare the method to the standard finite element method in terms of accuracy. The results obtained with the new method CutFEM are as accurate as the finite element method (FEM) whilst CutFEM disentangles the cell morphology from its discretisation, enabling to deal with arbitrarily complex morphologies, including kinks and triple junctions, in two and three dimensions.

A thorough understanding of brain metabolism is essential to tackle neurodegenerative diseases [141, 62]. Astrocytes are glial cells which play an important metabolic role by supplying neurons with energy [24]. These cells also provide scaffolding and help repair neighboring neurons, where they maintain balanced ionic concentrations (homeostasis) and contribute to the blood-brain barrier by preventing the diffusion of large molecules into the brain.

Recent investigations show that the morphology of astrocytes, which can be complex (see Figure 3.1), impacts upon their function, in particular the efficiency with which these cells metabolise nutrients and provide neurons with energy [199].

Modelling and simulation could be effective in furthering our understanding brain metabolism by enabling to test biological hypotheses and investigate the relative importance of model parameters on quantities of interest to biologists.

The challenges involved with modelling and simulating metabolic activity in cells include:

1. Building a representative model of the metabolic pathways, usually a set of reaction-diffusion equations;

2. Identifying the parameters for these partial differential equations (PDEs) as well as the sensitivity of the system to these parameters [191, 113, 190, 192, 193, 189];

3. Discretising the complex and evolving geometries of the cells;

4. Solving this set of PDEs on these complex domains;

Fig. 3.1 The complex morphology of an astrocyte from a human post mortem sample obtained by fluorescent (GFAP) super-resolution light microscopy [186] and reconstructed by the machine learning based tool MicMac [199].

5. Ensuring the accuracy of the solution by measuring discretisation error [54, 88, 53];

6. Ensure the usability of the numerical framework by non-experts.

This last point aims at simplifying multi-disciplinary interactions between computational, data science and domain experts, it is also becoming increasingly important to devise numerical frameworks which can be used and enhanced without being a computational science expert. To do so, open-source frameworks such as FEniCS [138, 9, 110], getFEM [194], FreeFEM [114], Deal.ii [12] are all possible candidates. These open-source frameworks enable the user to write models in a language which is natural to them and requires minimal interaction with technical details associated with well-established numerical methods.

Concerning metabolic activities, some models focused their attention to the metabolic pathways which they describe as a series of chemical reactions that enable the synthesis and breakdown of molecules as [175, 153, 61, 205].

So far, very little attention has been paid to the role of cell morphology on the modelling [125, 92]. However, cell morphology is known to be important to describe the state of the cell. For example, [13] show the importance of cell morphology on the development of Alzheimer's disease.

In this paper, we tackle points 1., 3., 4., and 6., above, and leave points 2. and 5. for further communications, as well as the extension to evolving domains.

Model We present a simple model of energy metabolism which takes into account the main pathways of the metabolic process in a single cell. Here, we focus on an astrocyte as a specific cell, but the developments are general. In particular, we include glycolysis, Lactate Dehydrogenase, TCA cycle and basal cellular activity explicitly in the cell model. Each pathway is described by a chemical reaction leading to a coupled reaction diffusion system.

Cell geometry Our ultimate goal is to enable the use of microscopy to produce input geometries for our computational framework and include the evolution of the cellular domain. To enable this, we define cell geometries using signed distance functions, also known as level-set functions [170, 206], which were successfully deployed in modeling other biological phenomena with moving interfaces, such as [82, 83].

Discretisation The solution of the set of coupled reaction diffusion equations has two characteristics, which create challenges for the standard finite element method:

- Local gradients in metabolite concentrations;
- Discontinuities across cell boundaries.

Standard finite element method would require to create a mesh that fits the boundary of the object. Even though much progress has been made in meshing technology [146], the advantages of methods that separate the geometry from the object are very appealing for our ultimate objective of describing a cell

evolving in time. Classic FEM would require to build a mesh conforming the object at each time step leading to very high computational drawbacks.

Enriched finite element methods such as the partition of unity FEM (PUFEM) [151, 18], the generalized finite element method (GFEM) [215] and the extended finite element method [26] are ideal to tackle these two challenges [39, 82].

Indeed, these methods enable the local enrichment of the discrete solution space with known features about the solution, including discontinuities and sharp gradients or singularities. This makes it possible to handle arbitrarily complex geometries quasi-independently of the mesh (see Figure 3.2).

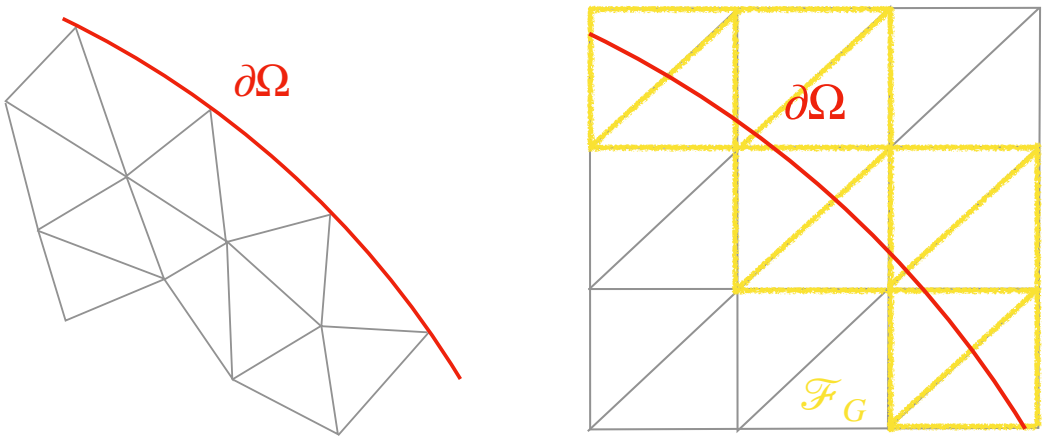

(a) FEM (b) CutFEM

Fig. 3.2 (a) Standard FEM requires the mesh to be conform the boundary of the domain $\partial\Omega$ (b) CutFEM embeds the implicitly defined interface $\partial\Omega$ into a background mesh, in yellow the set of ghost penalty facets $\mathcal{F}_G$.

Nonetheless, without preconditioning or special treatment [23, 131, 152, 108, 5, 4, 3] enriched finite elements cannot natively deal with arbitrarily complex geometries because of particular geometrical limit cases (interfaces passing close to a degree of freedom) and ill-conditioning stemming from linear dependencies due to complex enrichment functions acting upon large parts of the computational domain.

CutFEM [111, 57, 58, 35, 68, 67, 69] is an extension of XFEM that naturally addresses limit cases associated with complex geometries, and lends itself to image-based simulations. Moreover, we use the libCutFEM library,

which is a cut finite element extension of the open-source framework of the FEniCS Project [9, 138, 110, 58]. FEniCS offers a highly flexible and easy way of transforming models expressed as partial differential equations into numerical methods based on the finite element method through the Unified Form Language (UFL) [10], a domain-specific programming language for writing the weak form of partial differential equations. The UFL specification of the finite element problem is then automatically translated by the other components of the FEniCS Project (DOLFIN [9] and the FEniCS Form Compiler (FFC) [138]) into high-performance specific C++ code with little or no user intervention.

Solution scheme To solve the set of coupled, time-dependent and non-linear PDEs, we first discretise in time using a standard implicit time stepping scheme. The non-linear equation is solved using a Newton-Raphson scheme. The Jacobian, required for the Newton-Raphson scheme, is calculated automatically at the symbolic level by FEniCS. This greatly eases the implementation from the user's perspective, as deriving and implementing the consistent Jacobian manually can be a tedious and error prone task. The resulting linear systems at each step of the Newton-Raphson algorithm is solved using standard linear solvers from the PETSc library [19].

Usability and extensibility of the framework Thanks to the flexibility of FEniCS, the framework is generic and usable by biologists without a background or specific training in Computational Sciences or Applied Mathematics. The code used to create the two of the examples is freely online accessible (see availability of data and materials) and can be adapted to other problems straightforwardly.

The paper is organized as follows. In Section 3.2, we present the biological model for energy metabolism followed by the governing equation and its weak form. The FEM and CutFEM discretization can be found in Section 3.3. In Section 3.4 a detailed explanation of how implement our model in CutFEM is presented. Our numerical results are introduced in Section 3.5 and the conclusions follow in Section 3.6.

3.2 The problem Formulation

The aim of this section is to introduce the energy metabolism model, which can be expressed as a set of partial differential equations, in its strong and weak form.

3.2.1 Basic Model for Energy Metabolism

The scope of this model is to isolate conceptually the essential mathematical properties of the metabolic processes of a cell, the mechanism that generate energy for cellular activities from the synthesis and breakdown of nutrients [71].

The simplified model of metabolic pathway in a cell is sketched in Figure 3.3 and described by the following reactions (see abbreviations for details)

$$\mathrm{HXK} := \mathrm{GLC} + 2\,\mathrm{ATP} \rightarrow 2\,\mathrm{ADP} + 2\mathrm{GLY} \tag{3.1}$$

$$\mathrm{PYRK} := \mathrm{GLY} + 2\,\mathrm{ADP} \rightarrow 2\,\mathrm{ATP} + \mathrm{PYR} \tag{3.2}$$

$$\mathrm{LDH} := \mathrm{PYR} \rightarrow \mathrm{LAC} \tag{3.3}$$

$$\mathrm{Mito} := \mathrm{PYR} \rightarrow 28\,\mathrm{ATP} \tag{3.4}$$

$$\mathrm{act} := \mathrm{ATP} \rightarrow \mathrm{ADP}. \tag{3.5}$$

The pathway starts when the molecules derived from food (nutrients) enter the cytosol of the cell, and the process called glycolysis starts the breakdown of glucose (GLC) into two molecules of pyruvate (PYR). The glycolysis process can be split, to our modeling purpose, into two main chemical reactions: ATP-consuming (4.1) and ATP-producing (4.2). The pyruvate produced by glycolysis can, then, be converted into lactate (LAC) by the enzyme lactate dehydrogenase (LDH) simplified with the chemical reaction (4.3) or enter mitochondria and used to produce ATP through the TCA cycle shown in reaction (4.4).

Last, we take into account the activity of the cell which uses ATP for its own sustenance represented by the chemical reaction (4.5).

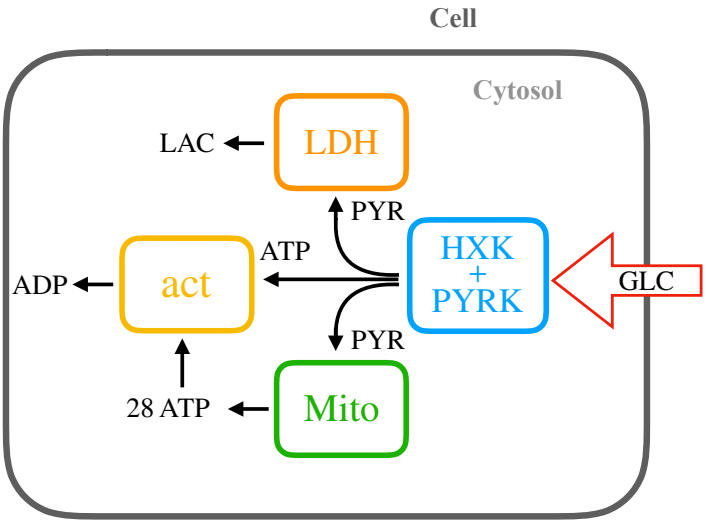

Fig. 3.3 The main pathways we consider in our Simplified Model of Energy Metabolism of a cell. The glucose (GLC) enters inside the cell into the cytosol and takes part into the glycolysis composed by the two reactions HXK and PYRK. The products of the glycolysis, PYR and ATP, are then used into LDH reaction, that generates LAC, into act reaction, that describes the cellular activity producing ADP, and inside the mitochondria where the reaction denoted Mito happens generating the major source of ATP for the cell.

In order to facilitate our model we consider that the backward reactions are negligible. Moreover, we consider that the enzymes that catalyzed the chemical reactions are located in a specific region of the cellular domain.

3.2.2 Strong Formulation of Governing Equations

Let Ω be an open and bounded subset of $\mathbb{R}^d$ (d=2 or 3) with Lipschitz-continuous boundary and we denote the concentration of the chemical species using the bracket notation, $[\,\cdot\,]$, as a function

$$[\,\cdot\,] : \Omega \times [0, T] \to \mathbb{R}.$$

Mathematically, we can express the sequence of reactions Equations (4.1)-(4.5) with a coupled system of semi-linear parabolic reaction diffusion equations [160]. We consider that the species involved are subject to diffusion in the domain and we denote $D_{[\cdot]} > 0$ the diffusive constants. The reactions obey

to the law of mass action [226] where $K_{\text{HXK}}, K_{\text{PYRK}}, K_{\text{LDH}}, K_{\text{Mito}}$ and K_{act} are the rate constants and we introduce Gaussian functions, indicated with $\mathcal{G}_{\text{HXK}}(x_0, \sigma)$, $\mathcal{G}_{\text{PYRK}}(x_0, \sigma)$, $\mathcal{G}_{\text{LDH}}(x_0, \sigma)$, $\mathcal{G}_{\text{Mito}}(x_0, \sigma)$ and $\mathcal{G}_{\text{act}}(x_0, \sigma)$, to locate the region where the reactions are happening

$$\mathcal{G}_{\cdot} = \mathcal{G}(x_{0,\cdot}, \sigma_{\cdot}) = \frac{1}{\sqrt{2\pi\sigma_{\cdot}^2}} \exp - \frac{(x - x_{0,\cdot})^2}{2\sigma_{\cdot}^2},$$

where $x_{0,\cdot} \in \Omega_{\cdot}$ and $\sigma \in \mathbb{R}$. Eventually, to represent the entrance of the glucose inside the cytosol we define a source term function $f : A \times [0, T] \to \mathbb{R}$, where A is a subset of Ω as

$$f(x,t) = \begin{cases} \alpha \in \mathbb{R} \quad \text{if} \quad (x,t) \in A \times [0,1], \\ 0 \quad \text{otherwise.} \end{cases}$$

The strong form of the reaction diffusion system is then, finding the concentrations $[\text{GLC}](x,t)$, $[\text{ADP}](x,t)$, $[\text{ATP}](x,t)$, $[\text{GLY}](x,t)$, $[\text{PYR}](x,t)$ and $[\text{LAC}](x,t)$ for all $x \in \Omega$ and $t \in [0,T]$ such that

$$\begin{cases} \frac{\partial[\text{GLC}]}{\partial t} = & D_{[\text{GLC}]}\nabla^2[\text{GLC}] - K_{\text{HXK}}[\text{GLC}][\text{ATP}]^2\mathcal{G}_{\text{HXK}} + f \\ \frac{\partial[\text{ATP}]}{\partial t} = & D_{[\text{ATP}]}\nabla^2[\text{ATP}] - 2K_{\text{HXK}}[\text{GLC}][\text{ATP}]^2\mathcal{G}_{\text{HXK}} \\ & +2K_{\text{PYRK}}[\text{ADP}]^2[\text{GLY}]\mathcal{G}_{\text{PYRK}} + 28K_{\text{Mito}}[\text{PYR}]\mathcal{G}_{\text{Mito}} \\ & -K_{\text{act}}[\text{ATP}]\mathcal{G}_{\text{act}} \\ \frac{\partial[\text{ADP}]}{\partial t} = & D_{[\text{ADP}]}\nabla^2[\text{ADP}] + 2K_{\text{HXK}}[\text{GLC}][\text{ATP}]^2\mathcal{G}_{\text{HXK}} \\ & -2K_{\text{PYRK}}[\text{ADP}]^2[\text{GLY}]\mathcal{G}_{\text{PYRK}} + K_{\text{act}}[\text{ATP}]\mathcal{G}_{\text{act}} \\ \frac{\partial[\text{GLY}]}{\partial t} = & D_{[\text{GLY}]}\nabla^2[\text{GLY}] + 2K_{\text{HXK}}[\text{GLC}][\text{ATP}]^2\mathcal{G}_{\text{HXK}} \\ & -K_{\text{PYRK}}[\text{ADP}]^2[\text{GLY}]\mathcal{G}_{\text{PYRK}} \\ \frac{\partial[\text{PYR}]}{\partial t} = & D_{[\text{PYR}]}\nabla^2[\text{PYR}] + K_{\text{PYRK}}[\text{ADP}]^2[\text{GLY}]\mathcal{G}_{\text{PYRK}} \\ & -K_{\text{LDH}}[\text{PYR}]\mathcal{G}_{\text{LDH}} - K_{\text{Mito}}[\text{PYR}]\mathcal{G}_{\text{Mito}} \\ \frac{\partial[\text{LAC}]}{\partial t} = & D_{[\text{LAC}]}\nabla^2[\text{LAC}] + K_{\text{LDH}}[\text{PYR}]\mathcal{G}_{\text{LDH}}. \end{cases} \tag{3.6}$$

The system is completed with homogeneous Neumann boundary conditions on $\partial\Omega$ and initial conditions at time $t = 0$

$$\begin{cases} [\text{GLC}](x, t = 0) = a_0(x) & x \in \Omega \\ [\text{ATP}](x, t = 0) = b_0(x) & x \in \Omega \\ [\text{ADP}](x, t = 0) = c_0(x) & x \in \Omega \\ [\text{GLY}](x, t = 0) = d_0(x) & x \in \Omega \\ [\text{PYR}](x, t = 0) = e_0(x) & x \in \Omega \\ [\text{LAC}](x, t = 0) = f_0(x) & x \in \Omega. \end{cases} \tag{3.7}$$

where $a_0, b_0, c_0, d_0, e_0, f_0 : \Omega \to \mathbb{R}$.

Precise questions on global existence of solutions of reaction-diffusion systems are still an open problem, we refer the reader to [179]. In this work, we consider all diffusion coefficients $D_{[\cdot]}$ equals, ensuring that a global solution of the system (4.6) with initial condition (3.7) exists.

3.2.3 Weak Formulation of Governing Equations

In this section we convert the strong form of the PDEs in Equation (4.6) into a corresponding weak form. This is necessary step in order to discretise both the FEM and CutFEM methods. For further details see e.g. [47].

We define the standard Hilbert space $V = v \in H^1(\Omega)$ and we denote with $\overline{V} = V \times V \times V \times V \times V \times V$ the product space.

The weak form of system (4.6) can be found multiplying each equation by a test function $v_1, v_2, v_3, v_4, v_5, v_6 \in \overline{V}$ and integrating over the space domain Ω

$$
\begin{cases}
\int_\Omega \frac{\partial[\mathrm{GLC}]}{\partial t}\, v_1 \,\mathrm{d}x = & \int_\Omega D_{[\mathrm{GLC}]}\nabla^2[\mathrm{GLC}]\, v_1 \,\mathrm{d}x + \\
& - \int_\Omega K_{\mathrm{HXK}}[\mathrm{GLC}][\mathrm{ATP}]^2\mathcal{G}_{\mathrm{HXK}}\, v_1 \,\mathrm{d}x + \int_\Omega f\, v_1 \,\mathrm{d}x \\
\int_\Omega \frac{\partial[\mathrm{ATP}]}{\partial t}\, v_2 \,\mathrm{d}x = & \int_\Omega D_{[\mathrm{ATP}]}\nabla^2[\mathrm{ATP}]\, v_2 \,\mathrm{d}x + \\
& - \int_\Omega 2K_{\mathrm{HXK}}[\mathrm{GLC}][\mathrm{ATP}]^2\mathcal{G}_{\mathrm{HXK}}\, v_2 \,\mathrm{d}x + \\
& + \int_\Omega 2K_{\mathrm{PYRK}}[\mathrm{ADP}]^2[\mathrm{GLY}]\mathcal{G}_{\mathrm{PYRK}}\, v_2 \,\mathrm{d}x + \\
& + \int_\Omega 28K_{\mathrm{Mito}}[\mathrm{PYR}]\mathcal{G}_{\mathrm{Mito}} v_2 \,\mathrm{d}x - \int_\Omega K_{\mathrm{act}}[\mathrm{ATP}]\mathcal{G}_{\mathrm{act}} v_2 \,\mathrm{d}x \\
\int_\Omega \frac{\partial[\mathrm{ADP}]}{\partial t}\, v_3 \,\mathrm{d}x = & \int_\Omega D_{[\mathrm{ADP}]}\nabla^2[\mathrm{ADP}]\, v_3 \,\mathrm{d}x + \\
& + \int_\Omega 2K_{\mathrm{HXK}}[\mathrm{GLC}][\mathrm{ATP}]^2\mathcal{G}_{\mathrm{HXK}}\, v_3 \,\mathrm{d}x + \\
& - \int_\Omega 2K_{\mathrm{PYRK}}[\mathrm{ADP}]^2[\mathrm{GLY}]\mathcal{G}_{\mathrm{PYRK}}\, v_3 \,\mathrm{d}x + \\
& + \int_\Omega K_{\mathrm{act}}[\mathrm{ATP}]\mathcal{G}_{\mathrm{act}}\, v_3 \,\mathrm{d}x \\
\int_\Omega \frac{\partial[\mathrm{GLY}]}{\partial t}\, v_4 \,\mathrm{d}x = & \int_\Omega D_{[\mathrm{GLY}]}\nabla^2[\mathrm{GLY}]\, v_4 \,\mathrm{d}x + \\
& + \int_\Omega 2K_{\mathrm{HXK}}[\mathrm{GLC}][\mathrm{ATP}]^2\mathcal{G}_{\mathrm{HXK}}\, v_4 \,\mathrm{d}x + \\
& - \int_\Omega K_{\mathrm{PYRK}}[\mathrm{ADP}]^2[\mathrm{GLY}]\mathcal{G}_{\mathrm{PYRK}}\, v_4 \,\mathrm{d}x \\
\int_\Omega \frac{\partial[\mathrm{PYR}]}{\partial t}\, v_5 \,\mathrm{d}x = & \int_\Omega D_{[\mathrm{PYR}]}\nabla^2[\mathrm{PYR}]\, v_5 \,\mathrm{d}x + \\
& + \int_\Omega K_{\mathrm{PYRK}}[\mathrm{ADP}]^2[\mathrm{GLY}]\mathcal{G}_{\mathrm{PYRK}}\, v_5 \,\mathrm{d}x + \\
& - \int_\Omega K_{\mathrm{LDH}}[\mathrm{PYR}]\mathcal{G}_{\mathrm{LDH}}\, v_5 \,\mathrm{d}x - \int_\Omega K_{\mathrm{Mito}}[\mathrm{PYR}]\mathcal{G}_{\mathrm{Mito}}\, v_5 \,\mathrm{d}x \\
\int_\Omega \frac{\partial[\mathrm{LAC}]}{\partial t}\, v_6 \,\mathrm{d}x = & \int_\Omega D_{[\mathrm{LAC}]}\nabla^2[\mathrm{LAC}]\, v_6 \,\mathrm{d}x + \int_\Omega K_{\mathrm{LDH}}[\mathrm{PYR}]\mathcal{G}_{\mathrm{LDH}}\, v_6 \,\mathrm{d}x.
\end{cases}
\tag{3.8}
$$

Since $D_{[\cdot]}$ is constant, we apply integration by parts to the second-order spatial derivative

$$
-\int_\Omega D_{[\,\cdot\,]}\nabla^2[\,\cdot\,]\, v_i \,\mathrm{d}x = \int_\Omega D_{[\,\cdot\,]}\nabla[\,\cdot\,]\,\nabla v_i \,\mathrm{d}x - \int_{\partial\Omega} D_{[\,\cdot\,]}\frac{\partial[\,\cdot\,]}{\partial n} v_i \mathrm{d}s. \tag{3.9}
$$

Since we have specified pure Neumann boundary conditions for each concentration species, the boundary terms vanish. Leading to

$$
-\int_\Omega D_{[\,\cdot\,]}\nabla^2[\,\cdot\,]\, v_i \,\mathrm{d}x = \int_\Omega D_{[\,\cdot\,]}\nabla[\,\cdot\,]\,\nabla v_i \,\mathrm{d}x. \tag{3.10}
$$

We can, then, substitute Equation (3.10) into Equation (3.8) and use the following compact notation

$$(u, v) = \int_{\Omega} uv \, \mathrm{d}x. \tag{3.11}$$

allowing us to state the weak form of the problem problem as: we seek the solutions [GLC],[ATP], [ADP],[GLY], [PYR], [LAC] in the space $\overline{V}$ such that for all $t \in [0, T]$ and for all test functions $v_1, v_2, v_3, v_4, v_5, v_6 \in \overline{V}$

$$\begin{cases} \left(\frac{\partial[\mathrm{GLC}]}{\partial t}, v_1\right) = & \left(- D_{[\mathrm{GLC}]}\nabla[\mathrm{GLC}], \nabla v_1\right) + \left(- K_{\mathrm{HXK}}[\mathrm{GLC}][\mathrm{ATP}]^2\mathcal{G}_{\mathrm{HXK}} \right. \\ & \left. + f, v_1\right) \\ \left(\frac{\partial[\mathrm{ATP}]}{\partial t}, v_2\right) = & \left(- D_{[\mathrm{ATP}]}\nabla[\mathrm{ATP}], \nabla v_2\right) + \left(- 2K_{\mathrm{HXK}}[\mathrm{GLC}][\mathrm{ATP}]^2\mathcal{G}_{\mathrm{HXK}} \right. \\ & + 2K_{\mathrm{PYRK}}[\mathrm{ADP}]^2[\mathrm{GLY}]\mathcal{G}_{\mathrm{PYRK}} + 28K_{\mathrm{Mito}}[\mathrm{PYR}]\mathcal{G}_{\mathrm{Mito}} \\ & \left. - K_{\mathrm{act}}[\mathrm{ATP}]\mathcal{G}_{\mathrm{act}}, v_2\right) \\ \left(\frac{\partial[\mathrm{ADP}]}{\partial t}, v_3\right) = & \left(- D_{[\mathrm{ADP}]}\nabla[\mathrm{ADP}], \nabla v_3\right) + \left(+ 2K_{\mathrm{HXK}}[\mathrm{GLC}][\mathrm{ATP}]^2\mathcal{G}_{\mathrm{HXK}} \right. \\ & \left. - 2K_{\mathrm{PYRK}}[\mathrm{ADP}]^2[\mathrm{GLY}]\mathcal{G}_{\mathrm{PYRK}} + K_{\mathrm{act}}[\mathrm{ATP}]\mathcal{G}_{\mathrm{act}}, v_3\right) \\ \left(\frac{\partial[\mathrm{GLY}]}{\partial t}, v_4\right) = & \left(- D_{[\mathrm{GLY}]}\nabla[\mathrm{GLY}], \nabla v_4\right) + \left(+ 2K_{\mathrm{HXK}}[\mathrm{GLC}][\mathrm{ATP}]^2\mathcal{G}_{\mathrm{HXK}} \right. \\ & \left. - K_{\mathrm{PYRK}}[\mathrm{ADP}]^2[\mathrm{GLY}]\mathcal{G}_{\mathrm{PYRK}}, v_4\right) \\ \left(\frac{\partial[\mathrm{PYR}]}{\partial t}, v_5\right) = & \left(- D_{[\mathrm{PYR}]}\nabla[\mathrm{PYR}], \nabla v_5\right) + \left(+ K_{\mathrm{PYRK}}[\mathrm{ADP}]^2[\mathrm{GLY}]\mathcal{G}_{\mathrm{PYRK}} \right. \\ & \left. - K_{\mathrm{LDH}}[\mathrm{PYR}]\mathcal{G}_{\mathrm{LDH}} - K_{\mathrm{Mito}}[\mathrm{PYR}]\mathcal{G}_{\mathrm{Mito}}, v_5\right) \\ \left(\frac{\partial[\mathrm{LAC}]}{\partial t}, v_6\right) = & \left(- D_{[\mathrm{LAC}]}\nabla[\mathrm{LAC}], \nabla v_6\right) + \left(+ K_{\mathrm{LDH}}[\mathrm{PYR}]\mathcal{G}_{\mathrm{LDH}}, v_6\right). \end{cases} \tag{3.12}$$

In the subsequent section we discuss the discretization of Equation (3.12) using the standard finite element method and the CutFEM.

3.3 Discretization

In order to solve Equation (3.12), we must discretise it in both space and time. Discretisation is a process by which continuous mathematical objects (e.g. v_1) are transformed into a discrete counterpart that can be manipulated

on a computer. We choose to discretise in space using the classical Finite Element Method [7] (FEM) and then using the Cut Finite Element Method (CutFEM) [58]. The FEM results serve as a baseline for comparison of the CutFEM method. For both FEM and CutFEM we discretize in time using a standard finite difference method.

The important distinction between FEM and CutFEM from the point of view of the user is that the FEM requires an extra mesh generation step; a mesh must be generated that conforms to the boundary of the domain, before the simulation can take place. This can be a difficult task, as the mesh must be of sufficiently good quality to ensure an accurate solution, while still conforming to the boundary. In contrast, CutFEM removes the need for a conforming mesh generation step. The boundary of the domain is described implicitly as a level set function that can be extracted directly from e.g. processed image data, or using constructive solid geometry (CSG) [195]. The promise of CutFEM is that discretization of geometry can be performed *automatically* without a mesh generation step that often requires lengthy manual intervention.

We recognise that both the Finite Element Method, and even more so, the CutFEM are highly technical and take some time to understand. The point of this section then is not to give a full and detailed exposition of both of these methods. Instead we aim show a precise derivation of the discrete weak forms and then in the subsequent section we show their translation into the FEniCS Project domain specific language, called the Unified Form Language (UFL) [10]. In practice, if the user can convert their problem into a discrete weak formulation then the the FEniCS Project and the libCutFEM library can automatically perform all of the subsequent discretization steps. For full details of how this process takes places the reader is referred to [9, 58].

3.3.1 FEM

To discretise our problem in time we choose a finite difference approximation, specifically, the backward Euler method [185]. First, we discretize the time interval $[0, T]$, denoting $\triangle t$ the size of the timestep. We denote with subscript n a concentration of (possibly multiple) chemical species at time t_n, where $0 \leq n < N$ with $N = T/\Delta t$ is an integer that counts the time steps. The

backward Euler method then approximates the continuous time derivative as

$$\frac{\partial}{\partial t}[\,\cdot\,] \approx \frac{[\,\cdot\,]_{n+1} - [\,\cdot\,]_n}{\triangle t}. \tag{3.13}$$

We discretize the spatial domain Ω using a triangulation $\mathcal{T}_h$ that conforms (matches) the exact boundary $\partial\Omega$. On this mesh we define the space of piece wise Lagrange finite elements of degree one as V and with $\overline{V}$ the product $\overline{V} = V \times V \times V \times V \times V \times V$. The space $\overline{V}$ can then be used to discretize the weak form equations (3.12).

We denote $U = ([\mathrm{GLC}], [\mathrm{ATP}], [\mathrm{ADP}], [\mathrm{GLY}], [\mathrm{PYR}], [\mathrm{LAC}])$ the vector of all the concentration solutions and $v = (v_1, v_2, v_3, v_4, v_5, v_6) \in \overline{V}$ the corresponding vector of test functions. The initial conditions are denoted $[U]_0$. We then solve a sequence of problems: find $[U]_{n+1} \in \overline{V}$ for $n = 0, \ldots, N-1$ such that

$$f_h([U]_{n+1}, [U]_n; v) = 0 \quad \forall v \in \overline{V}, \tag{3.14}$$

where

$$
\begin{aligned}
f_h([U]_{n+1},[U]_n;v) = \int_\Omega \Big(& \triangle t^{-1}([\mathrm{GLC}]_{n+1}-[\mathrm{GLC}]_n)v_1 + \\
& + D_{[\mathrm{GLC}]}\nabla[\mathrm{GLC}]_{n+1}\nabla v_1 + \\
& - f v_1 + K_{\mathrm{HXK}}[\mathrm{GLC}]_{n+1}[\mathrm{ATP}]^2_{n+1}v_1\mathcal{G}_{\mathrm{HXK}} + \\
& + \triangle t^{-1}([\mathrm{ATP}]_{n+1}-[\mathrm{ATP}]_n)v_2 + D_{[\mathrm{ATP}]}\nabla[\mathrm{ATP}]_{n+1}\nabla v_2 + \\
& + 2K_{\mathrm{HXK}}[\mathrm{GLC}]_{n+1}[\mathrm{ATP}]^2_{n+1}v_2\mathcal{G}_{\mathrm{HXK}} + \\
& - 2K_{\mathrm{PYRK}}[\mathrm{GLY}]_{n+1}[\mathrm{ADP}]^2_{n+1}v_2\mathcal{G}_{\mathrm{PYRK}} + \\
& - 28K_{\mathrm{Mito}}[\mathrm{PYR}]_{n+1}v_2\mathcal{G}_{\mathrm{Mito}} + K_{\mathrm{act}}[\mathrm{ATP}]_{n+1}v_2\mathcal{G}_{\mathrm{act}} + \\
& + \triangle t^{-1}([\mathrm{ADP}]_{n+1}-[\mathrm{ADP}]_n)v_3 + D_{[\mathrm{ADP}]}\nabla[\mathrm{ADP}]_{n+1}\nabla v_3 \\
& - 2K_{\mathrm{HXK}}[\mathrm{GLC}]_{n+1}[\mathrm{ATP}]^2_{n+1}v_3\mathcal{G}_{\mathrm{HXK}} + \\
& + 2K_{\mathrm{PYRK}}[\mathrm{GLY}]_{n+1}[\mathrm{ADP}]^2_{n+1}v_3\mathcal{G}_{\mathrm{PYRK}} + \\
& - K_{\mathrm{act}}[\mathrm{ATP}]_{n+1}v_3\mathcal{G}_{\mathrm{act}} \\
& + \triangle t^{-1}([\mathrm{GLY}]_{n+1}-[\mathrm{GLY}]_n)v_4 + D_{[\mathrm{GLY}]}\nabla[\mathrm{GLY}]_{n+1}\nabla v_4 + \\
& - 2K_{\mathrm{HXK}}[\mathrm{GLC}]_{n+1}[\mathrm{ATP}]^2_{n+1}v_4\mathcal{G}_{\mathrm{HXK}} + \\
& + K_{\mathrm{PYRK}}[\mathrm{GLY}]_{n+1}[\mathrm{ADP}]^2_{n+1}v_4\mathcal{G}_{\mathrm{PYRK}} \\
& + \triangle t^{-1}([\mathrm{PYR}]_{n+1}-[\mathrm{PYR}]_n)v_5 + D_{[\mathrm{PYR}]}\nabla[\mathrm{PYR}]_{n+1}\nabla v_5 + \\
& - K_{\mathrm{PYRK}}[\mathrm{GLY}]_{n+1}[\mathrm{ADP}]^2_{n+1}v_5\mathcal{G}_{\mathrm{PYRK}} + \\
& + K_{\mathrm{LDH}}[\mathrm{PYR}]_{n+1}v_5\mathcal{G}_{\mathrm{LDH}} + K_{\mathrm{Mito}}[\mathrm{PYR}]_{n+1}v_5\mathcal{G}_{\mathrm{Mito}} \\
& + \triangle t^{-1}([\mathrm{LAC}]_{n+1}-[\mathrm{LAC}]_n)v_6 + D_{[\mathrm{LAC}]}\nabla[\mathrm{LAC}]_{n+1}\nabla v_6 + \\
& - K_{\mathrm{LDH}}[\mathrm{PYR}]_{n+1}v_6\mathcal{G}_{\mathrm{LDH}}\Big)\,\mathrm{d}x.
\end{aligned}
\tag{3.15}
$$

Since equation (3.14) is a non-linear function of the unknown solution $[U]_{n+1}$ we choose to use a Newton-Raphson type algorithm to solve it. This Newton-Raphson algorithm requires the computation of the derivative of f_h with respect to U (commonly called the Jacobian of f_h). We do not perform this step manually, but instead use the automatic differentiation capabilities of UFL [10], as shown in Section 3.4.

3.3.2 CutFEM

Instead of discretizing the spatial domain Ω using a mesh that conforms to the boundary, in CutFEM, the problem domain Ω is described by a level-set function. The level set function is a scalar function on $\mathbb{R}^d$, such that $\phi(x) < 0$ for $x \in \Omega$, $\phi(x) > 0$ for $x \notin \Omega$ and $\phi(x) = 0$ for $x \in \partial\Omega$. We then cover the domain Ω by a regular background mesh Λ ($\Omega \subseteq \Lambda$) of simple shape, e.g. a box containing Ω meshed with a uniform triangulation. Let K denote a triangle/tetrahedron in this triangulation. Now, let $\tilde{\mathcal{T}}_h$ be the fictitious domain mesh composed by all elements $K \in \Lambda$ such that $K \cap \Omega \neq 0$ ($\Omega \subseteq \tilde{\mathcal{T}}_h \subseteq \Lambda$).

Furthermore, the union of all elements in $\tilde{\mathcal{T}}_h$ is called the fictitious domain $\tilde{\Omega}$. We denote with

$$\mathcal{G}_h^* := \{K \in \tilde{\mathcal{T}}_h : K \cap \partial\Omega \neq \emptyset\}$$

the set of elements intersected by the interface, and we define the set of so-called ghost penalty facets [57] (see Figure 3.2

$$\mathcal{F}_G = \{F \text{ facet in } \tilde{\mathcal{T}}_h : F = K \cap K' \quad \text{where} \quad K \in \mathcal{G}_h^* \quad \text{or} \quad K' \in \mathcal{G}_h^*\}.$$

The stabilisation term introduced in the next section will be applied to this subset of facets. We consider the space

$$W = \{v \in C^0(\tilde{\Omega}) : v|_K \in P^1(K), \forall K \in \tilde{\mathcal{T}}_h\}$$

and the jump gradient is defined for all facet F and $v \in W$ by $[\![\partial_{n_F} v]\!] = n_F \cdot \nabla v|_K - n_F \cdot \nabla|_{K'}$ where n_F denotes the unit normal to F in fixed but arbitrary direction. We use the same notation as the previous section, denoting the solution $U = ([\text{GLC}], [\text{ATP}], [\text{ADP}], [\text{GLY}], [\text{PYR}], [\text{LAC}])$, $v = (v_1, v_2, v_3, v_4, v_5, v_6)$ and the product space $\overline{W} = W \times W \times W \times W \times W \times W$, We then solve a sequence of problems: find $[U]_{n+1} \in \overline{V}$ for $n = 0, \ldots, n-1$ such that

$$f_h([U]_{n+1}, [U]_n; v) + j([U]_{n+1}, v) = 0 \quad \forall v \in \overline{W} \tag{3.16}$$

where $f_h([U]_{n+1}, [U]_n; v)$ is identical to the standard FEM Equation (3.15). Here, $j([U]_{n+1}, v)$ denotes the following stabilization terms

$$\begin{aligned} j([U]_{n+1}, v) = \sum_{F \in \mathcal{F}_G} \big(& (\gamma h D_{[\mathrm{GLC}]} [\![\partial_{n_F} [\mathrm{GLC}]_{n+1}]\!], [\![\partial_{n_F} v_1]\!])_F \\ & + (\gamma h D_{[\mathrm{ATP}]} [\![\partial_{n_F} [\mathrm{ATP}]_{n+1}]\!], [\![\partial_{n_F} v_2]\!])_F \\ & + (\gamma h D_{[\mathrm{ADP}]} [\![\partial_{n_F} [\mathrm{ADP}]_{n+1}]\!], [\![\partial_{n_F} v_3]\!])_F \\ & + (\gamma h D_{[\mathrm{GLY}]} [\![\partial_{n_F} [\mathrm{GLY}]_{n+1}]\!], [\![\partial_{n_F} v_4]\!])_F \\ & + (\gamma h D_{[\mathrm{PYR}]} [\![\partial_{n_F} [\mathrm{PYR}]_{n+1}]\!], [\![\partial_{n_F} v_5]\!])_F \\ & + (\gamma h D_{[\mathrm{LAC}]} [\![\partial_{n_F} [\mathrm{LAC}]_{n+1}]\!], [\![\partial_{n_F} v_6]\!])_F \big) \end{aligned} \tag{3.17}$$

inspired by [58]. Here, γ is a positive penalty parameter. These stabilization terms extend the solution from the physical domain Ω onto the fictitious domain $\tilde{\Omega}$, it is consistent with the continuous system. They prevent ill-conditioning of the system matrices in case only small parts of Ω are contained in an element near the boundary $\partial\Omega$. This stabilisation is critical for the robustness and reliability of CutFEM.

3.4 Implementation

The finite element method discretization has been implemented using Python with the open source finite element solver DOLFIN from the FEniCS Project, see [138, 9]. The CutFEM discretization has been implemented using Python using the libCutFEM library [58] which builds on top of DOLFIN and the rest of the FEniCS Project. In this section we show *parts* of the code for the libCutFEM example that highlight the close link between the mathematics and the concrete computer implementation. The standard FEniCS Project implementation is similar so we have chosen to show only the libCutFEM implementation for reasons of brevity. The reader should refer to the free online repository for two full working examples that are around 250 lines of code each. The precise problem setup and results from this example are shown in Section 3.5.3.

We import the `dolfin` and `cutfem` Python modules. These two modules contain all of the functionality we need to solve the problem using the CutFEM approach.

```
from dolfin import *
from cutfem import *
```

We create the background mesh Λ and then define a level set function describing the heart-shaped domain.

```
# Create background mesh
bg_mesh = RectangleMesh(-1, -1, 1., 2., N, N)
...
# Define heart-shaped level set function
level_set = Expression('x[0] < 0. ? pow(x[1] - sqrt(-x[0]), 2)
    -1 + pow(x[0], 2): pow(x[1] - sqrt(x[0]), 2) - 1 + pow(x[0],
     2)', degree=2)
```

In the next part of the code, we use two special libCutFEM methods to 1. create a special cut `mesh`, and 2. a `mesh_cutter` that intersects the mesh with the level set and computes the distinct sets of cells (i.e. those that are on the inside of the level set and those that are outside).

```
# Define fictitious domain
mesh = CutFEMTools_fictitious_domain_mesh(bg_mesh, level_set,
    0, 0)
...
# Compute mesh to levelset intersection and corresponding
    marker
mesh_cutter = MeshCutter(mesh, level_set)
```

With these special objects in hand we can define special CutFEM-specific UFL `Measure` objects that will subsequently allow us to write the residual and the stabilisation weak forms. Simply put, a measure defines regions of the problem mesh (cells, edges, parts inside the level set, and parts outside etc.) on which FEniCS will integrate different parts of a weak form.

```
# Measure on all the cells having an intersection with the
    levelset
# Marker 0 if the cell have an intersection with \{ level set <
     0 \}  and 1 otherwise
```

```
dx = Measure("dx")[mesh_cutter.domain_marker()]
# Measure on the fictitious boundary defined by the level set
# Marker 0 if the facet have an intersection with \{ level set < 0 \}  and 1 otherwise
dS = Measure("dS")[mesh_cutter.interior_facet_marker(0)]
# Measure on the interior part of cells cut by the level set
dxq = dc(0, metadata={"num_cells": 1})

# We combine the measure on the inside of the domain and the measure
# on the interior part of the cut cells
dxc = dx(0) + dxq
```

We create a finite element function space $\bar{V}$ that we can use to further define the UFL algebraic objects that we need.

```
V = FunctionSpace(mesh, "P", 1)
V_bar = MixedFunctionSpace([V, V, V, V, V, V])
v = TestFunction(V_bar)
v_1, v_2, v_3, v_4, v_5, v_6 = v.split()
```

Now we have everything that we need to write the weak residual $f_h([U]_{n+1}, [U]_n; v)$ in Equation (3.14) using the UFL. We use the integration measure `dxc` which indicates the integration on cells inside the domain Ω and in parts of the cut cells inside Ω. This form would look identical in the standard FEniCS Project code except that we would use the `dx` measure that denotes integration over all cells of the mesh.

```
...
u = Function(V_bar)
u_n = project(u_0, V_bar) # Initial condition, details not shown
# Solution at next timestep
a, b, c, d, e, f = u.split() # GLC, ATP, ADP, GLY, PYR, LAC
# Solution at current timestep
a_n, b_n, c_n, d_n, e_n, f_n = u_n.split()

F = ((a - a_n) / k)*v_1*dxc + D_glc*dot(grad(a), grad(v_1))*dxc
    + K_hxk*a*b**2*v_1*g_hxk*dxc - f_glc*v_1*dxc + ((b - b_n) /
    k)*v_2*dxc + D_atp*dot(grad(b), grad(v_2))*dxc + 2*K_hxk*a*
```

```
    b**2*v_2*g_hxk*dxc - 2*K_pyrk*d*c**2*v_2*g_pyrk*dxc - 28*
    K_Mito*e*v_2*g_mito*dxc + K_act*b*v_2*g_act*dxc + ((c - c_n)
     / k)*v_3*dxc + D_adp*dot(grad(c), grad(v_3))*dxc - 2*K_hxk*
    a*b**2*v_3*g_hxk*dxc + 2*K_pyrk*d*c**2*v_3*g_pyrk*dxc -
    K_act*b*v_3*g_act*dxc + ((d - d_n) / k)*v_4*dxc + D_gly*dot(
    grad(d), grad(v_4))*dxc - 2*K_hxk*a*b**2*v_4*g_hxk*dxc +
    K_pyrk*d*c**2*v_4*g_pyrk*dxc + ((e - e_n) / k)*v_5*dxc +
    D_pyr*dot(grad(e), grad(v_5))*dxc - K_pyrk*d*c**2*v_5*g_pyrk
    *dxc + K_ldh*e*v_5*g_ldh*dxc + K_Mito*e*v_5*g_mito*dxc + ((f
     - f_n) / k)*v_6*dxc + D_lac*dot(grad(f), grad(v_6))*dxc -
    K_ldh*e*v_6*g_ldh*dxc
```

The stabilization term $j([U]_{n+1}, v)$ Equation (3.17) is written in UFL using the integration measure `dS(1)` which integrates on the ghost penalty facets $\mathcal{F}_G$ (Figure 3.4).

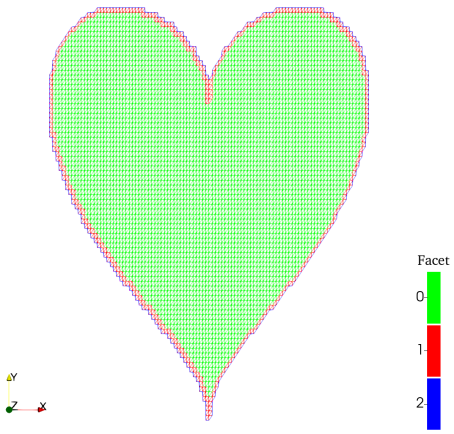

Fig. 3.4 We can see the fictitious domain $\tilde{\Omega}$ for the heart shaped function, and the facets marked. In red the set of facets $\mathcal{F}_G$ where we apply the stabilization term $j([U]_{n+1}, v)$.

```
1 j = avg(gamma)*avg(h)*D_glc*dot(jump(grad(a), n), jump(grad(v_1
    ), n))*dS(1) + avg(gamma)*avg(h)*D_atp*dot(jump(grad(b), n),
     jump(grad(v_2), n))*dS(1) + avg(gamma)*avg(h)*D_adp*dot(
    jump(grad(c), n), jump(grad(v_3), n))*dS(1) + avg(gamma)*avg
    (h)*D_gly*dot(jump(grad(d), n), jump(grad(v_4), n))*dS(1) +
    avg(gamma)*avg(h)*D_pyr*dot(jump(grad(e), n), jump(grad(v_5)
    , n))*dS(1) + avg(gamma)*avg(h)*D_lac*dot(jump(grad(f), n),
    jump(grad(v_6), n))*dS(1)
```

For both forms `F` and `j` we remark how similar the UFL notation is to the mathematical notation in Equation (3.14) and Equation (3.17). Calculating the UFL expression for the Jacobian $\mathbb{J}$ can be performed automatically using the `derivative` function.

```
F += j
J = derivative(F, u)
```

The last step before the solver is to use the Composite framework of CutFEM to define the problem on different parts of the mesh domain.

```
# Fictitious domain
composite_mesh = CompositeMesh()
composite_mesh.add(mesh)

W = CompositeFunctionSpace(composite_mesh)
W.add(V_bar);
W.build();

# Constrain dofs outside
FidoTools_compute_constrained_dofs(W, mesh_cutter)

a = FidoForm(W,W)
form_a = create_dolfin_form(J)
a.add(form_a, mesh_cutter)

L = FidoForm(W)
form_L = create_dolfin_form(F)
L.add(form_L, mesh_cutter);
```

Eventually, we can solve the non-linear and time-dependent problem with the following two nested loops, the outer one for the timestepping, and the inner one for the Newton-Raphson algorithm. The FEniCS Project infrastructure (UFL+FFC+DOLFIN) automatically generates and executes low-level code to assemble the sparse matrices `A` and `b`. This linear system is then solved using PETSc and MUMPS.

```
...
# Timestep loop
max_iters = 50
toll_a = 1.e-10
for i in range(num_steps):
    j = 0
    # Newton-Raphson algorithm
    while j < max_iters:
        A = composite_assemble(a)
        b = composite_assemble(L)

        uc = CompositeFunction(W)

        # Solve linear system for Newton step using MUMPS
    direct solver
        solve(A, uc.vector(), -b, 'mumps')

        # Newton update
        u.vector().axpy(1.0, uc.part(0).vector())

        # Terminate if tolerance reached
        if uc.part(0).vector().norm("l2") < toll_a:
            break
        else:
            j += 1

    ...
    # Update the solution
    u_n._assign(u)
    # Update the time step
    t[0] = t[0] + dt
    # Update the source term
    f_glc.t = t[0]
```

In the previous piece of code, we used the increment as stopping criteria for the Newton-Raphson algorithm. We refer the reader to the free online repository with an example where the stopping criteria is the tolerance to the residual. In the full example, in the free online repository the solution at each timestep is outputted to a VTK file that can be opened with Paraview (https://paraview.org) for visualisation.

3.5 Numerical Results

In this section we evaluate the accuracy of the CutFEM discretisation scheme for different geometries by comparing the CutFEM solution to the standard FEM solution. In addition, we want to confirm that at the steady state solutions (for large values of time t) predicted by CutFEM tend towards the asymptotic solutions of the associated ordinary differential equation (ODE) system. Then, we investigate the accuracy of CutFEM in comparison with the standard FEM for a simple circular geometry. We increase the complexity of the geometry and we show the ability of CutFEM to straightforwardly solve a test case within a non-Lipschitz domain. Lastly, we consider a three dimensional domain.

The numerical scheme was implemented using the CutFEM library [58] based on FEniCS Project [9, 138, 110]. The linear systems arising in the numerical experiments are solved using a direct (MUMPS) solver for the two-dimensional examples and a iterative (CG) solver with algebraic multigrid preconditioning (hypre) for the three-dimensional example.

3.5.1 Asymptotic Solution ODEs

The aim of this section is to validate our CutFEM implementation highlight that the solution of the reaction-diffusion system tends to the solution of the ODE system associated to the chemical reactions Equations (4.1)-(4.5) for time going to infinity. The solution of the ODE system is computed in two ways 1. we use the *solve_ivp* of the package *scipy* in python 2. we manually compute the asymptotic solutions, which can be found in Appendix A.1 together with the ODE system in Equation (A.1).

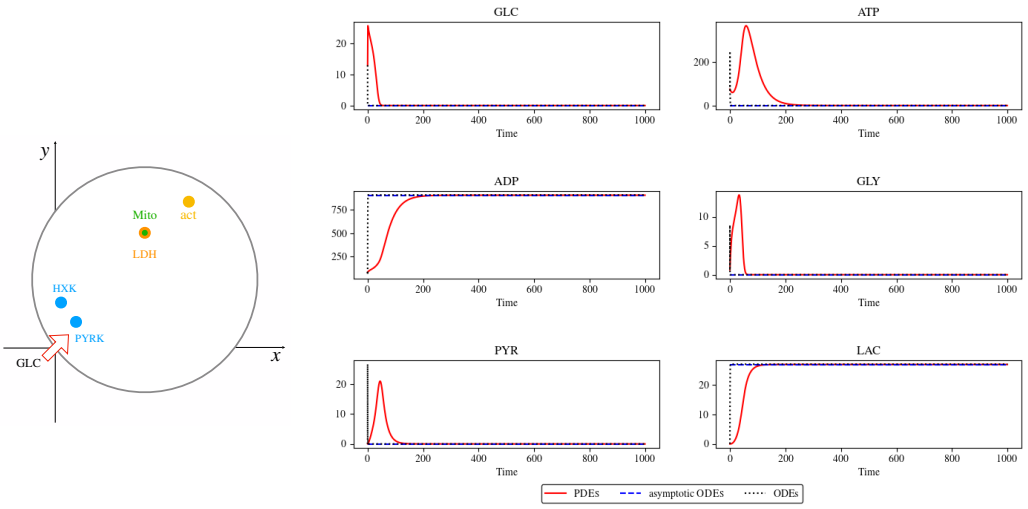

(a) (b)

Fig. 3.5 (a) The locations of the chemical reactions Equations (4.1)-(4.5) and the influx of GLC are shown in the circular domain in order to prove the convergence of the PDEs solutions to the ODEs. Note, the chemical reactions LDH Equation (4.3) and Mito Equation (4.4) have been placed in the same location. (b) The solutions of the PDEs obtained using CutFEM and integrated over the domain (red line) are plot in comparison with the asymptotic solutions of the ODEs for each concentration (blue line) and with the ODEs solved using *scipy*. The convergence of the PDEs to the ODEs solutions is reached for $t > 200$.

For the PDEs, we solve the reaction diffusion system in a circular domain defined in CutFEM using the level set function $\phi(x, y) = (x-4)^2+(y-3)^2-25$. The Gaussian parameters locating the chemical reactions, that are shown in Figure 3.5a, have been set as following: $\mathcal{G}_{\text{HXK}}(x_0 = 0.5, y_0 = 2.0, \sigma = 0.1)$, $\mathcal{G}_{\text{PYRK}}(x_0 = 1.1, y_0 = 1.2, \sigma = 0.1)$, $\mathcal{G}_{\text{LDH}}(x_0 = 4.0, y_0 = 5.0, \sigma = 0.1)$, $\mathcal{G}_{\text{Mito}}(x_0 = 4.0, y_0 = 5.0, \sigma = 0.1)$ and $\mathcal{G}_{\text{act}}(x_0 = 6.0, y_0 = 6.5, \sigma = 0.1)$. Note, we have co-localized the reactions (4.3) and (4.4), in order to obtain that PYR is used equally in the two reactions, such that we can set the parameter α of the ODE asymptotic solutions of Equation (A.3) equal to 0.5.

The influx of GLC entering the cell domain has been set equal to 100 until time $t = 1$ and is entering the cell into a circular subdomain with radius 0.3 and center the origin.

The rate constants $K_\cdot$ of the chemical reactions are set equal to 10.0, in order to avoid that one reaction dominates over, and the diffusive parameters

$D_{[\cdot]}$ of each chemical species is 100.0 to accelerate the convergence to the ODEs solutions. The initial amount of concentrations inside the cell are set to zero except for [ATP] and [ADP] that are equal to 1. Final time is 1000, as well as the number of time step. The CutFEM penalty parameter γ has been set equal to 0.1. The mesh size is set to a maximum diameter of 0.1744. In this experiment, a finer mesh is not required for proving the convergence to the ODEs solutions.

As initial condition, the asymptotic ODEs use the solution of PDEs at time equal to 1 when the source term of glucose stops, which keeps the total amounts of concentration unchanged, as shown in Appendix A.1.

To use *scipy* to solve the ODEs we set all the parameters as the PDEs, the influx of GLC and the initial conditions are obtained from the PDE ones integrating over the domain.

In order to compare the numerical solution of the system (4.6) solved using CutFEM, we integrate the solutions of the concentrations over the domain Ω to obtain the average chemical concentration of each species at each time step. We use the following notation

$$\tilde{[\cdot]}(t) := \int_\Omega [\cdot](t)\, \mathrm{d}x \quad \forall t \in [0, T]. \tag{3.18}$$

In Figure 3.5b, we plot the solutions obtained using the Formula (3.18) for the PDEs, the asymptotic ODE solutions obtained using Equation (A.3) and the ODE solutions with *scipy*. As expected from the asymptotic solutions computed in Appendix A.1, the average concentrations of GLC, ATP, GLY and PYR go to zero whilst the products of the system are LAC and ADP. We can see that the ODE solutions with *scipy* converge to the asymptotic solution very quickly, and after time $t = 200$ also the PDE solutions tend to the same values.

3.5.2 Two-dimensional Circular Domain

In this section, we assess the accuracy of the CutFEM solution. First, we consider the cell, Ω, as a circle defined by the level set function $\phi(x, y) = (x-4)^2 + (y-3)^2 - 25$ and we show that the results obtained with CutFEM

are of the same order as those obtained with FEM, where the circular domain is explicitly meshed using package mshr.

To investigate the behaviour of CutFEM for more complex boundaries we consider an irregular cell geometry defined by a perturbed circle represented by the level set function $\phi(x, y) = (x-4)^2 + (y-3)^2 - \cos(4x)\cos(5x) - \sin(4y)\cos(5y) - 25$. We highlight how it is easy for CutFEM to work with a more complex shape just by changing the level set function.

In this experiment the glucose source term and the reaction locations and parameters are set as in section 3.5.1, with the exception of the Mito reaction that is located at $\mathcal{G}_{\text{Mito}}(x_0 = 4.0, y_0 = 7.5, \sigma = 0.1)$. The test case is represented schematically in Figure 3.6a.

The chemical species are allowed to diffuse inside the cell with diffusive constants $D_{[\cdot]} = 1.0$ for each species. The rate constants of the chemical reaction and the initial chemical concentrations are set as in the previous test case, see Section 3.5.1. Final time is 10 and we set the number of time steps as 300. As before, the penalty parameter of CutFEM is set to 0.1. The choice of the mesh size is shown in Table 3.1 in accordance with the size of the Gaussian parameters σ.

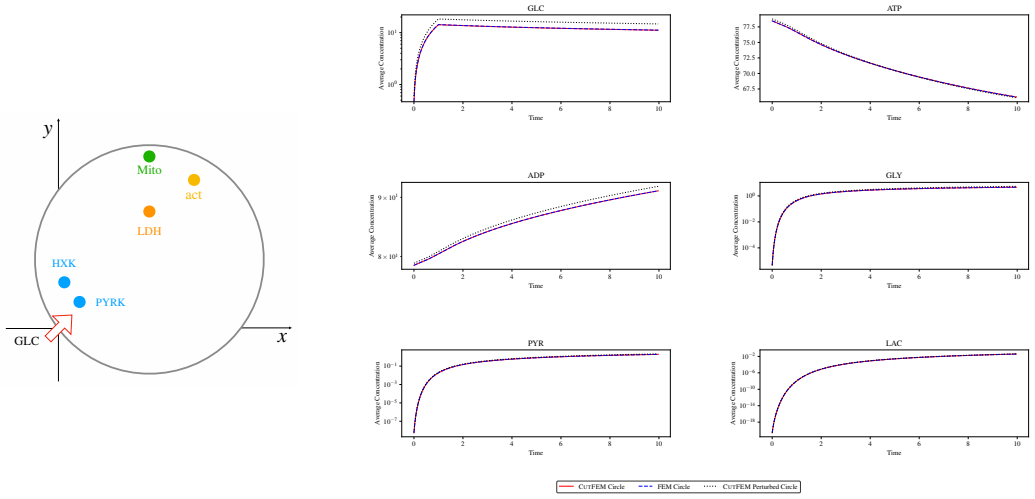

(a) (b)

Fig. 3.6 (a) The chosen location of the chemical reactions Equations (4.1)-(4.5) and of the influx of GLC are shown to compare FEM and CutFEMresults in a circular domain. (b) In the y-axis is plot the integral over the domain at each time step using Equation (3.18), giving us the average concentration, of CutFEM and FEM in a circular domain and CutFEM solved in a circular domain with perturbed boundary. The average concentration of each species of FEM (blue line) and CutFEM (red line) are equivalent while the CutFEM solutions of the perturbed domain (black line) share the same results for concentrations ATP, GLY, PYR, LAC and differs but show the same trend for GLC and ADP.

	Maximum Cell Diameter	DOF	Computational Time
Circle FEM	0.049999	477114	4 h 30 m
Circle CutFEM	0.049741	387786	23 h
Perturbed Circle CutFEM	0.048893	402288	21 h

Table 3.1 In the table shows the maximum cell diameter, the number of DOFs, and the computational time for FEM and CutFEM in a circular domain and for CutFEM for the perturbed boundary domain.

In Figure 3.6b, we investigate the average concentrations inside the three domains at each time step using Equation (3.18). The average concentrations for each species computed in the circular domain with FEM and CutFEM show equivalent results. The solutions obtained using the perturbed domain show higher average concentration of GLC and ADP than the results in the circular domain. We remind the reader that the system solved inside the perturbed

domain is not supposed to produce same results as the circular one, however the dynamics show the same trend as shown in Figure 3.6b.

For time equal to 5, we plot the solutions of the concentrations for each chemical species in Table 3.2. We notice how the Gaussian functions drive the chemical reactions in the regions defined in Figure 3.6a. For example, we can notice that ATP is consumed in two regions that locate respectively HXK and act, while ADP is produced. The GLC entered the cell is diffusing in the domain and taking part to the HXK reaction. In comparison, the results of FEM and CutFEM are almost identical.

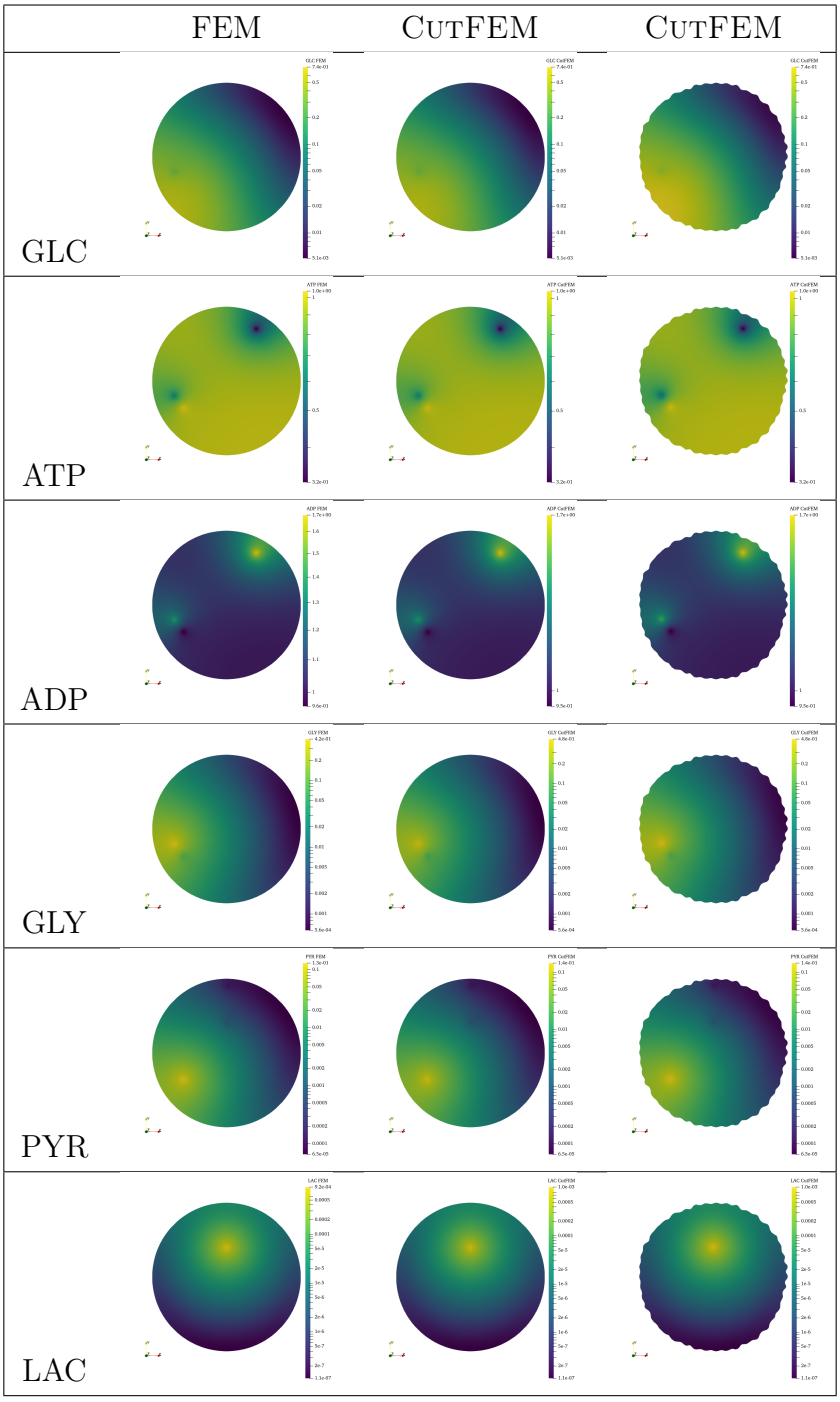

Table 3.2 Solutions of the concentrations, from top to bottom: GLC, ATP, ADP, GLY, PYR and LAC, at time $t = 5$ in a circular domain solved with FEM (Left), CutFEM (Center) and CutFEM in a perturbed boundary (Right). The source term of GLC is no longer active, and the quantity of GLC is spreading through the domain and participating into the reaction HXK. ATP and ADP show that in the region where HXK, PYRK and act are located, when one is consumed the other is produced. We can notice production of GLY, PYR and LAC. Comparing the results in the three domain, they are extremely close to each other and visually not distinguishable.

To further analyze the plot shown in Table 3.2, we compare in Figure 3.7 FEM and CutFEM solutions line $x = y$ at time 5 (Figure 3.7a) and final time 10 (Figure 3.7b). We can recognize where the reactions are from the bump in the curve. The plot indicates that the results are equivalent.

Our experiments suggest that CutFEM produces similar solutions to the FEM but the computational time needed to solve CutFEM is five times as high as standard FEM. The number of DOFs is smaller for CutFEM compared to FEM, as shown in Table 3.1.

Concerning the larger computational time requires for CutFEM, the CutFEM implementation is based on FEniCS 1.5.0 released in 2015, while the FEM ones on FEniCS 2019.1.0 released in 2019 with significant improvements and computational optimizations. Since CutFEM relies in large parts on the FEniCS functions, its computational time would be highly reduced when using a newer version of FEniCS. Breaking down the total computational time, we identified that the CutFEM implementation of assembly is significantly slower than the FEniCS implementation of assembly. However, critically, we have verified that both implementations scale at the expected optimal rate $O(N)$ in the number of cells N (results not shown). The larger constant in the $O(N)$ scaling in the CutFEM implementation points to certain computational kernels not optimised for efficiency.

In conclusion, in this section we showed how CutFEM and FEM gives equivalent results for a circular domain. Moreover, we investigated the behaviour of CutFEM with a more complex domain, the perturbed circle.

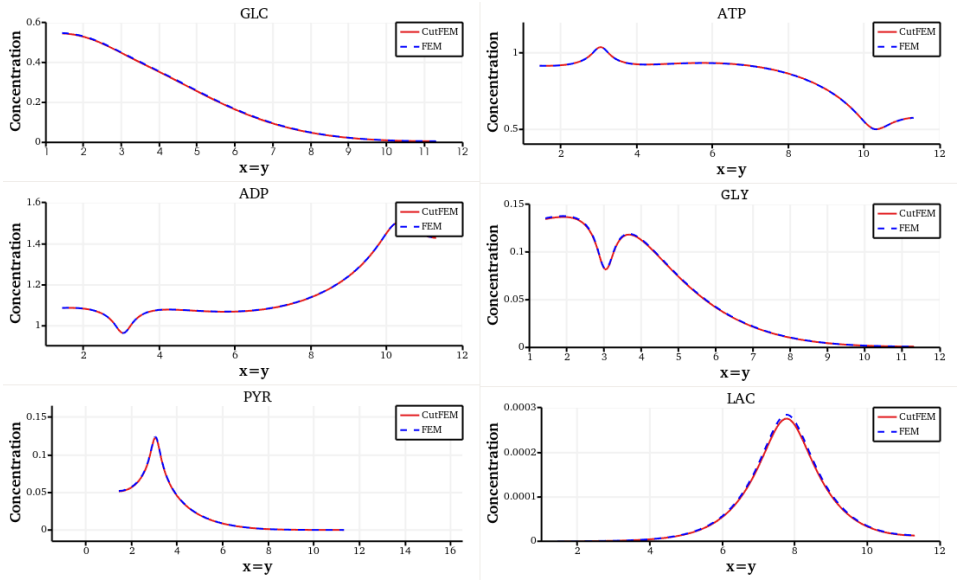

(a) t=5

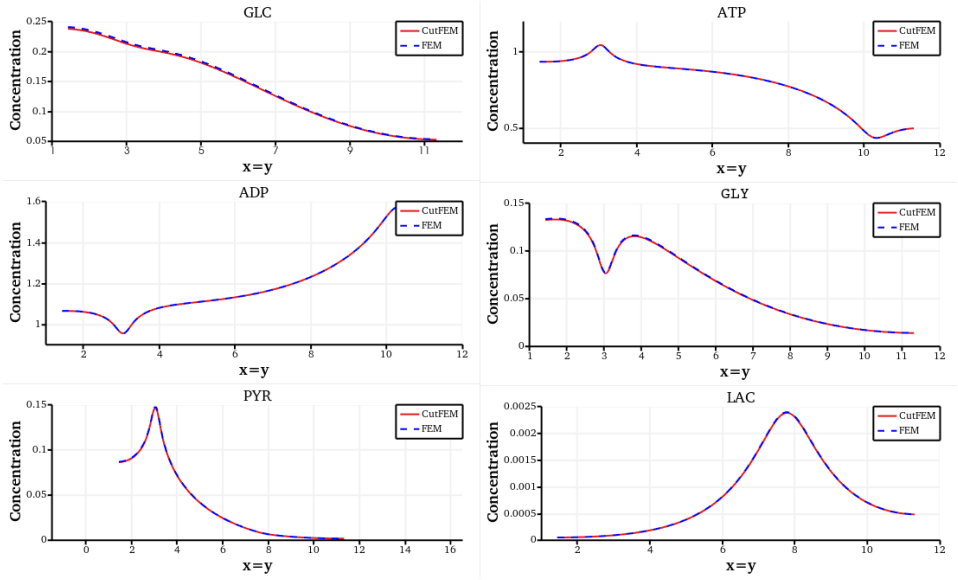

(b) t=10

Fig. 3.7 We plot the solutions of the concentrations in a circular domain obtained with FEM and CutFEM along the line $x = y$ at time $t = 5$ (a) and final time $T = 10$ (b). We can notice in the plot the location where the reactions are happening thanks to the bump in the plot. The only small differences detectable are in LAC at $t = 5$ and in GLC at $t = 10$ where CutFEM is slightly below the FEM curve.

3.5.3 Two-dimensional non-Lipschitz Domain

In this section, we consider an irregular boundary, i.e. where the normal field along the surface is non-smooth. We choose a heart-shaped domain, which has two singularities (this is known as a non-Lipschitz domain).

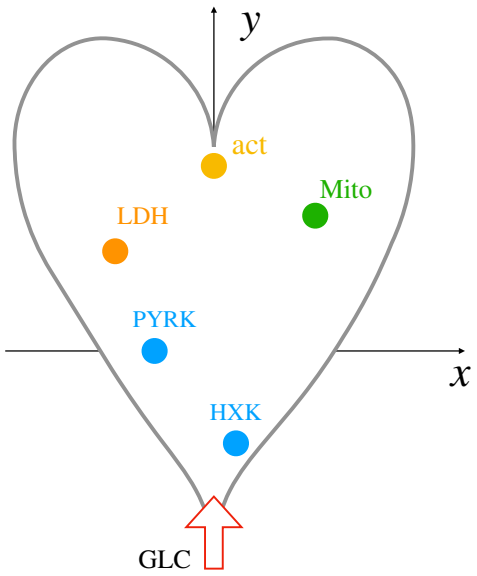

Fig. 3.8 Location of the chemical reactions Equations (4.1)-(4.5) and the source term of GLC in the heart shaped domain.

The heart-shaped is described by the level set function $\phi(x, y) = (y - \sqrt{|x|})^2 - 1 + x^2$. The description of the problem setting is shown in Figure 3.8. The gaussian functions are defined as $\mathcal{G}_{\text{HXK}}(x_0 = 0.1, y_0 = -0.5, \sigma = 0.1)$, $\mathcal{G}_{\text{PYRK}}(x_0 = 0.3, y_0 = 10.0, \sigma = 0.1)$, $\mathcal{G}_{\text{LDH}}(x_0 = -0.5, y_0 = 0.5, \sigma = 0.1)$, $\mathcal{G}_{\text{Mito}}(x_0 = 0.5, y_0 = 0.7, \sigma = 0.1)$ and $\mathcal{G}_{\text{act}}(x_0 = 0.0, y_0 = 0.9, \sigma = 0.1)$. We consider a source term for GLC active within a disk of radius 0.3, centered at the cusp and take the GLC influx to be 100.

The diffusive constants, the reaction rate and the initial concentrations are as in Section 3.5.2, as well as the penalty parameter for the stabilization term.

We solve the reaction diffusion system (4.6) using CutFEM, where we have set a background mesh with a maximum cell diameter equal to 0.01803, the number of DOFs is 129,606 and the total time to run the simulation was approximately 4 hours.

Figure 3.9 and Figure 3.10 show the solutions obtained in the heart-shaped domain for each chemical species at the initial and final time. At the initial time, we can see how the GLC (Figure 3.9a) enters the cellular domain, diffuses and takes part in HXK. On the other hand, the region where the reaction act (consuming ATP and producing ADP) is clearly visible (Figure 3.9b-3.9c). Observing the plot of GLY (Figure 3.9d) we can see the region where GLY is produced by HXK and at the same time consumed by PYRK. Interestingly, we can notice that at the initial time, the PYR produced by PYRK contributes to generating LAC, however PYR has not reached the Mito reaction site, so that there is no production of ATP from this reaction (Figures 3.9e-3.9f).

At the final time ($T = 10$), the GLC has diffused into the domain, and is still used to generate HXK (Figure 3.10a). Concentrations ADP, PYR and LAC have reached a stable state (Figure 3.10c-3.10e-3.10f), while ATP is consumed by the act reaction and is produced by the Mito reaction (Figure 3.10b). GLY is still consumed by PYRK and produced by HXK (Figure 3.10d).

Briefly, we observe that CutFEM solves the test case inside the heart shaped domain, the singularities are well described thanks to the choice of a fine mesh. The computational time of CutFEM in this test case is smaller than in the previous experiment since the number of DOFS is 4 times less then the previous test case.

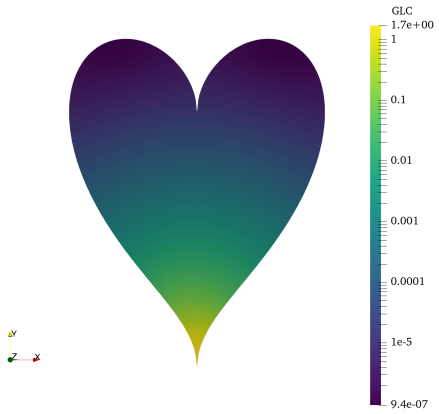

(a) GLC

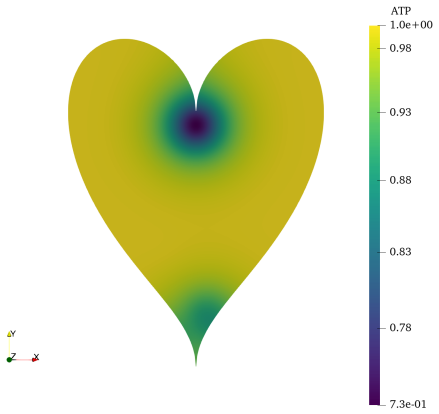

(b) ATP

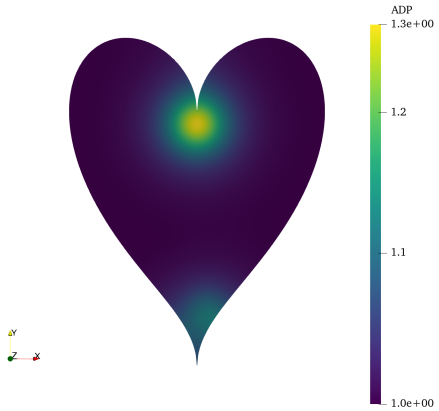

(c) ADP

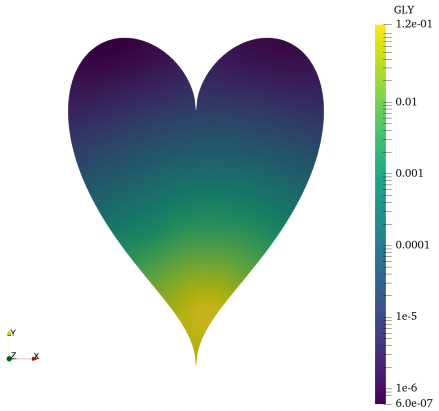

(d) GLY

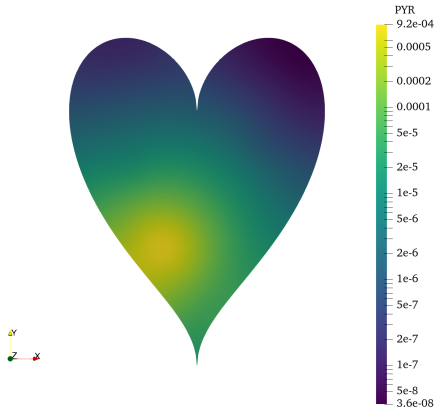

(e) PYR

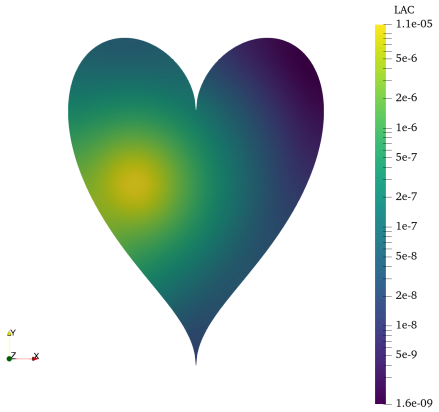

(f) LAC

Fig. 3.9 Solutions of the Model obtained in a heart-shaped domain at the Initial time (t=0). GLC is entering the domain from the infimum of the domain. ATP is used in the region where act and HXK are located, vice versa ADP is produced. GLY is produced from HXK. We can see PYR and LAC produced by PYRK and LDH, respectively.

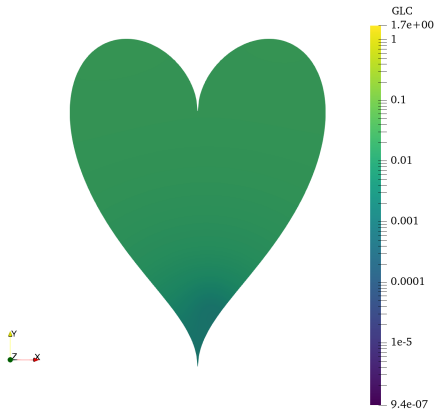

(a) GLC

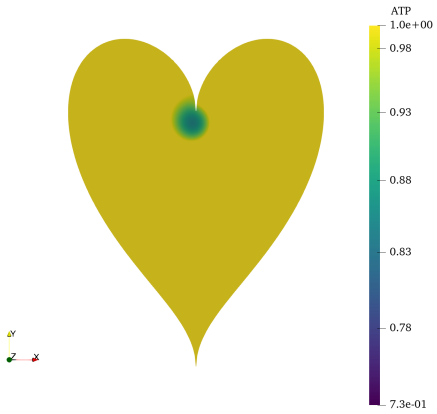

(b) ATP

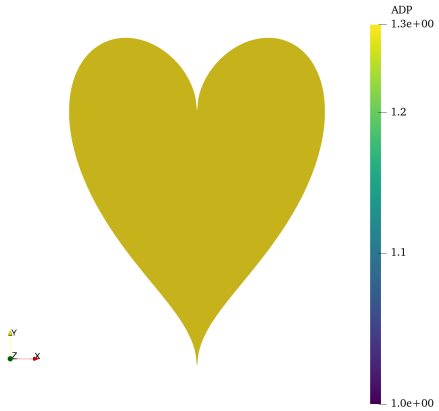

(c) ADP

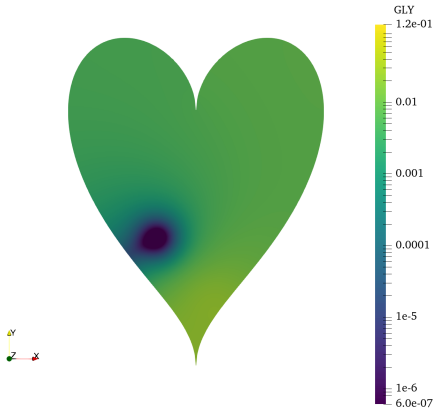

(d) GLY

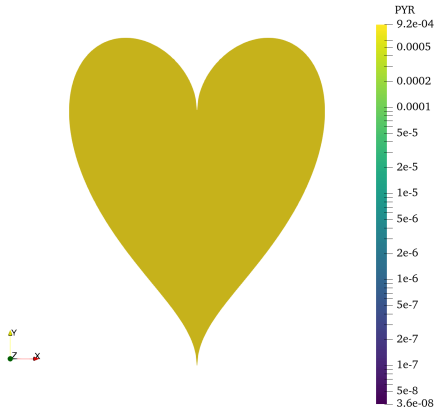

(e) PYR

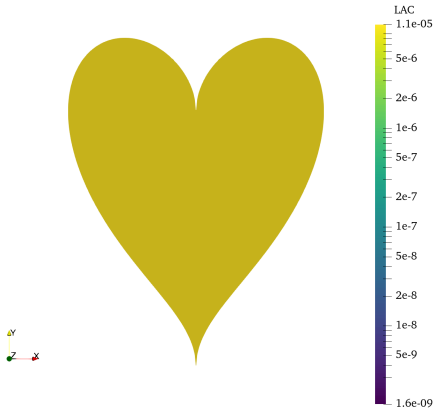

(f) LAC

Fig. 3.10 Solution of the Model obtained in a heart-shaped domain at the final time (T=10). From top to bottom from left to right: [GLC], [ATP], [ADP], [GLY], [PYR], [LAC]. GLC is still consumed in the infimum where HXK is. ADP, PYR and LAC have reached a state where the amount of concentration is uniformly distributed into the domain. ATP is consumed to produce ADP by act and produced by the Mito reaction. GLY is consumed by PYRK and produced by HXK.

3.5.4 Three-dimensional Complex Domain

For the last experiment, we work with a 3 dimensional domain. We consider a union of six spheres that generate a pop-corn shape. To create the shape we use the union of the following level set functions

$$\begin{aligned}
\phi_1(x,y,z) &= (x-4)^2 + (y-3)^2 + z^2 - 25 \\
\phi_2(x,y,z) &= (x-12)^2 + (y-3)^2 + z^2 - 25 \\
\phi_3(x,y,z) &= (x-8)^2 + (y-7)^2 + z^2 - 25 \\
\phi_4(x,y,z) &= (x-8)^2 + (y+1)^2 + z^2 - 25 \\
\phi_5(x,y,z) &= (x-8)^2 + (y-3)^2 + (z+4)^2 - 25 \\
\phi_6(x,y,z) &= (x-8)^2 + (y-3)^2 + (z-4)^2 - 25
\end{aligned}$$

We sketch in Figure 3.11a the problem setting projected onto the xy plane. The parameters chosen for the reaction locations are: $\mathcal{G}_{\text{HXK}}(x_0 = 0.5, y0 = 2.0, z_0 = 0.0, \sigma = 0.5)$, $\mathcal{G}_{\text{PYRK}}(x_0 = 1.1, y_0 = 1.2, z_0 = 0.0, \sigma = 0.5)$, $\mathcal{G}_{\text{LDH}}(x_0 = 4.0, y_0 = 5.0, z_0 = 0.0, \sigma = 0.5)$, $\mathcal{G}_{\text{Mito}}(x_0 = 4.0, y_0 = 7.5, z_0 = 0.0, \sigma = 0.5)$ and $\mathcal{G}_{\text{act}}(x_0 = 6.0, y_0 = 8.5, z_0 = 0.0, \sigma = 0.5)$. The source term is located in a ball of radius 0.3 centered on the origin, and we increase the source influx to 1,000 until time 1. The diffusive constants, the reaction rates and the initial conditions are set as in Section 3.5.2.

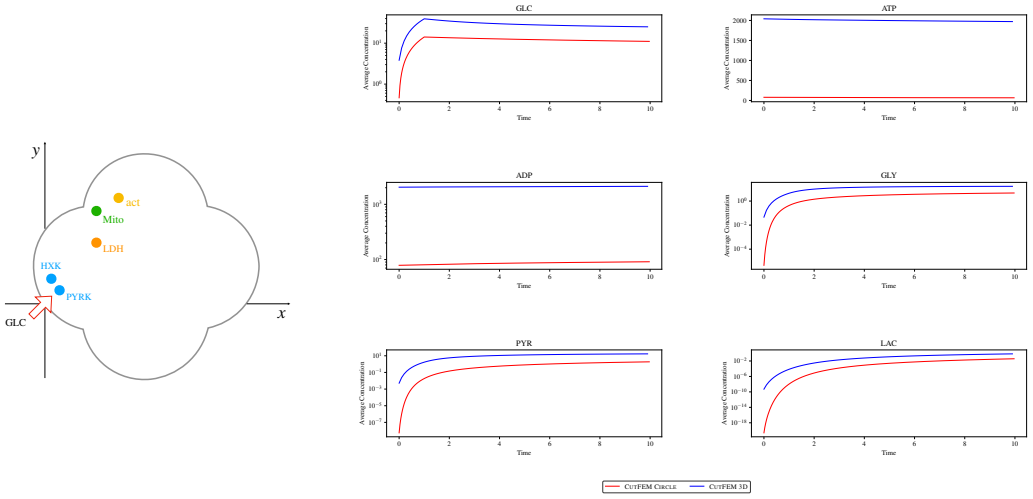

(a) (b)

Fig. 3.11 (a) Setting of chemical reactions Equations (4.1)-(4.5) and the source term of GLC for the 3D domain, projected into the x-y axes. (b) The plot shows the average concentrations of each species computed in the three-dimensional example (blue line) compared with the one obtained in Figure 3.6b with CutFEM in the circle.

Based on the converged mesh sizes obtained for the two-dimensional examples, we set the mesh size to $h = 0.3772$. Note that the choice of the Gaussian parameters σ is designed to make the reactions significant since the mesh is coarser than the meshes used in the previous examples. Also, we increase the number of time steps to 100, while the final time is 10. The CutFEM penalty parameter is 0.1.

In Figure 3.11b, we plot the average concentration of each species using Equation (3.18). We examine the trend of the average concentrations plotting them with the ones computed in Section 3.5.2. Even though the system solved one in 2D and one in 3D gives different results, we expect their average concentrations to behave similarly. Clearly, we have a higher influx of GLC entering the three-dimensional domain, as well as higher initial concentrations of ATP and ADP. As expected, the average concentrations are higher in the three-dimensional domain but they all follow the same trend as the two-dimensional cases.

We show the results obtained in the three-dimensional domain at time 5 in Figure 3.12. The results are in accordance with the ones showed in Section 3.5.2.

We notice that the species are diffusing inside the domain and the reactions are happening in the location we indicated with the Gaussian functions.

In conclusion, in our three-dimensional experiment we can see how the chain of chemical reactions describe the energy metabolism of a cell in a complex structure. CutFEM is able to work with complex three-dimensional geometries, although the computational time is large (is three days in this case).

3.6 Discussion

Studying brain energy metabolism can be helpful to further our understanding of several neurodegenerative diseases such as Alzheimer's and Parkinson's but a mechanistic perspective is still lacking. To investigate energy metabolism in biological relevant morphologies, we presented a simplified model of metabolism in a single cell using reaction-diffusion equations and demonstrated how to discretize the model using the FEM and CutFEM numerical methods. CutFEM has the advantage of enabling the use of a single level set function per cell, independent of the complexity of the cell geometry. Implementing using FEniCS and libCutFEM ensures the usability by non-experts. In particular, modifying one or several of the reaction diffusion equations can be made by altering only a few lines of code and any linearisation and parallelisation is done automatically by the FEniCS framework. One of the difficulties of non-conforming methods for implicit domain definition ([157], [158], [152]) is due to the ill-conditioning of the system matrices when the interfaces or the boundary of the domain passes close to a node, leading to very large or very small diagonal terms. The consistent stabilisation term used by CutFEM prevents this issue and leads to a stable and convergent scheme. Other approaches are provided in [5, 4, 3].

Our results indicate that CutFEM is a valuable approach to deal with biological problems with arbitrarily complex cell morphologies. The appeal of level set descriptions coupled to enriched finite element approaches such as CutFEM lies in the fact that the motion of geometries over time only requires updating the level set function, without modifying the mesh. This will be instrumental to consider complex and time dependent shapes of cells such as astrocytes.

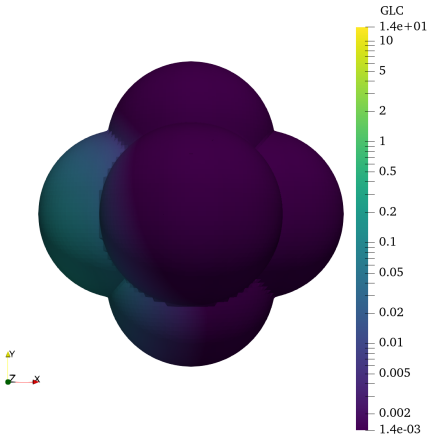

(a) GLC

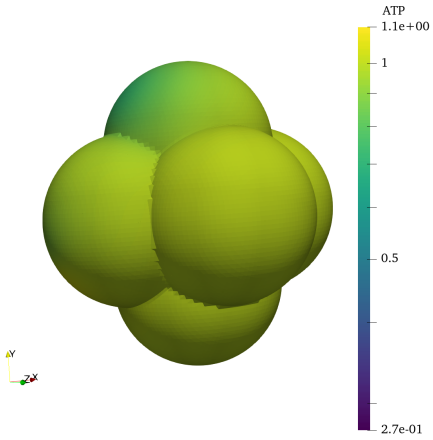

(b) ATP

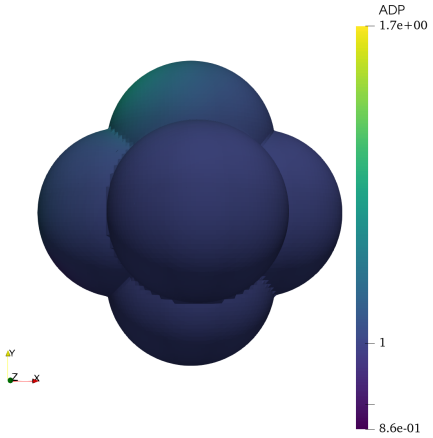

(c) ADP

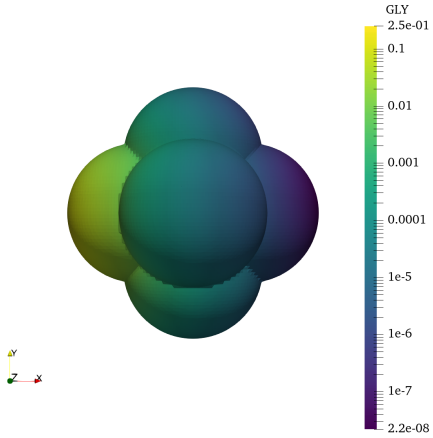

(d) GLY

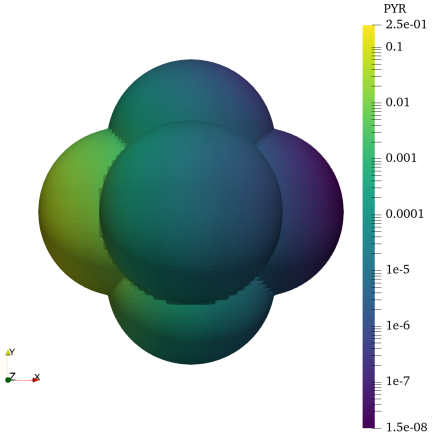

(e) PYR

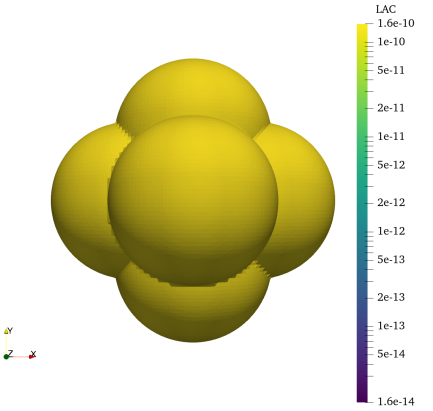

(f) LAC

Fig. 3.12 Solution of the reaction-diffusion system at time $t = 5$ solved using CutFEM inside a 3 dimensional pop corn shape. From top to bottom from left to right [GLC], [ATP], [ADP], [GLY], [PYR], [LAC]. The GLC is diffusing into the domain starting from the influx location. ATP and ADP are consumed and produced by the reaction act. GLY is produced by HXK and PYR produced by PYRK.

Our next steps will be to initiate the geometry of the cells through microscopy images 3.1 and to investigate the effect of perturbed astrocytic metabolism on neuronal support, which could lead to a better understanding of mechanisms in neurodegeneration.

CHAPTER 4

Mechanistic Multiscale Metabolic Model in Human Astrocyte

Our previous work, presented in Chapter 3, established CutFEM as a valid numerical approach to defining complex morphologies as the domain for numerical simulations. In this chapter, based on our manuscript [99] currently under review, we extended the investigation of metabolic modelling to the spatial and geometrical dimensions compared to the literature (section 2.2.1). We investigated the impact of reaction sites' spatial orchestration and geometries on our previously proposed metabolic model, where parameters for astrocytes are calibrated based on literature. First, we studied how different metabolic arrangements impact the metabolic system in simple two-dimensional geometries. Then, we explored Alzheimer's Disease metabolic conditions in human astrocytic three-dimensional images taken from confocal microscopy. My contributions to this manuscript, where I am the first author, consisted of developing the model and the software, performing the formal analysis, investigating the results, preparing the images, and writing the manuscript.

Abstract

Astrocytes with their specialized morphology are essential for brain homeostasis as metabolic mediators between blood vessels and neurons. In neurodegenerative diseases such as Alzheimer's disease (AD), astrocytes adopt reactive profiles with molecular and morphological changes that could lead to the impairment of their metabolic support and impact disease progression. However, the underlying mechanisms how metabolic function of human astrocytes is impaired by their morphological changes in AD is still elusive. To address this challenge, we developed and applied a metabolic multiscale modelling approach integrating the dynamics of metabolic energy pathways and physiological astrocyte morphologies acquired in human AD and age-matched control brain samples. The results demonstrate that the complex cell shape and intracellular organization of energetic pathways determine the metabolic profile and support capacity of astrocytes in health and AD conditions. Thus, our mechanistic approach indicates the importance of spatial orchestration in metabolism and allows for the identification of protective mechanisms against disease-associated metabolic impairments.

4.1 Introduction

The human brain is the organ with the highest energy demands required to sustain the high activity of neurons [132]. Astrocytes are multitasking glial cells directly contributing to brain homeostasis and metabolism. By their complex architecture as star-like branched cells, they are intermediate structures sitting between neurons and their synapses, which they enwrap with their intricate processes, and the blood vessels, which they engulf with their endfeet. Based on this strategic positioning, astrocytes act as metabolic supporters providing energy in the form of lactate (LAC) to neurons and modulating their activity [175, 24]. Astrocytes are also known to respond to brain "insults" and drastically change in many brain diseases such as Alzheimer's disease (AD). In these situations, they engage reactive profiles with changes in morphology and in their molecular program [94, 42] like in AD where human astrocytes exhibit hypertrophy and overbranching [174, 43]. In addition to morphological changes, AD-associated astrocytes also exhibit metabolic

dysfunctions [33, 62, 13, 74, 238], altering their role as neuronal supporters, but the relation to morphology is not established.

The metabolic support function of astrocytes depends on sufficient LAC production and efficient LAC export at the perisynapses as energy substrate for neurons [203], and on sufficient availability of adenosine triphosphate (ATP) for its own metabolic sustainability [218] requiring an ATP : ADP ratio at least larger than one [8]. Furthermore, physiological conditions for functional astrocytes are characterized by an approximate 10:1 ratio between LAC and pyruvate (PYR), the substrate for lactate production and mitochondrial activity, further indicating their metabolic support function [142]. Hence, astrocytes have to keep a balance between a LAC based "altruistic" support mode and a more "egocentric" self-sustainability characterized by a high ATP : ADP ratio. The mechanistic relation between the observed disease-related modifications in morphology and metabolic dysfunctions are still to be characterized and whether morphology changes might represent a compensatory mechanism remains elusive.

Here, we develop a general interdisciplinary approach to systematically investigate the interplay between astrocytic morphology and energy metabolism in AD by a novel spatiotemporal *in silico* model that allows for physiologically realistic simulations by integrating complex morphologies obtained by high-resolution confocal microscopy and thereby addresses the impossibility of appropriate *in vivo* human astrocyte studies. Metabolic modelling has been extensively addressed in literature at different levels *via* detailed genome-scaled metabolic network models [147] or *via* targeted dynamic models [28], including astrocytic metabolism [61, 71, 205]. All existing models neglect the spatial dimensions as they describe the metabolic processes through ordinary differential equations ($ODEs$). The underlying assumption that diffusion and reaction rates of metabolism are large enough to smear out spatial aspects are challenged by the complex morphology of astrocytes and an increasing amount of evidence for relocation of enzymes and other reaction site in different conditions [201, 119]. To include spatial variations and geometric effects, we developed a metabolic model by means of a complex reaction-diffusion system (RDS) in realistic three-dimensional (3D) morphologies obtained from high-resolution confocal microscopy images of astrocytes in *post mortem* brain samples of AD patients and age-matched control subjects [186]. The modelling framework incorpo-

rates the two essential astrocytic properties: 1) the main reactions of glucose metabolism are spatially localised to reflect the heterogeneous distribution of enzymes in the cell, and 2) the complex and context-dependent geometry of cells is directly incorporated from high-resolution microscopy. To address the resulting computational challenges in solving the corresponding partial equations of the RDS in realistic astrocytic morphologies with thin branches and regions of high curvature and kinks, we adapted our previous approach [97] utilizing the power of the cut finite element method (CutFEM) [58, 67] to disentangle the complex astrocytic geometries from the mesh generation of finite-element methods and handle complex geometries as independently of the mesh as possible.

By this approach, our model paves the way to a more physiological modelling of the effect of astrocytic morphology in AD. Our framework is general and open-source and can be used for other cell types characterized by high-resolution imaging. For model establishment, we first performed simulations in simple two-dimensional (2D) geometries and studied how metabolic dynamics are affected by the spatial arrangement of reaction sites. The findings in 2D indicated the importance of the spatial component and the diffusion limitation that arise from the competition between the corresponding reaction centers for the metabolic substrates. Furthermore, the results highlighted the fundamental role of mitochondrial organization for the metabolic output of the system. Based on these insights, we subsequently investigated spatiotemporal metabolic dynamics in real 3D human astrocytic morphologies by our multiscale modelling approach and demonstrate the potential of our framework to study metabolic dysfunction in AD-related reactive morphology of astrocytes.

4.2 Methods

To investigate the potential mechanistic link between morphology and energy metabolic activity, our model describes glucose metabolism by five main metabolic pathways (Fig. 4.1**a**). We describe glycolysis *via* two subsequent pathways where the first represents the ATP consuming and the second one the ATP producing reactions. The first pathway is catalysed by a set of enzymes (hexokinase, phosphoglucose isomerase, phosphofructose kinase and the fructose

bisphosphate aldolase), which consume glucose (GLC) and ATP to produce ADP and glyceraldehyde 3-phosphate (GLY). In the following, we describe this pathway by a coarse-grained hexokinase (HXK) activity. In the second lumped reaction, these metabolites are transformed into ATP and pyruvate (PYR) by a second set of enzymes (glyceraldehyde phosphate dehydrogenase, phosphoglycerate kinase, phosphoglycerate mutase, enolase and the pyruvate kinase), which we describe by the overall activity of the pyruvate kinase (PYRK). The generated PYR is subsequently metabolised into LAC by the lactate dehydrogenase (LDH) or used by mitochondrial metabolism to generate ATP. The mitochondrial metabolic activity of the Krebs cycle and oxidative phosphorylation is described by the coarse-grained effective reaction Mito. Finally, another effective reaction (act) accounts for various ATP-consuming processes associated to cellular activity. These metabolic pathways are put into a spatial context by distributing the corresponding reaction centers into a spatial domain.

4.2.1 Energy Metabolism Model

The core energy metabolism is broken down into the core metabolic pathways by the coarse-grained non-reversible reactions:

$$\mathrm{HXK} := \mathrm{GLC} + 2\,\mathrm{ATP} \rightarrow 2\,\mathrm{ADP} + 2\mathrm{GLY} \tag{4.1}$$

$$\mathrm{PYRK} := \mathrm{GLY} + 2\,\mathrm{ADP} \rightarrow 2\,\mathrm{ATP} + \mathrm{PYR} \tag{4.2}$$

$$\mathrm{LDH} := \mathrm{PYR} \rightarrow \mathrm{LAC} \tag{4.3}$$

$$\mathrm{Mito} := \mathrm{PYR} + 28\,\mathrm{ADP} \rightarrow 28\,\mathrm{ATP} \tag{4.4}$$

$$\mathrm{act} := \mathrm{ATP} \rightarrow \mathrm{ADP}\ , \tag{4.5}$$

where the first two reactions consider the ATP consuming and ATP producing parts of glycolysis, LDH describes the activity of lactate dehydrogenase. Mito reflects the overall metabolic activity of mitochondria in terms of ATP production and general cellular activity is reflected by the act reaction.

Reaction Diffusion System

To investigate the spatial coupling of the metabolic pathways (Eqs. (4.1)-(4.5)), the reactions were integrated by a RDS [160]. The domain of the $PDEs$ is

a bounded subset of $\mathbb{R}^d$ ($d = 2$ or 3), denoted by Ω and concentrations $[\,\cdot\,]$ are defined as function $[\,\cdot\,] : \Omega \times [0, T] \to \mathbb{R}$. Diffusion coefficients for each species are given by $D_{[\,\cdot\,]}$ and chemical reactions are modeled using mass action kinetics [226]. The reaction rate for homogeneous cellular activity (K_{act}) and a spatial reaction rate density, $\mathcal{K}_j$, for the other four reactions. Considering M reaction sites located in $\{\mathbf{x}_i\}_{i=1}^{M} \in \Omega$, the spatial reaction rates are defined as the product between the classical reaction rates, K_j, and Gaussian functions located at those reaction sites with variance $\sigma_i \in \mathbb{R}^+$:

$$\mathcal{K}_j(\mathbf{x}) = \frac{K_j}{\xi}\text{meas}(\Omega)\sum_{i=1}^{M}\mathcal{G}(\mathbf{x}_i, \sigma_i) \quad j = \{\text{HXK}, \text{PYRK}, \text{Mito}, \text{LDH}\}.$$

ξ is a parameter that ensure the property that $\int_\Omega \mathcal{K}_j \mathrm{d}x = K_j$ and meas(Ω) is the area of the domain in 2D or the volume in 3D. The source of GLC is described through a function $J_{\text{in}} : \Omega \times [0, T] \to \mathbb{R}$:

$$J_{\text{in}}(x, t) = \begin{cases} \alpha \in \mathbb{R} \quad \text{if} \quad (x, t) \in \Omega_{\text{in}} \times [0, T], \quad \text{where} \quad \Omega_{\text{in}} \subset \Omega \\ 0 \quad \text{otherwise.} \end{cases}.$$

Similarly, the degradation of LAC, which is proportional to the amount of LAC in region $\Omega_{\text{out}} \subset \Omega$ is described by function $\eta_{\text{LAC}} : \Omega \times [0, T] \to \mathbb{R}$

$$\eta_{\text{LAC}}(x, t) = \begin{cases} \eta \in \mathbb{R} \quad \text{if} \quad (x, t) \in \Omega_{\text{out}} \times [0, T], \quad \text{where} \quad \Omega_{\text{out}} \subset \Omega \\ 0 \quad \text{otherwise.} \end{cases}.$$

With this definition the reaction diffusion system is given by

$$
\begin{cases}
\frac{\partial[\mathrm{GLC}]}{\partial t} = & D_{[\mathrm{GLC}]}\nabla^2[\mathrm{GLC}] - \mathcal{K}_{\mathrm{HXK}}[\mathrm{GLC}][\mathrm{ATP}]^2 + J_{\mathrm{in}} \\
\frac{\partial[\mathrm{ATP}]}{\partial t} = & D_{[\mathrm{ATP}]}\nabla^2[\mathrm{ATP}] - 2\mathcal{K}_{\mathrm{HXK}}[\mathrm{GLC}][\mathrm{ATP}]^2 + 2\mathcal{K}_{\mathrm{PYRK}}[\mathrm{ADP}]^2[\mathrm{GLY}] \\
& +28\mathcal{K}_{\mathrm{Mito}}[\mathrm{PYR}][\mathrm{ADP}]^{28} - K_{\mathrm{act}}[\mathrm{ATP}] \\
\frac{\partial[\mathrm{ADP}]}{\partial t} = & D_{[\mathrm{ADP}]}\nabla^2[\mathrm{ADP}] + 2\mathcal{K}_{\mathrm{HXK}}[\mathrm{GLC}][\mathrm{ATP}]^2 - 2\mathcal{K}_{\mathrm{PYRK}}[\mathrm{ADP}]^2[\mathrm{GLY}] \\
& +K_{\mathrm{act}}[\mathrm{ATP}] - 28\mathcal{K}_{\mathrm{Mito}}[\mathrm{PYR}][\mathrm{ADP}]^{28} \\
\frac{\partial[\mathrm{GLY}]}{\partial t} = & D_{[\mathrm{GLY}]}\nabla^2[\mathrm{GLY}] + 2\mathcal{K}_{\mathrm{HXK}}[\mathrm{GLC}][\mathrm{ATP}]^2 - \mathcal{K}_{\mathrm{PYRK}}[\mathrm{ADP}]^2[\mathrm{GLY}] \\
\frac{\partial[\mathrm{PYR}]}{\partial t} = & D_{[\mathrm{PYR}]}\nabla^2[\mathrm{PYR}] + \mathcal{K}_{\mathrm{PYRK}}[\mathrm{ADP}]^2[\mathrm{GLY}] - \mathcal{K}_{\mathrm{LDH}}[\mathrm{PYR}] \\
& -\mathcal{K}_{\mathrm{Mito}}[\mathrm{PYR}][\mathrm{ADP}]^{28} \\
\frac{\partial[\mathrm{LAC}]}{\partial t} = & D_{[\mathrm{LAC}]}\nabla^2[\mathrm{LAC}] + \mathcal{K}_{\mathrm{LDH}}[\mathrm{PYR}] - \eta_{\mathrm{LAC}}[\mathrm{LAC}] \ ,
\end{cases}
\tag{4.6}
$$

where we considered von Neumann boundary condition to consider no-flux settings at the cell membrane. To characterize the system's behavior, we analysed the equilibrating dynamics towards the steady state from the initial conditions for ATP and ADP concentrations

$$
\begin{cases}
[\mathrm{ATP}](x, t=0) \in \mathbb{R} \quad x \in \Omega \\
[\mathrm{ADP}](x, t=0) \in \mathbb{R} \quad x \in \Omega
\end{cases}
$$

where an initial ATP concentration is required for the initial glycolysis reactions and vanishing concentrations for the other species. To ensure robust simulations, we transformed the RDS into a dimensionless system allowing for convergence over a large parameter range (Appendix B.5).

Physiological Model Parameters

The parameters used in our model are given in Table 4.1. The diffusion parameters were chosen for ATP and ADP following [198], for GLC based on [212] and for the other species based on the Polson method [182, 221].

The calibration of the reaction rates has been done in accordance with the steady states of the ODE system [71] associated to Eq. (4.6). For J_{in} we used the maximum transport rate of GLC from [71]. For J_{out} we used the maximum transport rate of LAC but divided it for the steady state, since we required our

transport of LAC to be proportional to the local concentration of LAC inside the cell.

Model parameters				
Parameter name	Value	Description	Units	Reference
D_{GLC}	$0.6E3$	diffusion coefficient of glucose	$[\mu\mathrm{m}^2\mathrm{s}^{-1}]$	[212]
D_{ATP}	$0.15E3$	diffusion coefficient of ATP	$[\mu\mathrm{m}^2\mathrm{s}^{-1}]$	[198]
D_{ADP}	$0.15E3$	diffusion coefficient of ADP	$[\mu\mathrm{m}^2\mathrm{s}^{-1}]$	[198]
D_{GLY}	$0.51E3$	diffusion coefficient of glyceraldehyde	$[\mu\mathrm{m}^2\mathrm{s}^{-1}]$	[182, 221]
D_{PYR}	$0.64E3$	diffusion coefficient of pyruvate	$[\mu\mathrm{m}^2\mathrm{s}^{-1}]$	[182, 221]
D_{LAC}	$0.64E3$	diffusion coefficient of lactate	$[\mu\mathrm{m}^2\mathrm{s}^{-1}]$	[182, 221]
$\mathrm{GLC}(t=0)$	0.0	initial concentration of glucose	[mM]	
$\mathrm{ATP}(t=0)$	1.6	initial concentration of ATP	[mM]	[71]
$\mathrm{ADP}(t=0)$	1.6	initial concentration of ADP	[mM]	
$\mathrm{GLY}(t=0)$	0.0	initial concentration of glyceraldehyde	[mM]	
$\mathrm{PYR}(t=0)$	0.0	initial concentration of pyruvate	[mM]	
$\mathrm{LAC}(t=0)$	0.0	initial concentration of lactate	[mM]	
J_{in}	0.048	influx of glucose	$[\mathrm{mM\,s}^{-1}]$	[71]
J_{out}	0.0969	degradation term of lactate	$[\mathrm{s}^{-1}]$	[71]
K_{HXK}	$6.19E-02$	reaction rate of hexokinase	$[(\mathrm{mM})^{-2}\mathrm{s}^{-1}]$	[71]
K_{PYRK}	1.92	reaction rate of pyruvate kinase	$[(\mathrm{mM})^{-2}\mathrm{s}^{-1}]$	[71]
K_{Mito}	$8.13E-02$	reaction rate of mitochondria activity	$[(\mathrm{mM})^{-28}\mathrm{s}^{-1}]$	[71]
K_{act}	$1.69E-01$	reaction rate of cellular activity	$[\mathrm{s}^{-1}]$	[71]
K_{LDH}	$7.19E-01$	reaction rate of lactate dehydrogenase	$[\mathrm{s}^{-1}]$	[71]

Table 4.1 Model parameters

4.2.2 Image Processing of Human Astrocytes

Human Brain Tissue

Post-mortem brain tissue was obtained from the Douglas-Bell Canada Brain Bank and handled according to the agreements with the Ethics Board of the Douglas-Bell Brain Bank (Douglas Mental Health University Institute, Montréal, QC, Canada) and the Ethic Panel of the University of Luxembourg (ERP 16-037 and 21-009). The two hippocampal samples used in this work were donated from a male 87-year-old Alzheimer's Disease patient with a disease stage of A2B3C2 and a post-mortem interval of 21,75 hours, and by a female 89-year-old (age-matched) control subject with a post-mortem interval of 23,58 hours.

Immunofluorescence Stainings

The PFA-fixed hippocampal samples were cryosectioned into $50 - 100\,\mu$m thick slices on a sliding freezing microtome (Leica SM2010R). To visualize astrocytes and mitochondria, we co-immunostained the slices against glial fibrillary acidic protein (GFAP) and Tu translation elongation factor mitochondrial (TUFM) respectively. The target-binding primary antibodies used here were Anti-GFAP guinea-pig (Synaptic Systems Cat# 173 004, RRID:AB_10641162) at a dilution of 1:500, and Anti-TUFM mouse (Atlas Antibodies Cat# AMAb90966, RRID:AB_2665738) at a dilution of $1 : 200$. The corresponding fluorophore-coupled secondary antibodies used were Alexa Fluor 647-AffiniPure Donkey Anti-Guinea Pig IgG (H+L) (Jackson ImmunoResearch Labs Cat# 706-605-148, RRID:AB_2340476) at a dilution of $1 : 300$ and Alexa Fluor 488-AffiniPure Donkey Anti-Mouse IgG (H+L) (Jackson ImmunoResearch Labs Cat# 715-545-150, RRID:AB_2340846) at a dilution of $1 : 400$. We followed a previously published protocol [186] with the exception of a double incubation with primary antibodies for the TUFM staining.

Image Acquisitions

High-resolution confocal images with $0.333\,\mu$m z-step were acquired using a Leica DMi8 microscope with a 93X glycerol objective and LAS X software (Leica Microsystems). The region of interest was fixed on the hippocampal subregion CA1.

Image Pre-Processing

The surface function of Imaris 9.6.0 software was used to segment GFAP staining to produce astrocyte morphology 3D reconstructions. The surface grain size parameter was set to $0.3\,\mu$m for the segmentation of astrocyte morphology. Upon segmentation of the GFAP signal of the entire image, we manually selected the astrocyte of interest and removed all other non-relevant segmentation structures. The spots function was used to segment TUFM staining. The estimated spots diameter was set to $0.2\,\mu$m. To select only the mitochondria of interest (corresponding to the astrocyte of interest) we applied

the filter of the spots function called 'Shortest Distance to Surface' [segmented astrocyte]. In the control astrocyte some mitochondria of interest were not automatically selected by this filter setting, because they were too far away from the segmented surface, however part of the astrocyte, notably in the cell soma. To include these mitochondria into the analysis, a second filter was applied twice by selecting the central mitochondria of the soma compartment and applying 'Shortest Distance to Surface' function.

The direct use of the astrocytic segmented images as domain for our simulation would require a mesh fine enough to capture the thin branches of the cellular structure. This would mean billions of quality finite elements, with a good aspect ratio. In literature, this problem was addressed by refining the mesh in critical regions [70]. However in our case, this would require refining all branches. We overcome these issues by additional image pre-processing where we dilated and down-sampled the binary images. These two steps enlarged the thin branches and avoid discontinuities when we map the images to the finite element mesh. These steps are not critically affecting the real morphology of the astrocytes and might actually address partially the GFAP staining limitation. Moreover, we impose the astrocytic volume in the simulations to be equal to the one of the segmented images obtained with Imaris. Eventually, we obtained the final segmented images (f) with labeling the voxels inside (-1), outside (1) and on the boundary (0) of the astrocytes.

Before applying the same steps to the binarised segmented mitochondrial images, we applied a convolution filter to smooth the voxels. To extrapolate the information about mitochondrial density, we selected all connected components in the images and for each of them, we identified the center and the radius of the circle that contains such component.

4.2.3 Numerical Methods

To solve numerically the RDS, the first step is to convert Eq. 4.6 into a corresponding weak form [47]. Then, we discretise the weak form both in time and space. we discretise the time derivative using a finite difference method (backward Euler) [185] and the spatial domain by finite elements [116] and cut finite elements [38]. The 2D experiments were solved using classical finite

element methods based on FEniCS [138, 9], while the 3D experiments were solved using CutFEM [58, 38]. Since the weak RDS formulation is non-linear, we linearised it and used a Newton-Raphson algorithm to iteratively solve the problem. The linear system at each time step of the Newton-Raphson algorithm was solved using standard linear solver from the *PETSc* library. For further details and numerical parameters see Appendices B.6 and B.7, respectively.

4.3 Results

4.3.1 Metabolic Dynamics and Reaction Sites Competition in 2D Domains

For model establishment and calibration, we first analyzed the effect of different spatial arrangements of reaction sites on the metabolic profile in simple 2D geometries. For this, we considered a circular domain and compared different configurations of reaction locations. The diameter of the circular domain was set to 140 μm as an average diameter that contains a full astrocyte [165]. To reflect the metabolic flux from the endfeet towards the perisynapses at the neurons' locations, we placed the entry of GLC and the exit of LAC at opposing sides of the circle (Fig. 4.1**b**) where the subregions are defined as the intersection of a circle with a radius of 10 μm and centers are located at the origin for GLC and the antipodal point for LAC .

In this simplified setup, we first assumed that a given reaction occurs around a single location with a spatial extent of a Gaussian distribution with a width of $\sigma = 20.0\,\mu$m. As a control case, all four reactions were located in the center of the circle as shown in Fig. 4.1**c**, mimicking a well-stirred condition. In a more complex enzyme arrangement, we located the four reactions on the vertices of an equilateral triangle inscribed inside the circle: one reaction is placed on the top vertex close to the LAC exit, one reaction on the bottom right vertex and two reactions are placed on the bottom left vertex. An example is shown as "Location 1" in Fig. 4.1**b**, where PYRK and LDH are placed on the top of each other, while HXK and Mito are on the top and bottom right vertex, respectively.

The resulting dynamics of the Location 1 and the control setup are shown in Fig. 4.1**d** where the average concentration dynamics inside the domain for each involved metabolite is shown. As a reference, we also plotted the steady state concentrations from Cloutier *et al.* [71], which was used to calibrate parameters of our model for which no literature information was available (see Table 4.1). As expected, the control configuration leads to steady-state concentrations in agreement with Cloutier *et al.* during an equilibrium period of $\approx$ 50s, with an exception for LAC which exhibits an almost doubled level. By contrast, the arrangement of the enzyme sites in spatially distributed configurations such as Location 1 affects the metabolite levels of interest. For example, the steady state corresponding to Location 1 is characterized by concentrations of GLC, GLY, PYR and LAC that are approximately four, ten, two and three times higher compared to the well-mixed condition described by ODEs in Cloutier *et al.*, respectively.

The steady state solutions of Location 1 indicates the necessity of the species to diffuse inside the domain and reach the corresponding enzyme sites: GLC needs to diffuse into the other part of the domain to act as substrate for HXK, and the produced GLY needs to reach the PYRK to be metabolized into PYR. The reactions are thereby diffusion-limited and the system reaches the steady state before consuming more GLY. Finally, the increased LAC level for Location 1 in relation to the control case is caused by the co-localization of PYRK and LDH where produced PYR is directly metabolized into LAC whereas in the control case Mito and PYRK compete for PYR as substrate.

Spatial arrangement of metabolism has an impact on cellular metabolite concentrations.

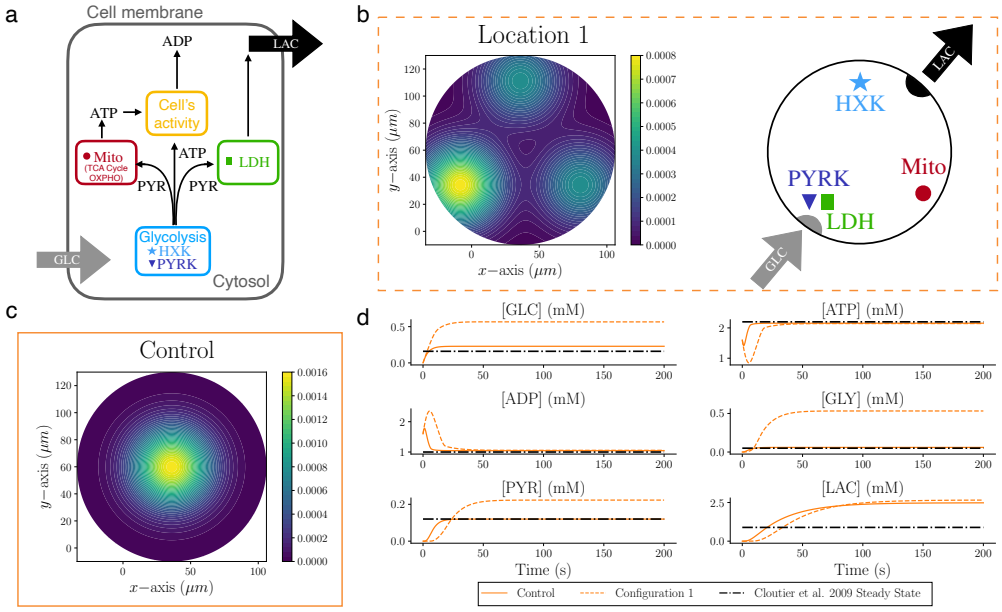

Fig. 4.1 **a** GLC enters the cytosol of the cell and takes part in glycolysis whose effective kinetics is captured by the two reactions HXK and PYRK. The products of glycolysis are subsequently consumed by the LDH reaction for generating LAC, by the act reaction describing ATP consumption due to cellular activity, and by mitochondria where the effective reaction Mito produces ATP from PYR through the Krebs cycle and oxidative phosphorylation. **b** (left) Generic configuration to investigate the effect of metabolite transport on the output of metabolism in a 2D circular domain. The color map highlights the position of the reaction sites, which are located on the vertices of an equilateral triangle. Two reaction sites are colocalised at the bottom left corner. (Right) Position of the reaction sites in Location 1: HXK on the top close to the efflux of LAC, PYRK and LDH colocalised close to the GLC influx, and Mito on the last vertex. **c** Control scenario: all reaction sites are located in the center. **d** Dynamics of the average concentration of each species in Location 1 and control cases, compared with the steady state values from Cloutier *et al.*.

To investigate systematically the effect of co-localisation and/or proximity of reaction centers to GLC influx or LAC efflux, we considered all possible location configurations for the four reactions on the vertices of the triangle (Fig. 4.1**b**). Considering the colocalisation of two reactions in the left-bottom vertex, leads to twelve possible location configurations (Figs. 4.2**a** and 4.2**c**). As a first attempt to address slightly more complex morphologies, we studied the twelve

locations within a two-dimensional star shape (Fig. 4.2**b**) as a simplified version of an astrocyte. This setup allows for comparable results between the two domains, since molecules have to pass similar distances between the subregions where GLC enters and the subregion where LAC is exported. Reaction sites were located analogously at the three vertices of an equilateral triangle within the star. As in the circular setup, we placed two reaction sites colocalised closer to the influx of GLC, and one reaction site at each of the remaining vertices.

Fig. 4.2**d** shows the steady-state and spatially averaged concentration of each species of interest for the twelve possible configurations of the circular (left columns) and the star domain (right columns) where the maximum and minimum values for each species are highlighted in red and blue, respectively. Simulations performed in both domains exhibit similar trends. The species that are affected the most by the different spatial arrangement are GLC, GLY and PYR for the co-localisation of the reaction sites HXK-PYRK (Location 6 and 9) and PYRK-LDH (Location 1 and 4) which led to low level of GLY or PYR, respectively. In the control case, where all the reaction sites overlap in the center of the domain, the system is more efficient with low levels of GLC, GLY and PYR, and a medium value of LAC. Although LAC shows differences depending on the location of the reaction sites, the changes are less significant due to the efflux which reduces LAC steady state concentrations. Interestingly, the star-shape domain exhibits the highest values of LAC pointing to the importance of morphologies with branches and higher complexity. Since cellular activity is assumed to occur homogeneously inside the domains, variability in ATP and ADP levels across the setups are rather small confirmed by the [ATP] : [ADP] ratio with a variance between all the simulations of $0.005\,(\mathrm{mM}^2)$ (Fig. 4.2**e**).

Overall, these *in silico* experiments emphasize the variable output of the metabolic RDS as a function of the intracellular spatial organization of reaction sites. To further investigate this effect, we next modelled the effect of enzyme distributions in more detail.

Spatial organization and competition between reaction sites affect the metabolic activity of the system.

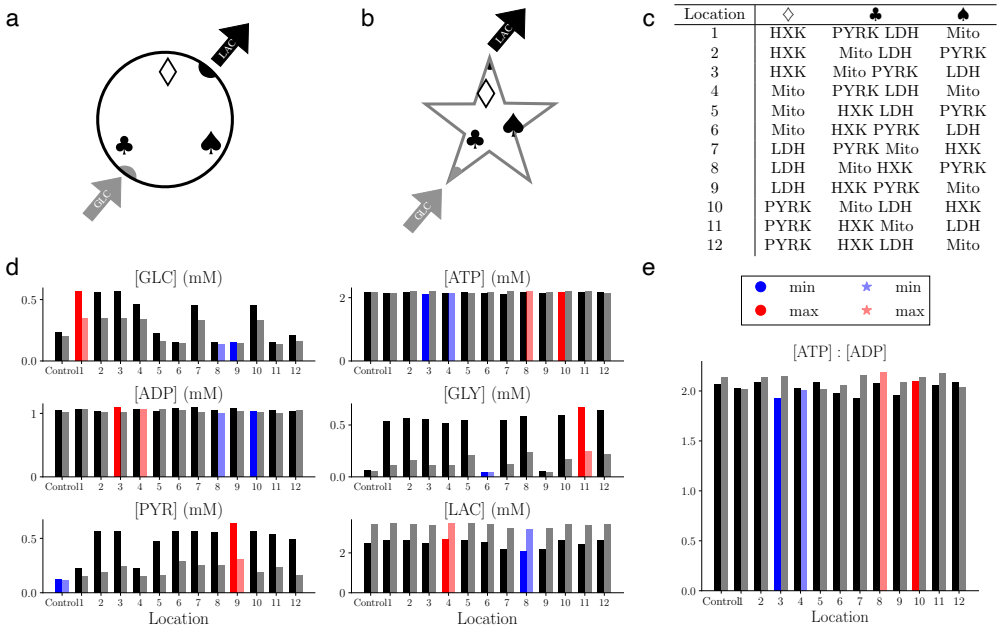

Location	♢	♣	♠
1	HXK	PYRK LDH	Mito
2	HXK	Mito LDH	PYRK
3	HXK	Mito PYRK	LDH
4	Mito	PYRK LDH	Mito
5	Mito	HXK LDH	PYRK
6	Mito	HXK PYRK	LDH
7	LDH	PYRK Mito	HXK
8	LDH	Mito HXK	PYRK
9	LDH	HXK PYRK	Mito
10	PYRK	Mito LDH	HXK
11	PYRK	HXK Mito	LDH
12	PYRK	HXK LDH	Mito

Fig. 4.2 **a** Spatial setting of simulations performed in a 2D circle. GLC enters along one side, and on the diametrically opposite side, LAC is exported. Each of the three symbols is associated to one (diamond and spade) or two (club) reactions. **b** Spatial setting of simulations performed in the star shape. The reaction sites are located analogously to the circle domain with the same distance between the GLC entry vertex and the LAC efflux/degradation. **c** Table of the 12 possible configurations corresponding to the allocation of one reaction site to diamond and spade vertices, and two colocalised reaction sites at the club vertex. **d** Spatially averaged steady-state concentrations of each species for the circle (left) and the star (right) **e** Spatially averaged steady state ATP : ADP ratio for simulations in a circular (left) and star-like geometry (right).

4.3.2 Uniform and Polarised Distribution of Reaction Sites in a Rectangular Domain

Based on the establishment of the spatiotemporal metabolic model for one reaction center for each pathway reaction, we next explored the effect of inhomogeneous distributions of reaction centers on the metabolic state of the cell. For this purpose, we considered for each metabolic reaction ten distinct

reaction sites with a smaller spatial extent ($\sigma = 1.0\,\mu$m), while conserving the overall metabolically activity. To mimic the morphology of astrocytic branches, the shape of the RDS domain was chosen as a two-dimensional rectangle of dimension $[0, l] \times [0, L]$, with width $l = 4\,\mu$m and a length $L = 140\,\mu$m where GLC enters from the bottom left corner of the rectangle (origin) and LAC exits from the top right corner. We considered two types of cellular organisation: one where the reaction sites are uniformly distributed inside the domain and the extreme opposite setting of a polarised cell where some reactions occur predominantly at one of the extremities of the cell. To ensure robustness of the findings, the two settings were compared by ensemble simulations of 200 distinct realizations of each setting. For the uniform cells, the coordinates of the 10 reaction sites of each type were randomly selected from a uniform distribution that covers the rectangular domain. Realizations of polarised cells were generated either by normal distributions ($\mathcal{N}(m, \sigma')$, where m and σ' denote the mean and standard deviation, respectively) or by log-normal ($\log\mathcal{N}(m, \sigma')$) distributions. Fig. 4.3**a** shows the position of the reaction sites along the y coordinate of the 200 realisations and Fig. 4.3**b** exemplifies enzyme distributions for a given cell for each setting. The different strategies for polarised cells lead to a certain probability for mitochondria localization in the upper part of the domain for the "Polarised" configuration but not for the "Polarised $\log\mathcal{N}(2)$" configuration (Fig. 4.3**a**). These settings allow for investigating the competition between the Mito and LDH reactions for their shared substrate PYR (Appendix B.1).

The steady-state level of metabolites is affected by the polarised distribution of enzymes within cells.

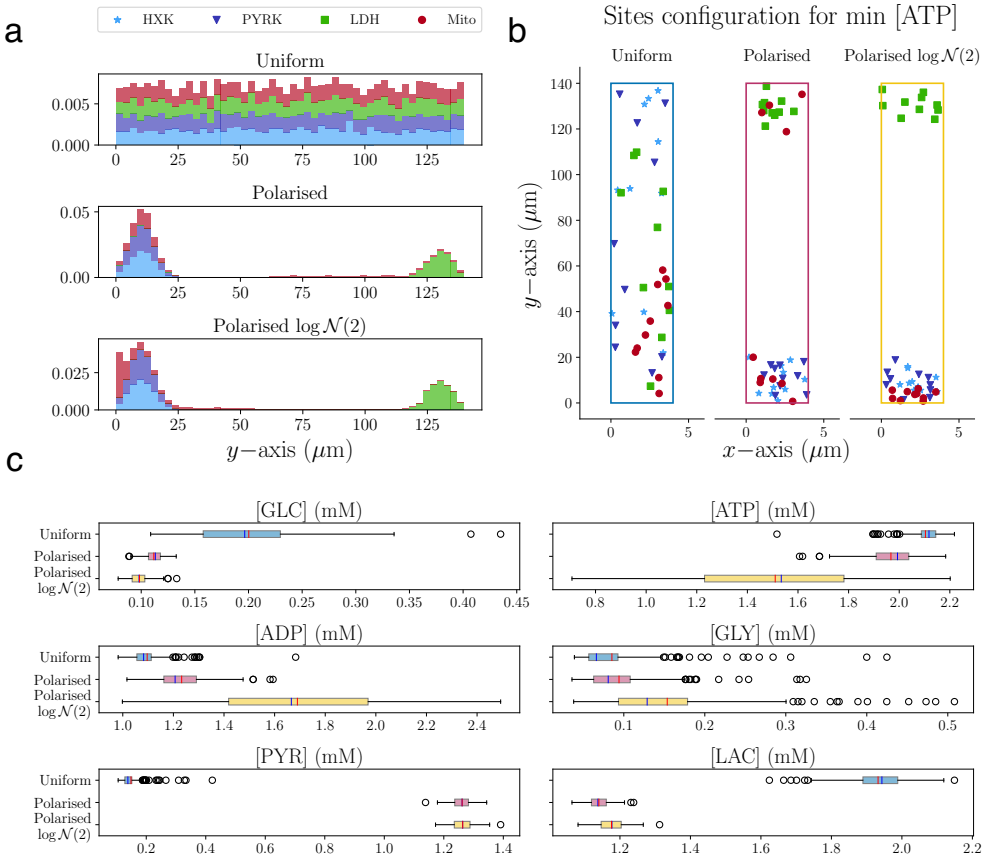

Fig. 4.3 **a** Distribution of the enzymes along the y-axis of the rectangular domain: HXK in light blue, PYRK in dark blue, LDH in green and Mito in dark red (top panel). In the Uniform setting, the reacting sites are uniformly distributed along the y-axis. In the Polarised settings, HXK, PYRK and LDH are spread unevenly over the domain with the first two located close to the origin and the latest close to the top of the domain. Mito reaction sites are distributed in the following way: 6 of them are normally distributed and colocated in the same area as HXK and PYRK, and 4 of them are uniformly located in the upper part of the domain (middle panel). In the Polarised log $\mathcal{N}(2)$ setting, mitochondria are located in the domain according to a log-normal distribution (bottom panel). **b** Examples of Uniform, Polarised and Polarised log $\mathcal{N}(2)$ distributions for the less energized cell where mitochondrial production is the most affected by polarisation. **c** Box plot of the average steady-state concentration of each species for the Uniform, Polarised and Polarised log $\mathcal{N}(2)$ distributions. (The mean and median of each box is signed in red and blue, respectively.)

Holm-Bonferroni Method							
T test independent		[GLC]	[ATP]	[ADP]	[GLY]	[PYR]	[LAC]
Uniform	Polarised	0.0	0.0	0.0	0.093	0.0	0.0
Uniform	Polarised $\log\mathcal{N}(2)$	0.0	0.0	0.0	0.0	0.0	0.0
Polarised	Polarised $\log\mathcal{N}(2)$	0.0	0.0	0.0	0.0	0.598	0.0
Wilcoxon-Mann-Whitney test		[GLC]	[ATP]	[ADP]	[GLY]	[PYR]	[LAC]
Uniform	Polarised	0.0	0.0	0.0	0.0001	0.0	0.0
Uniform	Polarised $\log\mathcal{N}(2)$	0.0	0.0	0.0	0.0	0.0	0.0
Polarised	Polarised $\log\mathcal{N}(2)$	0.0	0.0	0.0	0.0	0.345	0.0

Table 4.2 $p-$values of the significance tests for Experiment 2. We used multiple comparison Holm-Bonferroni Method on a parametric independent T-test and a non-parametric Wilcoxon-Mann-Whitney test with significance threshold of $p-$value < 0.05.

To assess the effect of the different spatial arrangements, the steady state concentration of the 200 realizations, for the three different configurations, were compared statistically (Fig. 4.3**c**) including T-test and Wilcoxon-Mann-Whitney with Holm-Bonferroni compensation (Table 4.2 and Appendix B.2). In general, the polarised cells consume more GLC than the uniform distributed ones, which is consistent with the fact that the reaction HXK is closer to the influx. GLY is present at a very low level for all configurations as also shown in the significance test. Interestingly, PYR and LAC differ strongly in polarised cells compared to the uniform setting with a higher level in PYR caused by faster metabolizing of GLC by the HXK and subsequent PYRK reactions. On the other hand, LAC levels are higher for the uniform cells since in polarised cells PYR reaches the more distant LDH reaction only by the amount which has not been consumed by the closer located Mito reactions. The resulting LAC : PYR concentration ratio for the cells with uniformly distributed enzymes cells respect the physiological constraints, whereas polarised cells exhibit ratios below one indicating an unphysiological or diseased state.

The corresponding ATP and ADP concentrations show a rather low variability for the uniform configuration with higher ATP and lower ADP concentrations (Fig. 4.3**c**) compared to the polarised cells. Interestingly, the Polarised $\log\mathcal{N}(2)$ configuration exhibits a very wide range for both concentrations with significantly different average values also in comparison with the Polarised configuration indicating the importance of mitochondrial distribution. Thus, the ATP : ADP ratio for the three cellular configurations (Fig. 4.4**a**) confirms

that the Polarised $\log\mathcal{N}(2)$ realisations cover an ATP : ADP ratio range from unhealthy (ratio < 1) to healthy (ratio ≥ 1).

The impact of the configurations on the metabolic activity and in particular with a focus on the "altruistic" behaviour producing more LAC or an "egocentric" strategy producing more ATP, can be visualized by the relationship between LAC and the ATP : ADP ratio (Fig. 4.4**b**). We found two distinct clusters formed by uniform and polarised cells, where the uniform cells display a co-existing egoistic and altruistic mode characterized by high ATP and LAC concentrations for self-sustainability and neuronal support. Indeed, the correlation between the variables, the ratio and LAC, is only slightly negative for the uniform cells (-0.19), whereas the group of polarised cells exhibits stronger negative correlation (-0.65) indicating that high values of one quantity lead to low values of the other. "Polarised" cells are located on the top of the cluster and the "Polarised $\log\mathcal{N}(2)$" cells are predominantly in the lower part of the cluster characterized by a lower ATP : ADP-ratio and slightly higher LAC concentrations (Fig. 4.4**b**). This difference indicates the importance of mitochondria localization as shown by the color-indicated classification of the vertical arrangement of mitochondria. We colored the metabolic profile of each realisation based on the highest $y-$coordinate of Mito sites ($y_{\max}$): yellow, orange, red or black, if $y_{\max} < 30$, $30 < y_{\max} < 60$, $60 < y_{\max} < 100$ or $y_{\max} > 100$, respectively. This analysis highlights that the lowest level of ATP coincides with realisations where all mitochondria are grouped in the lower region. By contrast, simulations with a high energetic profile correspond to arrangements where mitochondria are distributed throughout the whole rectangular shape. The spatial arrangements and the corresponding mitochondrial activation that describe the most energized cell for each configuration are shown in Figs. 4.4**c-d** and confirm the necessity of mitochondria to be well-distributed in the whole domain to sustain high ATP levels. Comparing the mitochondrial activity at steady state for each of these cells, we notice low activity in the lower part of the polarised cells indicating the co-localization of Mito and PYRK leads to substrate competition. This suggests that PYRK inhibits the mitochondrial activity. On the other hand, the cellular arrangements presented in Fig. 4.3**b** produce the less energised cells with minimum ATP and all mitochondria gathered in clusters.

Mitochondrial distribution determine [ATP] : [ADP] ratio and thereby energetic states of cells.

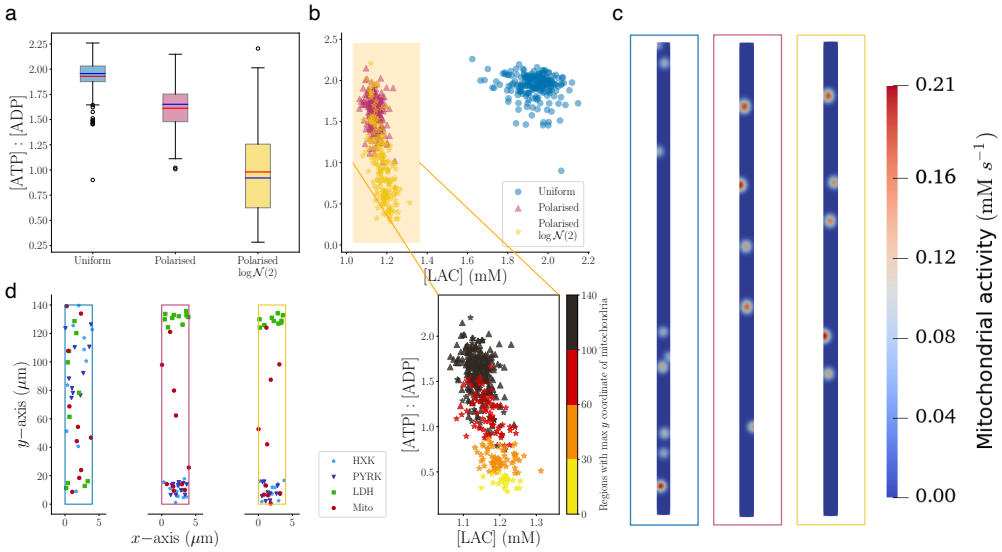

Fig. 4.4 **a** Box plot of the final average values of the [ATP] : [ADP] for Uniform, Polarised and Polarised log$\mathcal{N}(2)$ (Mean in red and median in blue). **b** (top) scatter plot of ratio against LAC final average values. There are two distinct clusters between the Polarised cells and the uniformly distributed ones. (bottom) Zoom on the ratio against LAC for Polarised cells colored based on the region where we can find the mitochondria with the highest y-coordinate. Interestingly if the enzymes are well distributed inside the domain, so if there is at least one mitochondria with a y-coordinate larger than 100 (black), the ratio value is higher. On the other hand, if the mitochondria are all located within the first or second region (yellow and orange), with y-coordinate lower than 60, the cell is in unhealthy status. **c** Mitochondria activation of the configurations with maximum ATP production for the three type of cells at steady state **d** Reaction sites setting for the maximum level of ATP for the three distributions.

Overall, this analysis demonstrates the impact of the interplay between spatial enzyme orchestration and morphology on the metabolic profile of cells. Our finding highlights that different cellular organization leads to different steady state concentrations which might be linked to potential disease of cells.

4.3.3 Morphological effects on Metabolic Activity of Human Astrocytes in Health and AD

Finally, we extend our work to 3D reconstructions of human astrocytes acquired from GFAP-immunostained *post-mortem* brain samples from age-matched control subjects (Figs.4.5**a-c**) and AD patients (Figs.4.5**d-f**). The 3D confocal images of the astrocytes were acquired in the CA1 subregion of the hippocampus (Figs. 4.5**a** and 4.5**d**). Given the typical *post-mortem* nature of such brain samples, the dynamical consequences of the morphology for metabolic profiles can be only assessed by an appropriate *in silico* strategy. The respective segmentations of the prototypical astrocytes (Figs. 4.5**b** and 4.5**e**) reveal significant differences in the volume and morphological diversity of the two cells: the reactive AD astrocyte exhibits hypertrophy, proliferation of branches and coverage of wider spatial domains in comparison with the less complex shape of the control astrocyte (Figs. 4.5**g** and 4.5**h**). Based on mitochondria staining and segmentation (Figs. 4.5**a-b** and 4.5**d-e**), a realistic spatial arrangement of mitochondria is implemented in the multiscale model (Figs. 4.5**c** and 4.5**f**). The presence of regions with different mitochondrial density is respected by tuning the center positions and variances of the Mito spatial reaction rates (Figs. 4.5**c** and 4.5**f**). The minimum variance is set to $1.0\,\mu$m and we scale accordingly the size of the other regions with a maximum of $2.0\,\mu$m. The number of reaction sites for the other reactions is set according to the amount of mitochondria selected from post-processing, 97 for the control and 140 for the reactive astrocyte (Fig. 4.5**i**). For each Mito reaction site, we located a HXK site close by in agreement with the observed relationships between these two enzymes [121, 140]. The reaction sites of PYRK and LDH are taken from a uniform distribution defined in the three dimensional box containing the astrocyte. The locations of the reaction sites for the simulations inside the

control and AD reactive astrocyte are shown in Figs. 4.6**a** and 4.6**c** together with the assumed endfeet for GLC influx and the subregions at the perisynapses for LAC export into the extracellular space (Figs. 4.6**a-c**).

Human hippocampal astrocytes from an age-matched control subject and AD patient: from microscopy image to 3D simulation setting.

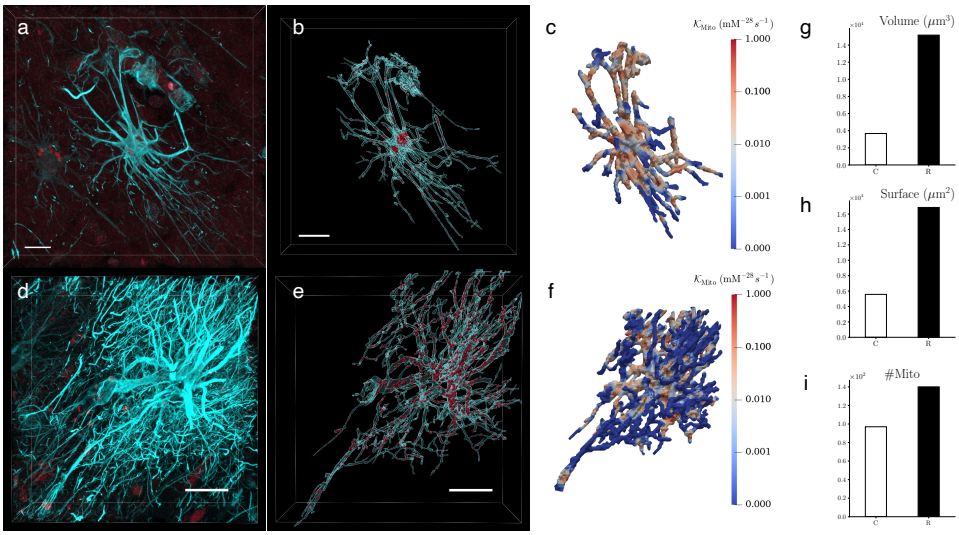

Fig. 4.5 High-resolution confocal microscopy images **a** from an age-matched control subject and **d** from an AD patient were obtained from $50-100\,\mu$m brain sections that were immunostained against GFAP (cyan) to visualize astrocyte cytoskeletal morphology, and against TUFM (dark red) to reveal mitochondria in the hippocampus. Using Imaris 9.6.0 **b** and **e**, astrocyte 3D morphology was segmented using the surface tool and mitochondria were labelled with the spots tool for the astrocytes in both conditions. Finally, based on the segmentation, we created the domains for our simulations and we selected the locations with higher density to define the Mito reactions. **c** and **f** show the spatial reaction rates $\mathcal{K}_{\text{Mito}}$ describing the mitochondria activity inside the cells. In the bar charts **g-i**, we compared the cell volumes – $3673\,\mu\text{m}^3$ for the control astrocyte (C) and $15161\,\mu\text{m}^3$ for the reactive (R), cell surfaces – $5569\,\mu\text{m}^2$ for C and $16854\,\mu\text{m}^2$ for R, and the number of mitochondria activity centers – 97 for C and 140 for R computed in **c** and **f**. Scalebars: **a-b** $15\,\mu$m, **d-e** $30\,\mu$m.

As a first analysis, we ran three baseline simulations based on the physiological parameters (Table 4.1) with one simulation inside the protoplasmic

control morphology (C) (Fig. 4.6**a**), one within the same morphology but with a polarised distribution of reaction centres (P) (Fig. 4.6**b**) and one inside the reactive astrocyte (R) (Fig. 4.6**c**, more details are given in Appendix B.3). The resulting dynamics of these baseline simulations (Fig. 4.6**d**) are in good agreement with the investigation of enzyme distributions in the 2D domains where scenarios C and R resembles properties of the uniform distributed cell and P corresponds to the polarised cell (Fig. 4.3**b**). However, the average LAC concentration is higher than expected for P and lower than expected for C and R. Also the PYR concentration is closer to that of the uniform setting for the P configuration. While the concentration values of C and R are on average very close (Fig. 4.6**b**), smaller differences are visible mostly in GLC and LAC, and attributed to the effect of the morphological differences and reaction site configurations.

To investigate a reactive astrocyte subject to AD, we extended our simulations by gradually adding AD-related dysfunctions. Experiment 1 (E1) mimics a loss of GLC uptake [159] by a 30% decreased GLC influx. Experiment 2 (E2) includes the dysfunction in mitochondrial activity [136, 156, 178] inducing a lower ATP production by a reduced reaction rate for Mito ($K_{\text{Mito}}10^{-5}$). In accordance with available experimental data [33], we considered an increment of the activity of LDH by a factor of ten in Experiment 3 (E3) and an increment in the glycolysis rate in particular in the PYRK reaction, also by a factor of ten in Experiment 4 (E4). In the final experiment (EAD), all four conditions were combined to explore their possible synergistic effects.

Fig. 4.7**a** exhibits the percentage of the concentration loss at steady state for experiments E1, E2, E3, E4 and EAD compared to R. Interestingly, the 30% reduction in GLC uptake in E1 is reflected by the final steady state in GLC ($\approx$ 28.7% loss) which induced a loss of $\approx$ 35% in GLY, PYR and LAC. Dysfunctional Mito reactions lead to an increase in final GLC level and a loss in ATP and GLY whereas the level of LAC is not affected. The experimentally observed increased activity of LDH (considered in experiment E3) results mainly in faster metabolizing of PYR. On the other hand, GLY consumption is maximised by the turnover of PYRK in the E4 experiment

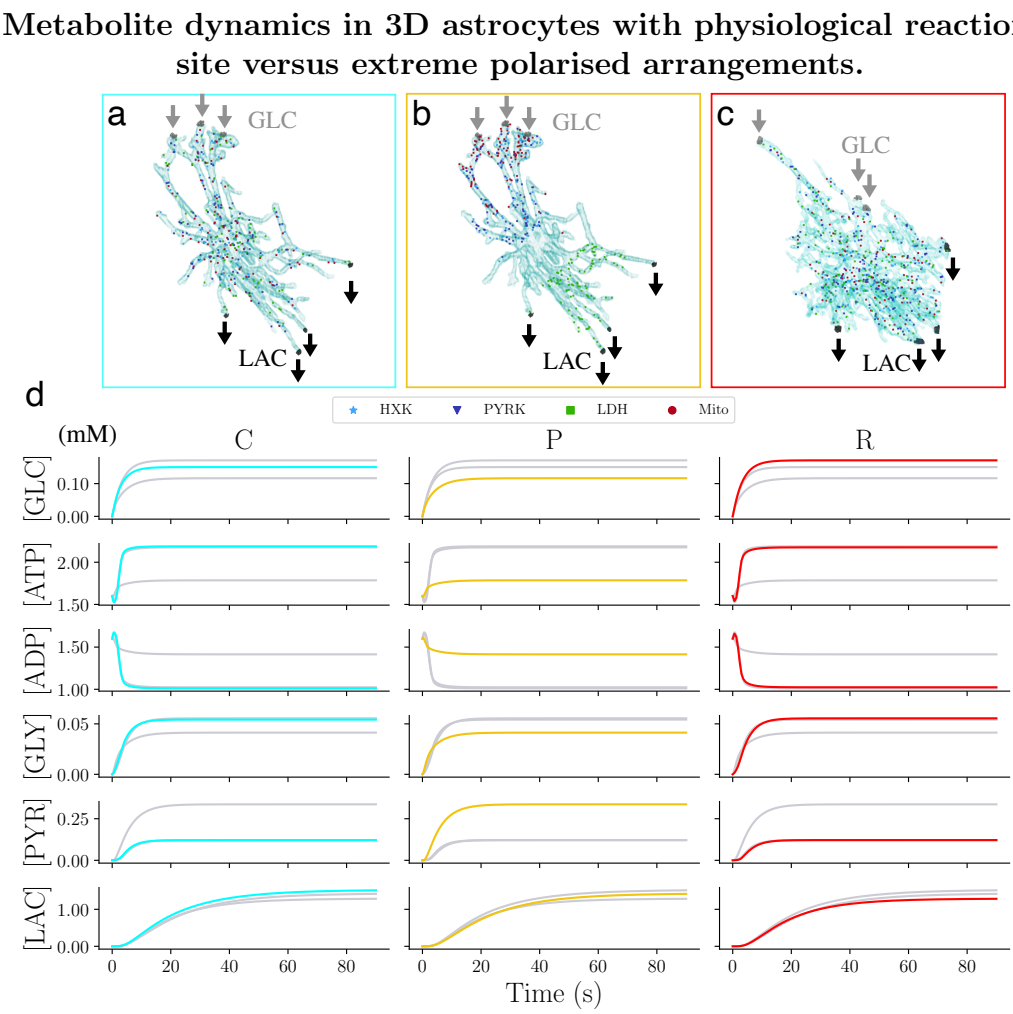

Fig. 4.6 Setting of the 3D simulations for the **a** control (C), **b** polarised (P) and **c** reactive (R) astrocyte. For C and R, Mito reaction centers were inferred from the microscopic images. Each HXK site is sorted from a gaussian distribution centered at each Mito site. In this way for each Mito we have an HXK reaction close by. PYRK and LDH are uniformly distributed inside the box that contains the cells. The reaction centers of P are sorted in the way that HXK and PYRK are colocalised close to the GLC influx, while on the other extremity of the cell we locate LDH centers. Mito centers are sorted using a log-normal distribution that locate them in the same region as HXK. The number of centers per reaction type is 90 for C and P, and 140 for R. For the three settings, GLC enters three sub-regions from the branches of the cell in contact with the blood vessels and LAC exits from four sub-regions at the other extremity of the cell. **d** Time behavior of the average concentration of each species for C (cyan), P (yellow) and R (red).

while the other concentrations are not affected. The combined effect of the individual dysfunctions in the EAD experiment leads to a significant change in the metabolic profile (with the highest loss in ATP, GLY and PYR Fig. 4.7**a**). (The dynamics of these experiments is shown in Appendix B.4.)

The functional state of cells in terms of ATP : ADP and LAC : PYR ratios at steady state is preserved for a wide range of conditions. Even for the polarised P configuration, the ATP : ADP ratio is higher than 1.0 (Figs. 4.7**b** and 4.7**c**), suggesting that a complex shape makes the cell more robust against extreme situations. This is also confirmed by the ratios of the E2 experiment, that does not exhibit a ratio below 1.0 despite mitochondrial dysfunction. The only cell that reaches a critical unhealthy state is the EAD condition (0.93), where mitochondrial dysfunction adds to the other dysfunctions. Also the ratio of LAC : PYR is always within physiological range (> 10) for all conditions except P. However, a LAC : PYR ratio of above 80 are reported in E3 and EAD, which may indicate hypoxia with low levels of oxygen in blood [142].

Since LAC export into the extracellular space is an essential mechanism of astrocytic support to neurons, we also quantified LAC efflux exporting LAC from the corresponding subregions (Fig. 4.7**d**). The asymptotic behaviour of the efflux indicates that cells with the C and P configuration export more LAC, suggesting that the less ramified morphology of the protoplasmic astrocyte allows for faster diffusion of molecules and subsequent export regions. On the other hand, E1 and EAD configurations export less, indicating that the 70% decrease in GLC uptake might drive this AD symptom. The different metabolic states of the cell are also assembled in the "altruistic" vs "egocentric" map in terms of the LAC concentration and the ATP : ADP ratio (Fig. 4.7**e**). This map indicates the C configuration as the most efficient cell with high levels for both in agreement with the previous finding on uniform distributed cells. The P setup exhibits a more altruistic behaviour than expected by producing more LAC than ATP, potentially facilitated by the morphology. When cells lack GLC, they become more egoistic and produce more ATP. Remarkably, the steady state of LAC of the R, E2, E3 and E4 experiments is $\approx 1.3\,\mu$M but the ATP concentration is decreasing from high levels in the R and E4 configuration

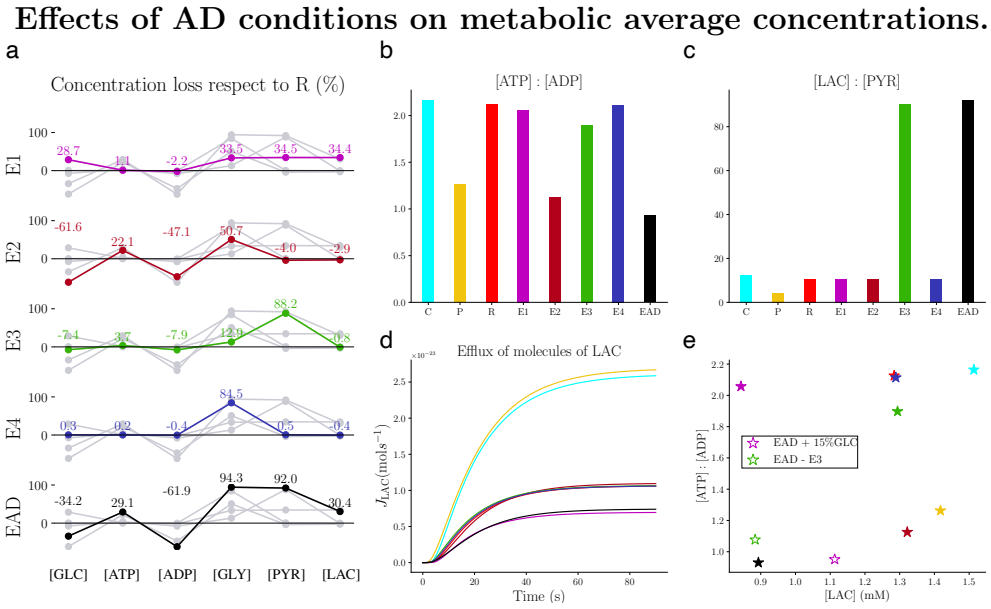

Fig. 4.7 We consider four pathological conditions of AD, in the setting of the reactive astrocyte R. E1 describes the deficiency of GLC uptake (magenta); E2, the mitochondria dysfunction (dark red); E3, the LDH overwork (green); E4, PYRK overwork (blue) and EAD, the four conditions combined (black). **a** Final average concentration loss respect to R. The experiments reflect their loss/gain imposed to the cell through the conditions. Steady-state spatially averaged **b** ATP : ADP ratio and **c** LAC : PYR ratio of control (cyan), polarised (yellow), reactive (red) and all the AD experiments. **d** Efflux of LAC molecules exported over time from the astrocyte to the extracellular space. The experiments with higher export are the two control astrocyte with C and P configurations. The experiments with a lower export are E1 with a loss in GLC uptake and EAD with the combination of the AD conditions. **e** Scatter plot of ATP : ADP against LAC final average values. The most efficient cell is the control one. Then, the different AD conditions affect the cell status leading the reactive cell affected by all the AD conditions to an unhealthy state. In order to save the EAD cell, we increase the uptake of GLC up to 85% (white star with magenta edge), and the cell responds by using the more available fuel to produce more LAC. However, blocking the LDH overwork (white star with green edge) increases ATP : ADP and thereby rescues the astrocyte from the AD conditions.

to lower concentration in E2. Finally, lower levels of both ATP and LAC is the AD-related EAD condition suggesting that it can neither support neurons nor itself. Last, we studied how to support an AD-impacted astrocyte where the results of the individual conditions helped to disentangle the different effects. Importing more GLC (by increasing the uptake to 85% of the healthy control condition) turns the cell into a more altruistic state by using the additional fuel predominantly for LAC production. Blocking the excessive activity of LDH saves the cell from AD-related energy deprivation but with the cost of reduced LAC export.

To investigate the impact of diffusion limitation as an underlying mechanism in reactive astrocytes, Fig. 4.8 illustrates the time evolution of the 3D distribution of concentrations for the healthy C and AD-related EAD condition considering the properties and spatial distribution of reaction sites (Supplementary Movies 1-12). In particular, the trapping effect discussed above is highlighted in the reactive astrocytic morphology for ATP and PYR where branches exhibit a higher concentration variability.

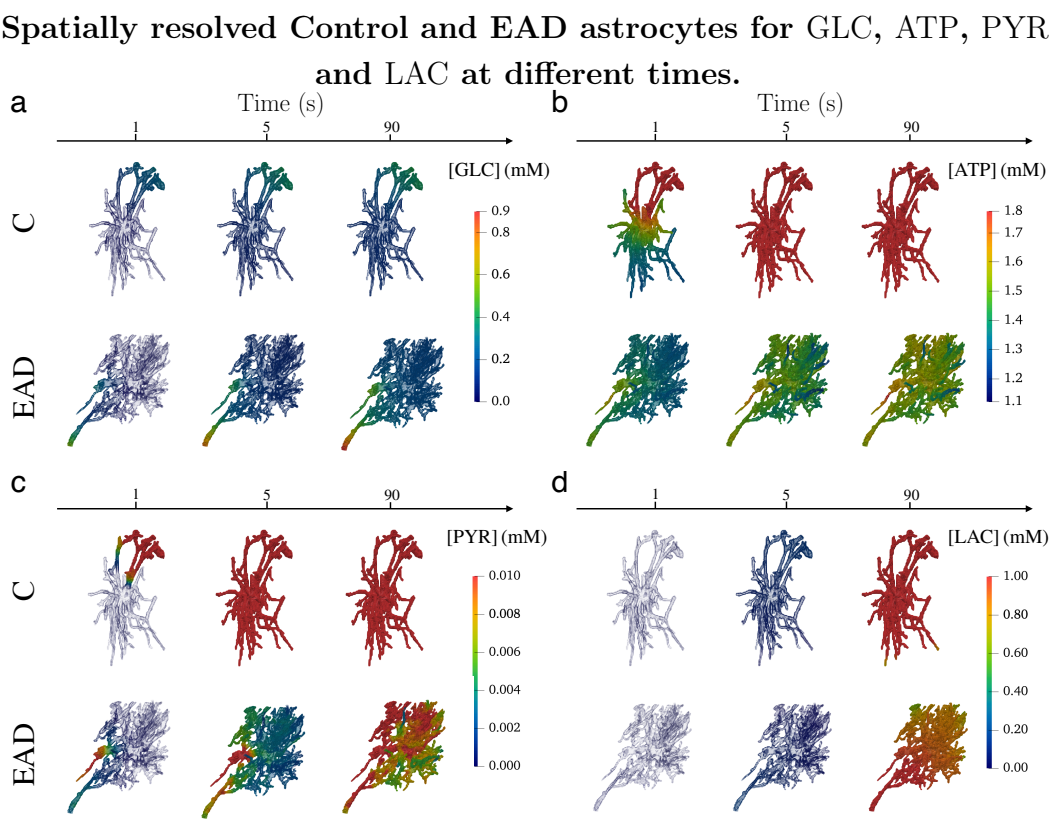

Fig. 4.8 3D spatial concentration of metabolites at three different time steps in control (C) and reactive astrocyte affected by AD pathology (EAD). **a** GLC enters from the blood vessels and spreads inside the astrocytic domains activating the glucose metabolism. **b** ATP, already present in the cells at the initial time, is produced and consumed. In particular, in correspondence with regions with high numbers/absence of Mito sites, we can notice high/low levels of ATP in EAD. **c** PYR produced by PYRK diffuses inside the 3D domains and highlight the complex shape of the reactive astrocyte with high variability of concentration within the cell. **d** LAC shows a slow production, in fact at time 5, both C and EAD show low concentrations. At the final time, we can appreciate the steady state level of LAC where the regions where it is exported are highlighted by lower concentrations.

To summarise, the physiologically realistic simulations reproduce important features of astrocytes in healthy and diseased conditions. The incorporation of real morphologies highlights cellular robustness against extreme enzymatic configurations. This is also seen for AD conditions, indicating the influence of the cellular domain on the metabolic state of the cell. In fact, a single

AD characteristic does not lead to an unhealthy cell, only combinations of AD-terrain leads to severe metabolic dysfunctions.

4.4 Discussion

Although the link between cellular morphology and metabolic activity might have implications for neurodegeneration including Parkinson's disease and Alzheimer's disease, our understanding of this connection remain imperfect due in part to experimental limitations. To address this challenge, we developed a multiscale model for energy metabolism in complex cellular domains with a specific focus on the intracellular spatial orchestration of astrocytes. To build the mathematical model, we first considered a single reaction site for each metabolic subpathway in a 2D circular geometry and validated the model in terms of physiological concentration ranges for astrocytes (Fig. 4.1), in accordance with previous ODEs model [71]. We showed numerically that different spatial organisation of reaction sites lead to distinct metabolic profiles due to diffusion limitation and local substrate competition (Fig. 4.2). The observed differences between the circular and the star-shaped domain indicated a possible trapping effect for molecules in more complex shapes. These trapping effects might be overestimated compared to a more physiologically realistic astrocyte, since many more reaction sites are typically present within an astrocytic branch. Nevertheless, these results strongly indicate that the spatial dimension and the domain complexity can have a crucial effect on metabolic profiles and may be of particular importance for the metabolic support function of astrocytes.

To further characterize these spatial effects in a more physiological setting, we considered a larger number of reaction sites, which were distributed either within a uniform or polarised arrangement inside a rectangular shape, mimicking an astrocytic branch. For each configuration, we ran 200 realisations, allowing for robust statistical comparisons between the different settings (Fig. 4.3). The results showed that cells with uniformly distributed reaction sites are significantly more efficient in both the "altruistic" LAC production as well as the "egocentric" intracellular energy state. Although polarised organization corresponds to an extreme and rare biological setting, the analysis of these

realisations indicates the importance of a more homogeneous mitochondria distribution for a sufficient activity and a related energized cell state (Fig. 4.4). This is in line with experimental observation of mitochondrial organisation and homeostasis including fission and fusion where impairment of these processes are linked to neurodegeneration [137].

Based on the 2D model, we extended our investigations to physiological 3D morphologies of astrocytes, obtained from confocal microscopy images of human *post-mortem* brain samples of an AD patient and a healthy control subject. Our approach is thereby able to integrate directly the spatial orchestration of reaction enzymes as demonstrated by the experimentally quantified mitochondrial distribution (Fig. 4.5). We first confirmed that using different morphologies but the same parameters lead to concentrations in the physiological range in agreement with the findings in the simplified 2D geometries (Fig. 4.6). To investigate the effect of AD-related molecular modifications, we analysed a reactive astrocyte with baseline parameters and four individual metabolic dysfunctions linked to AD and their combinations (Fig. 4.7). The results highlighted that different pathological effects arouse specific system response and differentiated the cell behaviour between an "altruistic" and an "egocentric" mode. Furthermore, the results indicated that any give dysfunction does not lead necessarily to a dysfunctional cell with a low ATP : ADP ratio but it is the cumulative metabolic insufficiencies that lead the cell into a critical state. This synergistic phenotype might be related to the multi-hit perspective in neurodegeneration which addresses the transient compensation and typical disease onset at higher age [173, 236]. The systematic study of the individual dysfunctions allowed to suggest that reducing LDH activity could sustain astrocytic function. Such approaches are also discussed in the context of cancer [126, 107]. However, in the context of AD, the challenge would be to interfere with metabolism in a cell-type specific manner.

Furthermore, the comparison between the simplified 2D domains and the complex 3D morphologies indicates that real astrocytic shape affect the cell state with robustness towards enzyme orchestration and different metabolic dysfunctions. This robustness might be caused by the trapping of molecules in thin branches as further indicated by the analysis of 2D star-shaped morphology. The thin processes may hamper the diffusion of molecules as shown by the spatial concentration profiles (Fig. 4.8) which increased mitochondrial activity

and corresponding ATP production with the cost of decreased LAC export. Thus, the complex morphology might provide a mechanism to support an "egocentric" state if the system reaches limiting conditions, similar to energy buffering in complex mitochondrial morphologies [105].

To our knowledge, our approach is the first 3D model of cellular energy metabolism using physiological human cellular morphologies. Our analyses of hippocampal control and AD-related reactive astrocytes clearly demonstrate the importance of morphology for cellular metabolic activity. Our approach has limitations, such as the lack of cellular compartmentalisation, the coarse-graining of enzymatic reaction into effective metabolic pathways, the limitation of the GFAP staining and the incomplete information on reaction site localization provided by imaging modalities. Despite these limitations, we demonstrate the general importance and feasibility of physiological simulations by integrating molecular properties, spatial intracellular orchestration and morphology. Based on our multiscale framework, future investigations will allow to disentangle different mechanisms underlying neurodegeneration, including mitochondrial morphology [207, 105], organization and dysfunction [122, 211, 80] by more detailed models.

CHAPTER 5

Cross-talk between Metabolism and Calcium Signalling

The fundamental role of calcium was introduced in Section 2.1.4 and the state-of-the-art modelling was presented in Section 2.2.2. In the sight of our studies on the importance of metabolic spatial organisation and the relevance of cellular geometries presented in Chapter 4, we focus our research in this chapter on the spatio-temporal crosstalk between metabolism and calcium signalling. We adapt our previously proposed metabolic model to communicate with a calcium signalling module that focuses on mitochondrial dynamics proposed by V. Voorsluijs *et al.* (2022) [225]. A corresponding journal submission is in preparation.

5.1 Introduction

Metabolism and calcium signalling are two fundamental processes in astrocytes. However, they are not entirely decoupled (Figure 5.1). There is an active crosstalk between Ca^{2+} and ATP. Ca^{2+} is transported inside the mitochondria

and used to activate the TCA cycle. On the other hand, ATP is consumed to transport Ca^{2+} into the ER.

In more detail, the transport of Ca^{2+} from the cytosol to the mitochondria is mediated by the mitochondrial calcium uniporter (MCU). Moreover, the sodium-calcium exchanger (NCX), an antiporter membrane, exchanges Ca^{2+} between mitochondria and cytosol using sodium ions. On the other hand, the passage of Ca^{2+} to the ER is performed by the sarco/endoplasmic reticulum Ca^{2+}-ATPase (SERCA), which comes at ATP costs.

Modelling has been a valid tool to study these processes, complementary to biological investigations. These two processes can be investigated separately. Metabolic models have been proposed for a single astrocyte or neuron-astrocyte, and a geometric-based model investigation was done in our previous work [99]. On the other hand, calcium signalling models have been widely investigated. The investigation of models for calcium signalling in astrocytes is extensive, from deterministic to stochastic, from spatial [166, 222] to homogeneous. A model that study the interplay between these two processes was proposed by Voorsluijs *et al.* [225] based on other models presented in literature [143, 227, 31, 73]. However, in their model they did not incorporate the spatial domains, nor glycolysis, lactate dehydrogenase and pyruvate oxidation.

Therefore, we propose a computational spatio-temporal model to investigate the relationship between cytosolic calcium and ATP in relationship with the morphology of the domain. We combine our metabolic proposed model [97, 99] with the calcium model proposed in [225]. This work focuses on the crosstalk between Ca^{2+} and ATP. In particular, they propose a more detailed description of mitochondrial activity than our previous work. The combination of these two models allow (i) improve our metabolic model with a more detailed model of mitochondrial activity (ii) investigate the impact of calcium on the metabolic output and *viceversa* (iii) consider the geometrical effect and the impact of chemical diffusivity.

Our preliminary results indicate how the calcium interaction with our metabolic model benefits the cell, improving the energy level and the lactate concentration. Moreover, our studies on simple two-dimensional geometries show the geometrical effect on the system behaviour. Last, investigating glucose deficiency highlights the robustness of the system. In conclusion, these

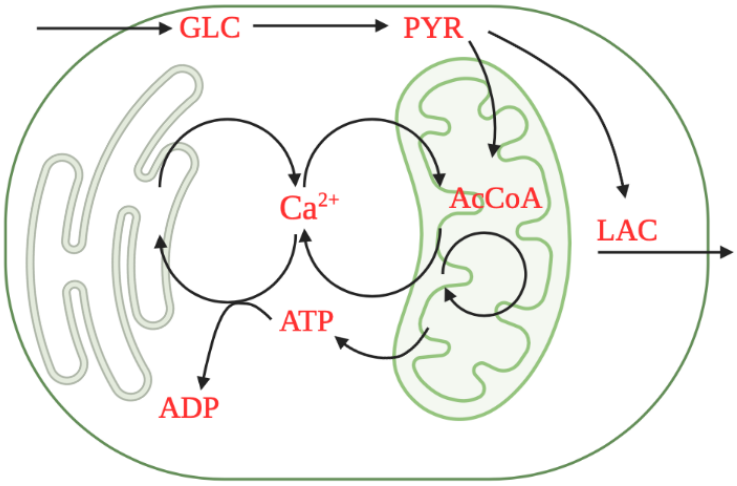

Fig. 5.1 Schematic representation of the interaction of Ca^{2+} with the metabolic process, GLC enters the cytosol and is transformed through glycolysis into PYR. PYR is either transported inside mitochondria or transformed into lactate which is then exported to the extracellular space. The pyruvate inside the mitochondria is transformed into AcCoA. TCA cycle and OXPHOS produce ATP, which is exported back to the cytosol. Cytosolic Ca^{2+} is exchanged between ER and mitochondria. To enter the ER, Ca^{2+} requires the use of ATP. (Image created with bioender.com)

preliminary results highlighted promising interactions between a calcium and metabolic model spatially-solved.

5.2 Metabolism and Calcium Model

To investigate the potential interplay between metabolism and calcium, our model proposes a coupling between two existing models. The metabolic model is taken from our previous work [99], while the calcium signalling model is based on the work [225]. The dynamic calcium model from [225] describes a detailed interaction between cytosol, ER and mitochondria, focusing on the interplay between ATP and Ca^{2+}. To refer to the cytosol, the endoplasmic reticulum and the mitochondria, we introduce the subscripts c, ER and m.

The steps of glucose metabolism are described through a combination of these two models. Glycolysis modelling is following [99], where two additional reactions describe it in a coarse-grained manner. As before (Chapter 4), we divide glycolysis into an ATP-consuming and ATP-producing reaction. The

first represents the combined action of hexokinase, phosphoglucose isomerase, phosphofructokinase and the fructose bisphosphate aldolase enzymes in the cytosol and name it HXK. The HXK reaction represents the consumption of GLC at the cost of two molecules of ATP_c to produce GLY_c and ADP_c. The second reaction (incorporating glyceraldehyde phosphate dehydrogenase, phosphoglycerate kinase, phosphoglycerate mutase, enolase and the pyruvate kinase occurring also in the cytosol) is referred to as PYRK. PYRK consumes cytosolic GLY_c and ADP_c to produce two molecule of ATP_c and PYR_c in the cytosol. Thus, glycolysis produces two molecules of ATP_c per molecule of GLC_c. The chemical equations for glycolysis are then:

$$\text{HXK}: \quad \text{GLC}_c + 2\,\text{ATP}_c \rightarrow 2\,\text{ADP}_c + 2\,\text{GLY}_c \tag{5.1}$$

$$\text{PYRK}: \quad \text{GLY}_c + 2\,\text{ADP}_c \rightarrow 2\,\text{ATP}_c + \text{PYR}_c. \tag{5.2}$$

We further consider then the transformation of cytosolic pyruvate (PYR_c) into lactate (LAC_c), performed by lactate dehydrogenase (LDH) in the cytosol:

$$\text{LDH}: \quad \text{PYR}_c \rightarrow \text{LAC}_c. \tag{5.3}$$

Part of the PYR produced by PYRK, enters the mitochondria through a pyruvate exchanger (PyrEx), which is modelled following [28]. PyrEx describes the reversible reaction where cytosolic pyruvate (PYR_c) becomes mitochondrial pyruvate (PYR_m) using hydrogen protons:

$$\text{PyrEx}: \quad \text{PYR}_c + {\text{H}_c}^+ \rightleftharpoons \text{PYR}_m + {\text{H}_m}^+ .$$

Then, the PYR_m is transformed by the pyruvate dehydrogenase complex (pdh) into acetyl co-A (AcCoA). This reaction is modelled following [28] as:

$$\text{pdh}: \quad \text{PYR}_m + \text{CoA} + \text{NAD} \rightleftharpoons \text{AcCoA} + \text{CO}_2 + \text{NADH} .$$

The AcCoA produced enters the TCA cycle. From now on, the model is taken from the work of [225]. Their model describes the TCA cycle through eight reversible chemical reactions defined as:

$$\begin{aligned}
\text{CS}: &\quad \text{OAA} + \text{AcCoA} + \text{H}_2\text{O}_\text{m} \rightleftharpoons \text{CIT} + \text{CoA} \\
\text{ACO}: &\quad \text{CIT} \rightleftharpoons \text{ISOC} \\
\text{IDH}: &\quad \text{ISOC} + \text{NAD} \rightleftharpoons \alpha\text{KG} + \text{NADH} + \text{CO}_2 \\
\text{KGDH}: &\quad \alpha\text{KG} + \text{NAD} + \text{CoA} \rightleftharpoons \text{SCoA} + \text{NADH} + \text{CO}_2 \\
\text{SL}: &\quad \text{SCoA} + \text{ADP}_\text{m} + \text{Pi}_\text{m} \rightleftharpoons \text{SUC} + \text{ATP}_\text{m} + \text{CoA} \\
\text{SDH}: &\quad \text{SUC} + \text{CoQ} \rightleftharpoons \text{FUM} + \text{CoQH}_2 \\
\text{FH}: &\quad \text{FUM} + \text{H}_2\text{O}_\text{m} \rightleftharpoons \text{MAL} \\
\text{MDH}: &\quad \text{MAL} + \text{NAD} \rightleftharpoons \text{OAA} + \text{NADH} \,.
\end{aligned}$$

The products of the TCA cycle go through the electron transport chain and oxidative phosphorylation, modelled by two reversible reactions (OX and F1) [143]:

$$\begin{aligned}
\text{OX}: &\quad \text{NADH} + 10\,\text{H}^+_\text{m} + \frac{1}{2}\text{O}_2 \rightleftharpoons \text{NAD} + 10\,\text{H}^+_\text{c} + \text{H}_2\text{O}_\text{m} \\
\text{F1}: &\quad \text{ADP}_\text{m} + \text{Pi}_\text{m} + 3\,\text{H}^+_\text{c} \rightleftharpoons \text{ATP}_\text{m} + \text{H}_2\text{O}_\text{m} + 3\,\text{H}^+_\text{m} \,.
\end{aligned}$$

Finally, the ATP_m produced in the mitochondria is exchanged with the cytosol at the cost of ADP, modelled by the ANT reversible reaction [143]:

$$\text{ANT}: \quad \text{ATP}_\text{m} + \text{ADP}_\text{c} \rightleftharpoons \text{ATP}_\text{c} + \text{ADP}_\text{m} \,.$$

Furthermore, the exchange of hydrogen protons between cytosol and mitochondria is taken into account by the reversible reaction:

$$\text{Hl}: \quad \mathrm{H_c^+} \rightleftharpoons \mathrm{H_m^+} \, .$$

The calcium dynamic of the model proposed by [225] considers the exchange of calcium between cytosol, ER and mitochondria. NCX and MCU reactions describe the exchange of Ca_c^{2+} between the cytosol and mitochondria. The exchange of Ca_c^{2+} with the ER is captured by SERCA and ER_{out}. In particular, the SERCA pump exchange of Ca^{2+} from the cytosol to ER hydrolyzes ATP_c into ADP_c. ERout mimic the flux of Ca^{2+} depending on the concentration of IP_3 mimicking IP_3 sensitive receptors. The chemical equations are:

$$\begin{aligned}
\text{ERout}: \quad & \mathrm{Ca_{ER}^{2+}} \overset{\mathrm{IP_3}}{\rightleftharpoons} \mathrm{Ca_c^{2+}} \\
\text{SERCA}: \quad & \mathrm{Ca_c^{2+}} + \frac{1}{2}\mathrm{ATP_c} + \frac{1}{2}\mathrm{H_2O_c} \rightleftharpoons \mathrm{Ca_{ER}^{2+}} + \frac{1}{2}\mathrm{ADP_c} + \frac{1}{2}\mathrm{Pi_c} \\
\text{NCX}: \quad & \mathrm{Ca_m^{2+}} + 3\,\mathrm{Na_c^+} \rightleftharpoons \mathrm{Ca_c^{2+}} + 3\,\mathrm{Na_m^+} \\
\text{MCU}: \quad & \mathrm{Ca_c^{2+}} \rightleftharpoons \mathrm{Ca_m^{2+}} \, .
\end{aligned}$$

To conclude, our model considers the dynamics of ATP hydrolysis in the cytosol described by a reversible reaction (Hyd) [225] to mimic other cellular activities as

$$\text{Hyd}: \quad \mathrm{ATP_c} + \mathrm{H_2O_c} \rightleftharpoons \mathrm{ADP_c} + \mathrm{Pi_c} \, .$$

Chemical species whose concentration is considered constant (and hence treated as fixed parameters) are highlighted in gray.

5.3 Mathematical Model

The metabolic and calcium modelling combined in this work [99, 225] have been defined by a PDE and an ODE, respectively. Here, we keep the distinction

between describing the metabolic model *via* a reaction diffusion system and the calcium signalling model by a kinetic dynamic model described by ODEs.

5.3.1 PDE System

The metabolic model presented in the previous section is defined mathematically through a reaction-diffusion system of partial differential equations. Considering Ω being a bounded domain of dimension d ($d = 2, 3$), we look for the concentrations ($[\cdot] : \Omega \times [0, T] \to \mathbb{R}$), $[\mathrm{GLC}]_c$, $[\mathrm{ATP}]_c$, $[\mathrm{ADP}]_c$, $[\mathrm{GLY}]_c$, $[\mathrm{PYR}]_c$ and $[\mathrm{LAC}]_c$, for all $x \in \Omega$ and for all $t \in [0, T]$ such that

$$
\begin{cases}
\frac{\partial [\mathrm{GLC}]_\mathrm{c}}{\partial t} = & D_{\mathrm{GLC}} \nabla^2 [\mathrm{GLC}]_\mathrm{c} - K_{HXK} [\mathrm{GLC}]_\mathrm{c} [\mathrm{ATP}]_\mathrm{c}^2 + J_{\mathrm{in}} \\
\frac{\partial [\mathrm{ATP}]_\mathrm{c}}{\partial t} = & D_{\mathrm{ATP}} \nabla^2 [\mathrm{ATP}]_\mathrm{c} - 2K_{HXK} [\mathrm{GLC}]_\mathrm{c} [\mathrm{ATP}]_\mathrm{c}^2 \\
& + 2K_{PYRK} [\mathrm{ADP}]_\mathrm{c}^2 [\mathrm{GLY}]_\mathrm{c} - J_{\mathrm{Hyd}} + \delta J_{\mathrm{ANT}} - \frac{1}{2} J_{\mathrm{SERCA}} \\
\frac{\partial [\mathrm{ADP}]_\mathrm{c}}{\partial t} = & D_{\mathrm{ADP}} \nabla^2 [\mathrm{ADP}]_\mathrm{c} + 2K_{HXK} [\mathrm{GLC}]_\mathrm{c} [\mathrm{ATP}]_\mathrm{c}^2 \\
& - 2K_{PYRK} [\mathrm{ADP}]_\mathrm{c}^2 [\mathrm{GLY}]_\mathrm{c} + J_{\mathrm{Hyd}} - \delta J_{\mathrm{ANT}} + \frac{1}{2} J_{\mathrm{SERCA}} \\
\frac{\partial [\mathrm{GLY}]_\mathrm{c}}{\partial t} = & D_{\mathrm{GLY}} \nabla^2 [\mathrm{GLY}]_\mathrm{c} + 2K_{HXK} [\mathrm{GLC}]_\mathrm{c} [\mathrm{ATP}]_\mathrm{c}^2 \\
& - K_{PYRK} [\mathrm{ADP}]_\mathrm{c}^2 [\mathrm{GLY}]_\mathrm{c} \\
\frac{\partial [\mathrm{PYR}]_\mathrm{c}}{\partial t} = & D_{\mathrm{PYR}} \nabla^2 [\mathrm{PYR}]_\mathrm{c} + K_{PYRK} [\mathrm{ADP}]_\mathrm{c}^2 [\mathrm{GLY}]_\mathrm{c} \\
& - K_{LDH} [\mathrm{PYR}]_\mathrm{c} - \delta J_{\mathrm{PyrEx}} \\
\frac{\partial [\mathrm{LAC}]_\mathrm{c}}{\partial t} = & D_{\mathrm{LAC}} \nabla^2 [\mathrm{LAC}]_\mathrm{c} + K_{LDH} [\mathrm{PYR}]_\mathrm{c} - \eta_{\mathrm{LAC}}(x, t) [\mathrm{LAC}]_c \,,
\end{cases}
\tag{5.4}
$$

where Ds are the positive diffusion coefficients, Ks are the classical reaction rate of the law of mass action and δ is the volume ration between mitochondria and cytosol. J_{in} is the source of glucose defined as

$$
J_{\mathrm{in}}(x, t) = \begin{cases} \alpha \in \mathbb{R} \quad \text{if} \quad (x, t) \in \Omega_{\mathrm{in}} \times [0, T], \quad \text{where} \quad \Omega_{\mathrm{in}} \subset \Omega \\ 0 \quad \text{otherwise.} \end{cases} .
$$

The outflux of lactate is defined as:

$$\eta_{\mathrm{LAC}}(x,t) = \begin{cases} \eta \in \mathbb{R} \quad \text{if} \quad (x,t) \in \Omega_{\mathrm{out}} \times [0,T], \quad \text{where} \quad \Omega_{\mathrm{out}} \subset \Omega \\ 0 \quad \text{otherwise.} \end{cases} .$$

We impose pure Neumann boundary conditions:

$$\nabla[u] \cdot n = 0 \quad \partial\Omega \quad u = \{\mathrm{GLC}, \mathrm{ATP}, \mathrm{ADP}, \mathrm{GLY}, \mathrm{PYR}, \mathrm{LAC}\}.$$

The system is complete with initial conditions for each specie at initial time. In Equation (5.4), we have highlighted in blue the fluxes that communicate with the ODE system.

5.3.2 ODE System

The ODE system from [225] has been adapted with the addition of two equations that describe the pyruvate in the cytosol (PYR_c) and the acetyl Co-A (AcCoA). The system is solved by finding the concentrations ($[\cdot] : [0,T] \to \mathbb{R}$), such that:

$$
\begin{cases}
\mathrm{d}_t[\mathrm{PYR}]_\mathrm{m} = J_{\mathrm{pyrEx}} - J_\mathrm{pdh} \\
\mathrm{d}_t[\mathrm{AcCoA}]_\mathrm{m} = J_\mathrm{pdh} - J_{CS} \\
\mathrm{d}_t[\mathrm{ADP}]_\mathrm{m} = J_\mathrm{ANT} - J_\mathrm{F1} - J_\mathrm{SL} \\
\mathrm{d}_t[\alpha\mathrm{KG}]_\mathrm{m} = J_\mathrm{IDH} - J_\mathrm{KGDH} \\
\mathrm{d}_t[\mathrm{ATP}]_\mathrm{m} = -J_\mathrm{ANT} + J_\mathrm{F1} + J_\mathrm{SL} \\
\mathrm{d}_t[\mathrm{Ca}^{2+}]_\mathrm{c} = \frac{f_\mathrm{c}}{\gamma}(-J_\mathrm{SERCA} + J_{\mathrm{ER}_{out}} + \delta(J_\mathrm{NCX} - J_\mathrm{MCU})) \\
\mathrm{d}_t[\mathrm{Ca}^{2+}]_\mathrm{m} = \frac{f_\mathrm{m}}{\gamma}(J_\mathrm{MCU} - J_\mathrm{NCX}) \\
\mathrm{d}_t[\mathrm{CIT}]_\mathrm{m} = J_\mathrm{CS} - J_\mathrm{ACO} \\
\mathrm{d}_t[\mathrm{FUM}]_\mathrm{m} = J_\mathrm{SDH} - J_\mathrm{FH} \\
\mathrm{d}_t[\mathrm{ISOC}]_\mathrm{m} = J_\mathrm{ACO} - J_\mathrm{IDH} \\
\mathrm{d}_t[\mathrm{MAL}]_\mathrm{m} = J_\mathrm{FH} - J_\mathrm{MDH} \\
\mathrm{d}_t[\mathrm{NAD}]_\mathrm{m} = J_\mathrm{Ox} - J_\mathrm{IDH} - J_\mathrm{KGDH} - J_\mathrm{MDH} - J_\mathrm{pdh} \\
\mathrm{d}_t[\mathrm{NADH}]_\mathrm{m} = -J_\mathrm{Ox} + J_\mathrm{IDH} + J_\mathrm{KGDH} + J_\mathrm{MDH} + J_\mathrm{pdh} \\
\mathrm{d}_t[\mathrm{OAA}]_\mathrm{m} = J_\mathrm{MDH} - J_\mathrm{CS} \\
\mathrm{d}_t\Delta\Psi = \frac{1}{C_\mathrm{m}}(10J_\mathrm{Ox} - 3J_\mathrm{F1} - J_\mathrm{ANT} - J_\mathrm{Hl} - J_\mathrm{NCX} - 2J_\mathrm{MCU}) \\
\mathrm{d}_t[\mathrm{SCoA}]_\mathrm{m} = J_\mathrm{KGDH} - J_\mathrm{SL} \\
\mathrm{d}_t[\mathrm{SUC}]_\mathrm{m} = J_\mathrm{SL} - J_\mathrm{SDH}\ .
\end{cases}
\tag{5.5}
$$

Fluxes are explicitly stated in Appendix C in Table C.1. The system is completed with initial condition for each specie at the initial time. In Equation (5.5), we have highlighted in blue the fluxes that communicate with the PDE system.

5.4 Methods

We discretise the time interval and solve the PDEs and ODEs at each time step. To solve the PDEs, we compute the fluxes using the solution of the ODEs at the previous time step. Afterwards, the ODEs solution is computed with the most recent values of the concentrations solved in the PDEs.

The PDEs model Equation (5.4) is solved using classic finite element method implemented in FEniCS [138]. The solution of the PDEs is defined in the space of P1 Lagrange elements, and the solver is a classic built-in solver, Newton [185], of FEniCS. The time is discretised using a backwards Euler. For more detail on the implementation we refer to [97].

The interaction between the two systems is enabled by solving the ODEs at each nodal point of the finite element mesh. Due to the stiffness of the ODE system, we solve using an implicit scheme, Euler backwards, solved at each degree of freedom of the mesh. The ODEs output is used as a input for the PDEs by projecting the solutions into the discontinuous Lagrange space.

5.5 Results

In this section, we present our first results on investigating the effect of calcium and metabolism interaction in our spatially resolved metabolic model. The parameters based on literature and the initial conditions for the chemical species are shown in the Appendix C in Section C.2 and Section C.3.

First, we validate the coupled model, comparing the results with the associated ODE system. Then, we investigate the effect of different spatial geometrical domain on the output. Last we consider the shortage of energetic substrate by deprivating the cell from a percentage of glucose influx.

5.5.1 Validation of the Coupled PDE-ODE System

To validate our combined model, we show that the solution of the coupled metabolic-calcium model (Equations (5.4)-(5.5)) converges to the solutions of the associated ODE system.

To assess the PDE-ODE model's convergence to the associated system, we solve it in a small spatial domain to mimic a system where reactions are not limited by diffusion. Hence, we consider a circular domain with radius $\sqrt{3}\,\mu$m. We locate the influx of GLC and the exit of LAC in a surrounding of two antipodal points. These surroundings are defined as the intersection

of the domain with a circle centred in the selected points and a radius 0.3 μm (Figure 5.2**a**).

The associated ODE system is solved using two different solvers. First, we consider the built-in *LSODA* solver of *scipy* which was already used for the original system in [225]. Second, we consider an Implicit Euler solver to assess it as a valid choice for the coupling. The time step for the coupled model is set to 0.01 as the Euler solver for the associated ODE system.

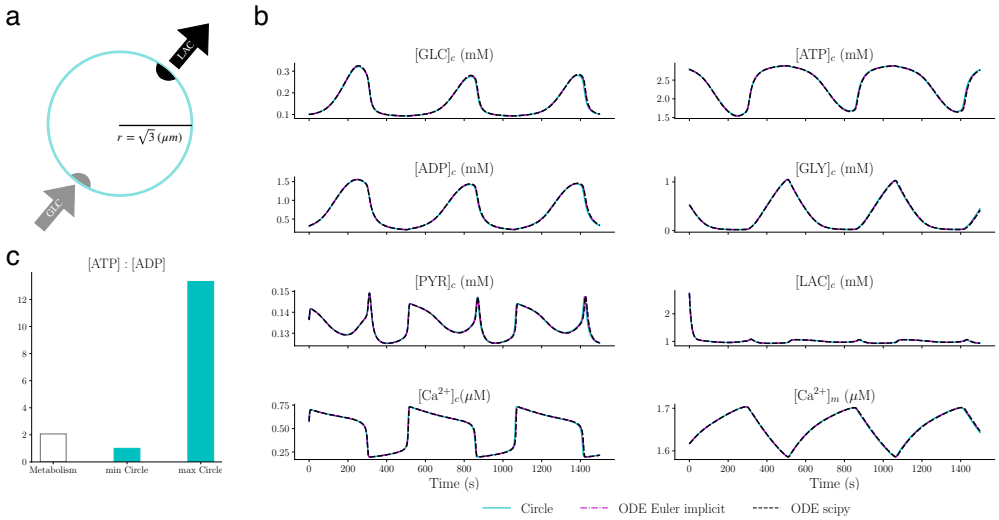

Fig. 5.2 **a** Spatial setting of the two dimensional simulation in a 2D circle of radius $\sqrt{3}$. GLC enters from one point and LAC exits from the antipodal point.**b** dynamics of the ODE system associated (dashed lines) and the spatial average concentration in the circle for the metabolites and Ca^{2+} in cytosol and mitochondria (Circle in cyan, ODE solved with Euler magenta and ODE solved with *scipy* in black dashed line). **c** Comparison of average ATP : ADP obtained in the two-dimensional simulations from Chapter 4 Figure 4.2**e** (white) and the minimum and maximum ratio from the average simulation in the circle (cyan).

Figure 5.2**b** presents the behaviour of the metabolic species and the Ca^{2+} in the cytosol and mitochondria in the time interval $[0, 1500]$. For the PDE-ODE coupling, the plotted solution is the average concentration at each time step. The results show convergence in all three applied methods.

Comparing the interaction of the metabolic-calcium model to our previous work [99], we notice that the calcium oscillation is induced in the whole system

of metabolites. Moreover, comparing the average ATP : ADP from Section 4.3.1 (Figure 4.2**e**) with the minimum and maximum ratio of the coupled system in the circle (Figure 5.2**c**), it is visible the improvement of the cellular energetic maximum status.

In conclusion, the implicit Euler scheme is an appropriate choice to solve the ODE in our coupled model. Our PDE-ODE coupled model in a small domain converges to the ODE of the associated system. The benefit of the calcium signalling on our previously proposed model is already evident by a higher average value of ATP.

5.5.2 Metabolic-Calcium Dynamics in 2D Domains

After validating our coupled scheme, we investigate the spatial effect on the system. As a first approach, we consider a circular and a star-shape domain in two dimensions (Figures 5.3**a-b**). The circular domain is set up as in the previous experiment. However, the diameter is now biologically significant, set to $140\,\mu$m, as the spatial extent of a typical astrocyte [165]. Based on the diameter of the circle, we build the star shape. The GLC enter and LAC exit locations are placed on two vertices of the star. We set the distance between these two vertices equal to the circle diameter. The subregions are defined for the circle and the star as the intersection of their respective domain with circles of radius $10\,\mu$m.

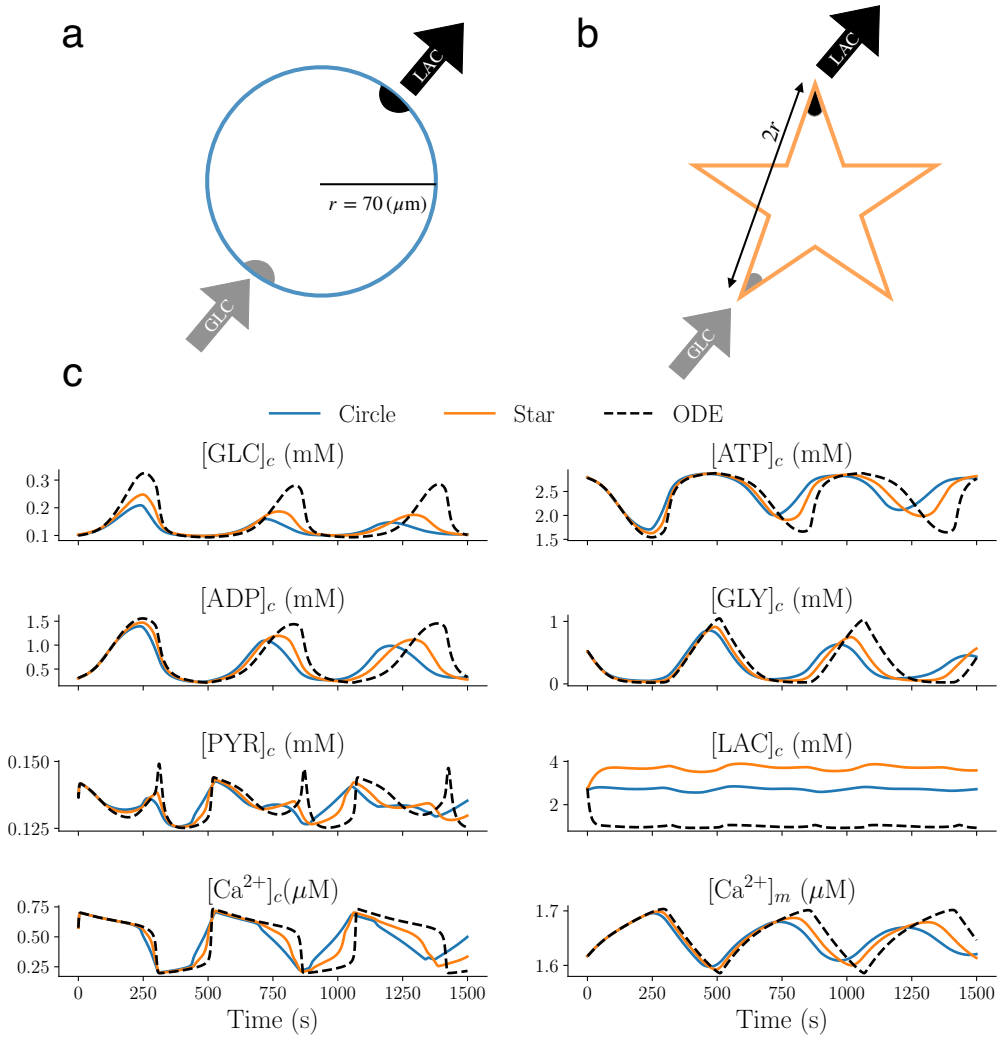

Fig. 5.3 **a-b** Spatial setting of the circular and star shape domain. The distance between the two vertices of the star is equal to the circle diameter. **c** Dynamics of concentration for the ODE system associated (black dashed), circle (blue) and star (orange).

Figure 5.3**c** shows the system's dynamics for the two-dimensional domains and the associated ODE system as reference. The spatial domain models add the crucial role of the diffusivity of the species solved by the PDEs. The effect of the diffusion flattens the oscillation of the chemical concentration species in the spatial experiments compared to the ODEs. However, the system behaviour is in agreement with the ODEs. The spatial models lower the oscillation

amplitude at larger time steps, suggesting that the system is still converging towards the oscillatory steady state with damped oscillation compared to the ODEs. The chemical species most affected by the spatial solution is LAC. LAC, a crucial component for astrocytic metabolism, is much higher in the spatial models compared to the ODE associated. The diffusion effect is responsible for the high lactate levels. The lactate molecules are first required to be produced. Then they need to travel to the region where they are exported, contrary to the ODEs, where production and export of lactate are independent of the position. Moreover, the higher levels of LAC obtained in the star-shape domain follow our findings in Chapter 4, indicating that a more complex morphology might interfere with the molecules' diffusivity.

Investigating the energetic production of the different systems, we compare in Figure 5.4**a** the minimum and maximum quantity of ATP : ADP and show Figure 5.4**b** the changes of the latter in time. The ratio must be more than 1 to indicate a healthy cellular status [217]. The ODE system associated presents the highest amplitude, followed by the star shape and last from the circle. In contrast, the circle shows faster oscillation followed by the star and the ODEs. Moreover, we compare in Figure5.4**d** the two main metabolic productions, LAC and ATP versus Ca^{2+}. This plot highlights the good performance from a metabolic point of view, with high values of LAC and ATP, for the three experiments pointing to the importance of the more complex morphology of the star. Compared to our results investigating the altruistic-egoistic behaviour in Chapter 4, the spatial results here exhibit a high concentration of both ATP and LAC in the cytosol, suggesting the bursting effect of cytosolic calcium dynamics on the metabolism. Moreover, Ca^{2+} affects the egoistic-altruistic balance adding an oscillatory behaviour. The spiral behaviour is better shown in Figure 5.4**e** where Ca^{2+} and ATP change over time. The three experiments show a spiral behaviour that decreases in amplitude over time for the spatial experiments, suggesting that in time the spatial experiments will reach the oscillatory steady state with lower oscillatory amplitude but with a similar cyclic trend as the ODEs.

In Figure 5.4**c**, we consider the relationship between mitochondrial pyruvate and cytosolic calcium. These two species are related because PYR_m is then transformed by pdh into AcCoA fundamental for the activation of the TCA cycle. The two species showed a relationship through their maximum and

minimum points. In the minimum calcium points, PYR_m clearly shows a point of maximum and maximum points of Ca^{2+} correspond to maximum points of PYR_m. Also, in this case, the ODE performs smooth functions compared to spatial domains. Moreover, we can appreciate the difference between pyruvate's star and circle behaviour, where PYR_m displays sharper peaks in the star than in the circle.

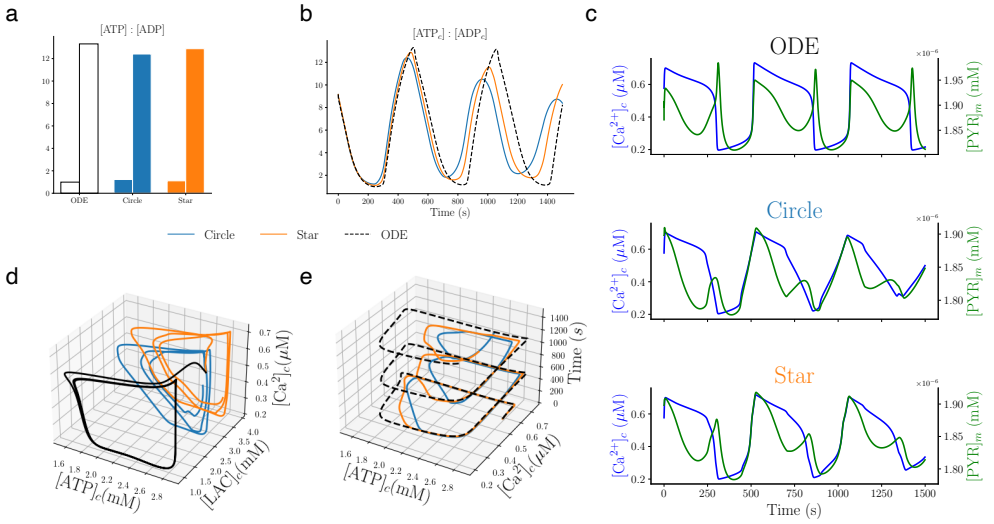

Fig. 5.4 **a** Histogram of minimum and maximum ATP : ADP for the ODE system associated (white), average for circular (blue) and star-shape (star) domains. **b** ATP : ADP changing in time. The circular and star-shape domains show the average concentration at each time step. **d** three-dimensional plot of ATP, LAC and Ca^{2+} in the cytosol for the three experiments. **e** three-dimensional plot in time of Ca^{2+} and ATP showing their spiralling behaviour for the three experiments. The two spatial experiments decrease the oscillatory amplitude in time.**c** cytosolic calcium Ca^{2+} plotted and mitochondrial PYR plotted in time for the ODE (top), circle (middle), star (bottom).

Next, we investigate the interplay between Ca^{2+} and metabolism in the three experiments of ATP and cytosolic Ca^{2+} in the spatial domains (Figures 5.6 and 5.5). The dynamics are shown in the right plot of Figures 5.6 and 5.5 for a time interval $[0, 550](s)$, the two systems exhibit similar trends. On the left side of Figures 5.6 and 5.5, we plot ATP and Ca^{2+} spatial results for four-time steps. We consider four times: the initial time ($t = 0\,(s)$), $t = 250\,(s)$, $t = 500\,(s)$ and

$t = 540\,(\mathrm{s})$. At the initial time, both ATP and Ca^{2+} are homogeneous in high concentrations. At time 250(s), ATP is close to its minimum, while there is a high Ca^{2+} concentration. Phase opposition that is also present in ODE model from Voorsluijs *et al.* [225]. Spatially the results are non-homogeneous. ATP is produced close to the GLC influx and low in the rest of the cell, opposite behaviour for the Ca^{2+}. At time $500\,(\mathrm{s})$, ATP is close to its maximum point. In accordance, the spatial solution shows high concentrations. On the other hand, Ca^{2+} concentration goes from its point of minimum to maximum. In the spatial solutions, we see the heterogeneity of concentration levels. Last, at time $540\,(\mathrm{s})$, both concentrations are at a high level. Between the spatial results of the circle and the star, we can notice the geometrical effects, mostly at times $250\,(\mathrm{s})$ and $500\,(\mathrm{s})$. At these two time steps, we can notice that transport of matter proceeds faster in the circular domain compared to the star domain. For example, the trapping effect in the branches of the star is visible at $t = 500\,(\mathrm{s})$ and impacts Ca^{2+} concentration, which is lower in these regions of the domain. In Voorsluijs *et al.* [225], we could see only phase opposition between ATP and Ca^{2+} concentrations. However, our coupled model showed a much more complex behaviour of the species adding the heterogeneity of concentration solved in a spatial domain which is then affected by the geometrical domain choice.

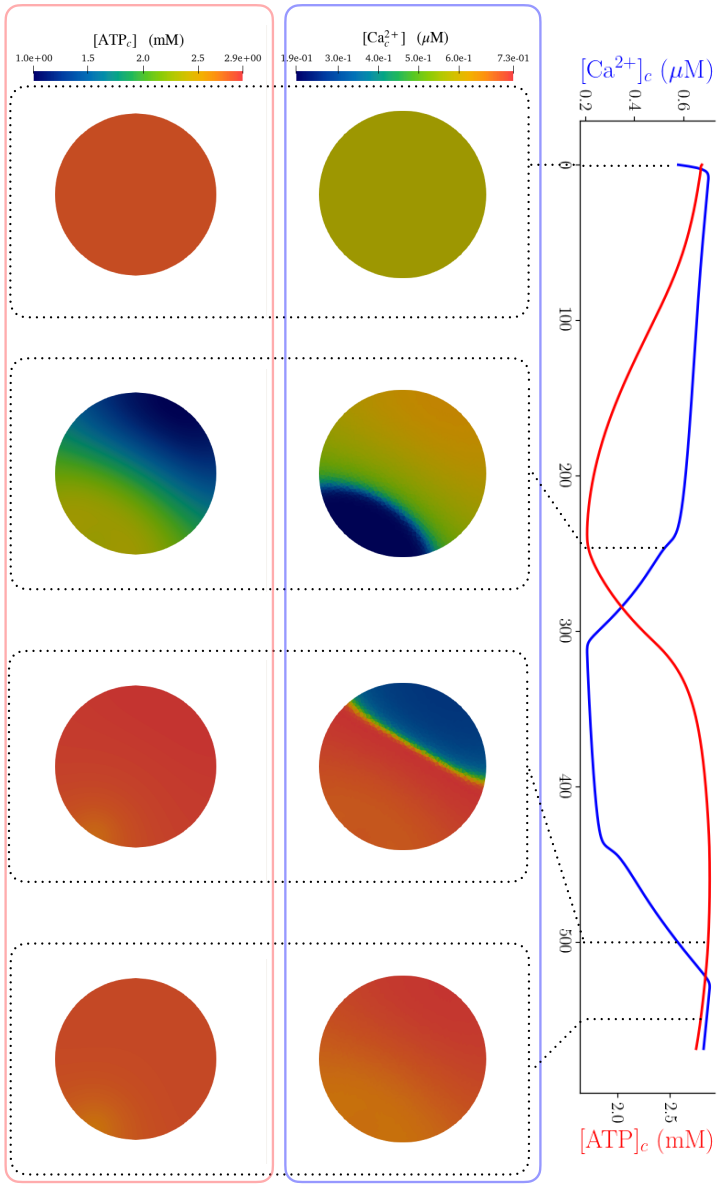

Fig. 5.5 Circle domain's spatial results (left) of cytosolic ATP (red box) and cytosolic Ca^{2+} (blue box), plotted at four time steps. The interplay dynamics of ATP and Ca^{2+} (Right) shows the four time selected ($t = \{0, 250, 500, 540\}$ (s)). High calcium levels induce low ATP and *viceversa*.

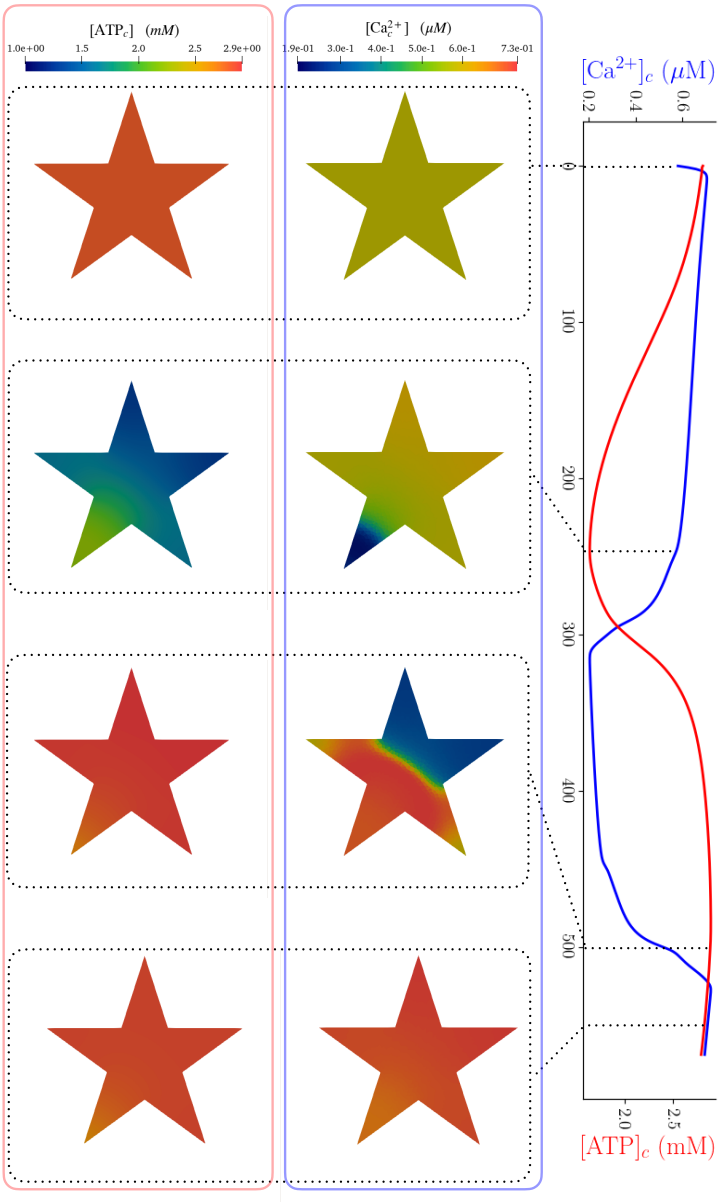

Fig. 5.6 Star shape domain's spatial results (left) of cytosolic ATP (red box) and cytosolic Ca^{2+} (blue box), plotted at four time steps. The interplay dynamics of ATP and Ca^{2+} (Right) shows the four time selected ($t = \{0, 250, 500, 540\}$ (s)). High calcium levels induce low ATP and *viceversa*.

Compared to our previous work [99], calcium dynamics pushes the cell to perform better metabolically with high ATP and high LAC and inducing

oscillations. This improvement is favoured by the geometries of the cellular space considered. In agreement with Chapter 4 because of the trapping effect, the star shape geometry performs better than the circle, and the spatial results strengthen our belief that a more complex shape benefits the system due to molecules' trapping effects. These preliminary results represent an exciting development to study the interplay of metabolism and calcium signalling in spatial domains. Moreover, they allow us to investigate the system in dysfunctional behaviour, similar to what we did in Chapter 4 for the astrocytic morphology.

5.5.3 Effect of Glucose Impairment on the Metabolic-Calcium Model

In this *in silico* experiment, we want to investigate the behaviour of the metabolic-calcium model in the presence of glucose dysfunction. We test our model considering that only 95% of the glucose was imported inside the cell. First, we assess the ODE system's behaviour (Figure 5.7). Interestingly, it directly shows the sensitivity of the system towards changes in GLC. The lower GLC uptake induces the cell to consume the ATP present in the cell's cytosol too quickly. Consequently, the glycolysis is blocked, and GLC accumulates in the cell. Moreover, the low level of ATP in the cytosol block the exchanges of Ca^{2+} with the ER, disrupting calcium signalling.

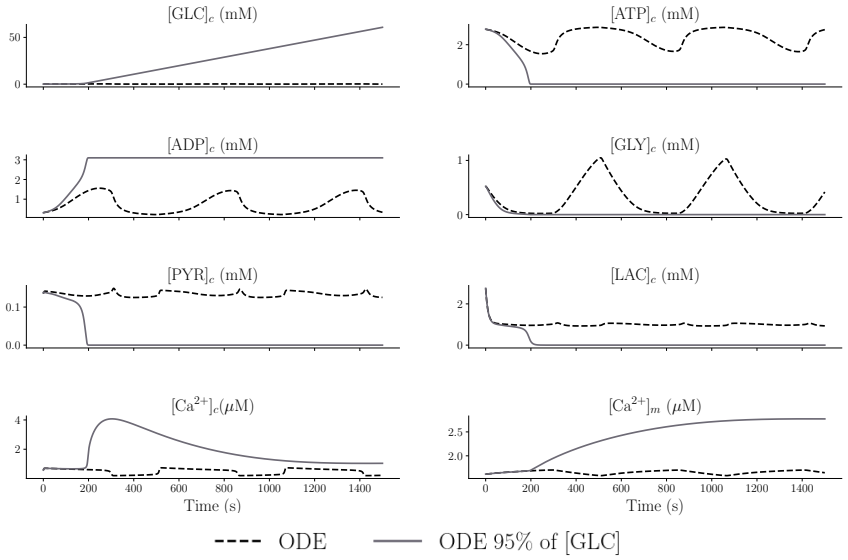

Fig. 5.7 Dynamics of the ODE systems associated to the metabolic-calcium model. The dynamic behaviour of the metabolites and the calcium shows that diminishing the GLC uptake to 95% (gray) leads the fast consumption of ATP blocking the system.

We run the same deficiency of GLC inside the circle (Figure 5.8**a**) and the star shape (Figure 5.9**a**) in our coupled model. The diffusivity of the chemicals is then playing a pivotal role, and the oscillations then survive, suggesting that the spatial model, including diffusivity and space, is making the system more robust (Figures 5.8**b** and 5.9**b**). The lower GLC uptake increases the oscillation amplitude for GLC, ATP ADP showing the susceptibility of the system and the thin balance between these species that lead the ODEs to not reach the steady state.

Figures 5.8**c** and 5.9**c** shows ATP and Ca^{2+} dynamics in the cytosol. Biologically the decrease of nutrients should lead to faster calcium spiking [155]. This trend is slightly visible in the star shape domain, while we cannot observe this behaviour in the circle. This suggests again that a star shape is more biologically significant than a circle for the system behaviour.

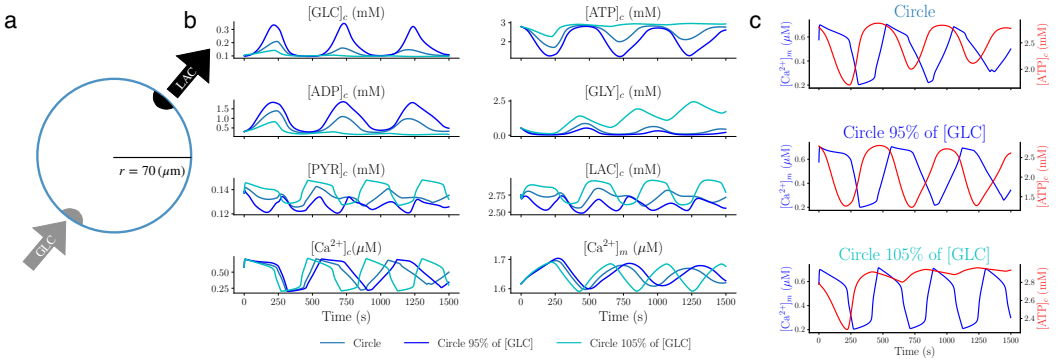

Fig. 5.8 **a** The setting of the circular domain simulation. **b** average concentrations dynamic of the system for normal GLC uptake (blue), 95% GLC uptake (dark blue) and 105% GLC uptake (cyan). **c** Dynamic of Ca^{2+} and ATP in the cytosol for normal GLC uptake (top), 95% GLC uptake (middle) and 105% GLC uptake (bottom).

Even if the spatial results show a higher robustness in glucose deficiency compared to the ODE, decreasing the glucose uptake to 90% was already showing the same ODE system behaviour (Figure 5.7).

On the other hand, considering an increase of the GLC influx of 105%, the system presents lower amplitude than normal condition (Figures 5.8**b** and 5.9**b**). However, the systems present another dysfunctional behaviour. GLY starts accumulating in the cell, preventing the system from reaching a steady state.

To conclude, these experiments with 90% and 105% GLC uptake show dysfunctional behaviour in glycolysis. These results suggest that our model might benefit from a better modelling interaction choice between GLC and ATP. Thus, their interaction could be improved by investigating alternative modelling ways. Nevertheless, the spatial model highlights how the spatial component and chemical diffusivity made the system more robust to glucose deficiency.

5.6 Discussion

Glucose metabolism and calcium signalling are two fundamental functions in cells, particularly in astrocytes. Investigating these functions is fundamental to

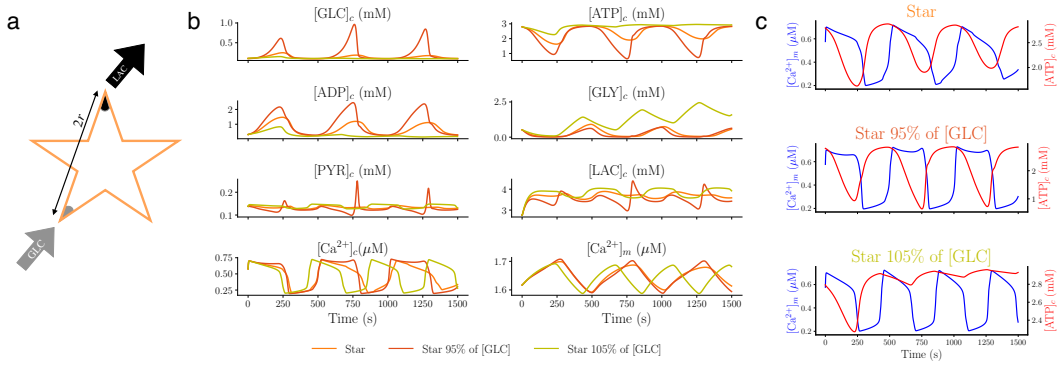

Fig. 5.9 **a** The setting of the star shape domain simulation. **b** average concentrations dynamic of the system for normal GLC uptake (orange), 95% GLC uptake (dark orange) and 105% GLC uptake (yellow). **c** Dynamic of Ca^{2+} and ATP in the cytosol for normal GLC uptake (top), 95% GLC uptake (middle) and 105% GLC uptake (bottom).

discover new insights in disease developments. A hallmark for astrocytes in neurodegeneration is low energy production [136, 156, 178] and morphological changes [94]. Studying the interplay between these two cellular functionalities can be done with the help of mathematical models. Many models studied calcium signalling and metabolism separately. However, calcium requires ATP to be transferred from the cytosol to ER, and, on the other hand, calcium in mitochondria is used to activate key enzymes in the TCA cycle and thereby enhances the flux of high energy electrons to the electron transport chain and the ATP production by enzyme complexes in the inner mitochondrial membrane. Due to this interplay, it is also necessary to study these two processes together and, in sight of our work on spatially resolved metabolic model, with a geometric-based model. Therefore, we proposed to couple together two existing models. We consider our previously proposed metabolic model solved in spatial domains through a reaction-diffusion system [99] and the kinetic dynamic calcium model proposed in [225]. We solve these models as a PDE system coupled with an ODE system. The two models are merged, adding two additional chemical species which are PYR_m and AcCoA.

Our first results showed the exciting effect of the spatial model on the coupling between these two processes. First, in Section 5.5.1, we have validated our coupled scheme by comparing it to the associated ODE system. The system showed the classic oscillatory calcium behaviour reflected in the whole

metabolism. Then, we considered two 2D spatial domains, the circle and a star shape (Section 5.5.2). The diffusivity affects the chemical species' behaviour by smoothing out the oscillation amplitude compared to the ODE. The coupled model is more efficient in terms of ATP and LAC production compared to the ODE. The calcium and ATP behaviour is in line with biological expectations: peaks in ATP are followed by peaks in Ca^{2+}. Moreover, the spatial results showed the heterogeneous concentrations level of ATP and Ca^{2+}. In particular, the geometrical effect of the star shape are visible in the branches concentrations, confirming our hypothesis of the molecular trapping effect in more complex domains. Therefore, a complex domain ensures higher cellular metabolic performance comparing LAC levels in the two shapes.

Last, we consider GLC impairment to simulate dysfunctional cellular glucose uptake [159] (Section 5.5.3). Our findings highlight that the coupled system is more robust than the associated ODE. The diffusivity is the key to simulate buffering effect and robustness. However, these experiments pointed also to a limitation in our model. The system is susceptible to small changes in glucose, indicating the necessity to investigate further the relationship between GLC and ATP. A possibility is to change the glycolysis model to keep a better balance between these two species. Moreover, the Ca^{2+} and ATP behaviour is more biologically significant in the star shape compared to the circle pointing towards the impact of complex morphologies.

In conclusion, our model combines spatial metabolic and calcium kinetic models. The coupling is fundamental for investigating the interaction between these two processes. Our preliminary results require further investigation. Nevertheless, our results indicate that the geometric and diffusivity component is essential for the system output.

CHAPTER 6

Conclusion

This thesis aimed to investigate the metabolism of astrocytes in relation with their morphologies in neurodegeneration. We discussed the motivation and objectives of this project in Sections 1.1 and 1.2 respectively, highlighting the interdisciplinarity of the work.

In Chapter 2, we presented a comprehensive overview of the state-of-the-art of involved disciplines and detailed the scientific background of the methodologies applied in this thesis. For this purpose, we discussed the centrality of astrocytes in the brain, focusing on their metabolism and morphologies, and highlighted the changes in these features in neurodegeneration (Section 2.1). We introduced systems biology as an interdisciplinary model-based approach to investigate complex biomedical mechanisms and in particular the unknowns in brain energy metabolism. When discussing the state-of-the-art of metabolic models, we indicated the need for investigating geometry-based cellular models and highlighted the lack of such approaches. Finally, we concluded the chapter by reviewing some numerical methods to solve geometry-based models.

6.1 Main Contributions

Within a widely used open source computational code base (FEniCS [138]), this thesis presented a flexible and easy-to-use image-based modelling approach to study metabolic dynamics in actual physiological geometries. In Section 1.2, we presented the first research question to reach our overarching goal:

"Which computational approach is best suited to deal with the complex morphologies of cells directly from cellular images and keeping stability and robustness in focus? "

We addressed this question in Chapter 3. Astrocytes require a numerical method that allows to include complex morphologies as a simulation domain. As an ideal candidate for handling complex geometries, we investigated the existing cut finite element method proposed in [58] and based on the idea of partition of unity introduced in [18] and recently surveyed in [38]. CutFEM is adapted to complex geometries defined by images since the domain is implicitly described as a level set function [206] on a simple non-conforming background mesh. In contrast, the classical finite element method requires a more complex mesh conforming to the object's boundary.

Hence, we compared the results of our proposed metabolic model for increasingly complex domains with the classical FEM and CutFEM. We thus established the validity of CutFEM to solve complex diffusion-reaction systems on arbitrary complex geometries. Moreover, the open-source code allows adapting our framework to any set of coupled PDEs on complex geometries.

After establishing a suitable numerical approach, we directed our research to the following question:

"How relevant are the spatial organisation of reaction sites inside the cell and different geometries for the output of the metabolic system?"

The question was addressed in our second manuscript [99] presented in Chapter 4. First, we proposed an improved energy metabolism model based on physiological astrocytic parameters. Then, we used simple two-dimensional geometries to investigate the relevance of the spatial orchestration of the reaction sites. The steady-state of the metabolic system showed a clear dependence on the intra-cellular organisation. Moreover, geometrical differences between a

circle and the star domain were reflected in the level of the final metabolite concentrations. When exploring a more significant number of reaction sites in a rectangular domain, we characterised the energetic cellular status based on the distribution of mitochondria. Overall, our two-dimensional investigation proved the impact of spatial arrangements on the metabolite profiles highlighting the necessity of including spatial arrangements in future modelling. These results are in accordance with the fundamental role of mitochondria distribution in cells [104, 137] and with the necessity of refining the metabolic model [2].

In the second part of Chapter 4, we used confocal microscopy images of astrocytes from human post-mortem brain samples with a reactive astrocyte from an Alzheimer's disease sample and a representative astrocyte from an age-matched control sample as our simulation domains. Following our previous work [97], we solved the model using CutFEM and described the astrocytes implicitly through a level-set function defined from the microscopic images. We then addressed the two specific research questions:

"How is the physiological morphology of astrocytes relevant to their metabolic role? How can our model be used in physiological geometries to study neurodegeneration in AD?"

Our three-dimensional experiments showed that complex morphologies ensured the robustness of the metabolic system toward extreme reaction site configurations. We then simulated AD-related metabolic dysfunctions [159, 136, 156, 33] and found that a single dysfunction impacts the system but does not necessarily lead to an unhealthy energetic status of the cell. However, the sum of all the metabolic dysfunctions led the cell to a state of energetic demand. This combined response might be related to the multi-hit perspective in neurodegeneration [173, 236]. Moreover, examining the individual dysfunctions suggested that reducing LDH activity could help astrocytic function, in accordance with cancer studies [126, 107]. In conclusion, our model incorporated confocal microscopy images to infer the astrocytic shapes paving the way to new *in silico* experiments that can help to compensate for the lack of human *in vivo* samples. Moreover, we showed the applicability of our approach to studying impaired brain energy metabolism in neurodegenerative diseases at unprecedented resolution.

Finally, Chapter 5 addressed the question:

"What is the interplay between glucose metabolism and calcium signalling in a spatially resolved domain of a cell?"

For this purpose, we coupled our developed metabolic model with a dynamic model of calcium signalling with a focus on ATP [225]. Our first results show that the coupled systems can improve cellular energy metabolism. Our model captured the energetic and calcium interaction in the cytosol. Furthermore, we showed the system's robustness compared to the ODE system under the substrate, i.e. glucose, deficient condition. Even if it is a work in progress, we presented promising results to investigate better the interplay between two key features of astrocytes in spatial domains.

To summarise, our main contributions are

- a reaction-diffusion system based on CutFEM for central energy metabolism including a step-by-step implementation,
- a numerical indication of the impact of different spatial arrangements of reaction site on the metabolite concentrations,
- an image-based computational model for real human astrocytes suitable to study energy metabolism in neurodegenerative diseases,
- a coupled model to investigate glucose metabolism and cellular signalling in spatial domains.

6.2 Perspectives and Future Applications

The work presented in this thesis has proven to pave the way for many new and exciting investigations on the relation between metabolism and geometries in astrocytes. However, the reason why astrocytes undergo morphological changes and their role in neurodegeneration remains to be clarified. In this last section, we want to discuss the future perspective and future research directions opened by the work in this thesis.

6.2.1 Discretization

In our first paper [97], we applied CutFEM to deal with geometries complexity. However, working with 3D astrocytic images is computationally very expensive. The addition of moving interfaces in CutFEM is still under investigation [69] and gets more challenging with a highly complex shape such as those of an astrocyte. Other numerical tools presented in Section 2.4 can be investigated. Furthermore, we could use error estimation to optimize the quality of the mesh [89, 56, 55] for a given quantity of interest, e.g. energy production ATP. This would enable to optimize the computational model to control the geometrical, boundary condition and quantity of interest. We could also ensure the accuracy of the solution by measuring the discretization error [37, 54, 88]. Moreover, the parameters of the model are uncertain. Papers on uncertainty quantification [113, 189] should be developed to investigate parametric uncertainties and their impact on quantities of interest. The interplay between discretisation error and model/parameter uncertainty would be desirable.

6.2.2 Modelling

The metabolic model proposed in our work [97, 99] was beneficial in proving the pivotal role of spatial distribution in the cell. However, it is a coarse-grained model with chemicals modelled simply using the law of mass action. Therefore, we could consider more detailed enzymatic models [61, 71]. The first step in this direction has been done in our metabolic-calcium coupled model.

Moreover, on the coupled calcium signalling and metabolism model (Chapter 5), we already discussed the model limitation that would require the improvement of modelling glycolysis. However, the model describes the interaction between three compartments (cytosol, mitochondria and ER). For simplicity, we have not yet considered cellular compartmentalization for the calcium module. Hence, a possible next step would be to include cellular compartments in the model, defining different subdomains.

So far, our model focused on a single astrocyte, and we investigated the metabolic output concerning their role as neuronal metabolic supply [24]. Hence, a 3D coupled model of an astrocyte and a neuron could be a next meaningful expansion of our model. As discussed, lactate is fundamental for neurons.

However, neuronal metabolism differs from astrocytes since it is more based on the TCA cycle. The coupled model could be investigated by adding a neuronal morphology and calibrating the metabolic parameters with the literature [71]. The high computational cost of solving two complex morphologies is an arising challenge.

Last, our model is entirely deterministic, but stochasticity is an immanent property of biological processes. Including a stochastic component [48] in activating our reaction sites or in the coupled model with calcium would add a new realistic component to the model.

6.2.3 Biophysics

Astrocytes are very heterogeneous [210], as presented in Section 2.1. Thus, a first application of our framework could be to consider a broader spectrum of different types of astrocytes and investigate their metabolism and the impact of their different cellular morphology on metabolism.

In our investigation of the reaction site locations [99], we highlighted the central role of mitochondrial location [104, 137]. The potential development of our work would be to use machine learning techniques [235] to investigate reaction site locations and where they could be more efficient for metabolite production in astrocytic morphologies.

Furthermore, the investigation of reaction sites pointed to the fundamental role of mitochondria location for healthy, energetic cellular production. Mitochondrial dysfunction is a significant feature of Parkinson's disease (PD) [41]. Therefore, our studies could be applied to PD *via* a multiscale approach which can go from mitochondrial morphological level [105, 207] to the full astrocyte.

Last, we proposed to use our 3D model to investigate the metabolism of a healthy astrocyte and an AD one. In the future, we would like to address the challenge of a dynamic model that describes the morphological and molecular changes of the cell from a healthy to a reactive state. A spatiotemporal model describing the cellular changes from healthy to diseased would be a valid tool to investigate cellular degeneration *in silico*. However, this comes with many challenges. A stable numerical method is required to simulate morphologic changes over time, leading to high computational costs.

In conclusion, the work presented in this thesis demonstrated the efficiency of interdisciplinary research in addressing biological complexity. The computational approaches shown are promising for investigating diseases and help biologists test new hypotheses and unravel the mystery of the brain.

References

[1] Acosta, C., Anderson, H. D., and Anderson, C. M. (2017). Astrocyte dysfunction in alzheimer disease. *Journal of neuroscience research*, 95(12):2430–2447.

[2] Agapakis, C. M., Boyle, P. M., and Silver, P. A. (2012). Natural strategies for the spatial optimization of metabolism in synthetic biology. *Nature chemical biology*, 8(6):527–535.

[3] Agathos, K., Bordas, S. P., and Chatzi, E. (2019). Improving the conditioning of xfem/gfem for fracture mechanics problems through enrichment quasi-orthogonalization. *Computer Methods in Applied Mechanics and Engineering*, 346:1051–1073.

[4] Agathos, K., Chatzi, E., and Bordas, S. P. (2018). Multiple crack detection in 3d using a stable xfem and global optimization. *Computational mechanics*, 62(4):835–852.

[5] Agathos, K., Chatzi, E., Bordas, S. P., and Talaslidis, D. (2016). A well-conditioned and optimally convergent xfem for 3d linear elastic fracture. *International Journal for Numerical Methods in Engineering*, 105(9):643–677.

[6] Allaman, I., Gavillet, M., Bélanger, M., Laroche, T., Viertl, D., Lashuel, H. A., and Magistretti, P. J. (2010). Amyloid-β aggregates cause alterations of astrocytic metabolic phenotype: impact on neuronal viability. *Journal of Neuroscience*, 30(9):3326–3338.

[7] Allik, H. and Hughes, T. J. (1970). Finite element method for piezoelectric vibration. *International journal for numerical methods in engineering*, 2(2):151–157.

[8] Almeida, A., Almeida, J., Bolaños, J. P., and Moncada, S. (2001). Different responses of astrocytes and neurons to nitric oxide: the role of glycolytically

generated atp in astrocyte protection. *Proceedings of the National Academy of Sciences*, 98(26):15294–15299.

[9] Alnæs, M. S., Blechta, J., Hake, J., Johansson, A., Kehlet, B., Logg, A., Richardson, C., Ring, J., Rognes, M. E., and Wells, G. N. (2015). The fenics project version 1.5. *Archive of Numerical Software*, 3(100):9–23.

[10] Alnæs, M. S., Logg, A., Ølgaard, K. B., Rognes, M. E., and Wells, G. N. (2014). Unified form language: A domain-specific language for weak formulations of partial differential equations. *ACM Transactions on Mathematical Software (TOMS)*, 40(2):1–37.

[11] Anderson, M. A., Ao, Y., and Sofroniew, M. V. (2014). Heterogeneity of reactive astrocytes. *Neuroscience letters*, 565:23–29.

[12] Arndt, D., Bangerth, W., Clevenger, T. C., Davydov, D., Fehling, M., Garcia-Sanchez, D., Harper, G., Heister, T., Heltai, L., Kronbichler, M., Kynch, R. M., Maier, M., Pelteret, J.-P., Turcksin, B., and Wells, D. (2019). The `deal.II` library, version 9.1. *Journal of Numerical Mathematics*, 27(4):203–213.

[13] Arranz, A. M. and De Strooper, B. (2019). The role of astroglia in alzheimer's disease: pathophysiology and clinical implications. *The Lancet Neurology*.

[14] Atroshchenko, E., Tomar, S., Xu, G., and Bordas, S. P. (2018). Weakening the tight coupling between geometry and simulation in isogeometric analysis: From sub-and super-geometric analysis to geometry-independent field approximation (gift). *International Journal for Numerical Methods in Engineering*, 114(10):1131–1159.

[15] Aubert, A. and Costalat, R. (2005). Interaction between astrocytes and neurons studied using a mathematical model of compartmentalized energy metabolism. *Journal of Cerebral Blood Flow & Metabolism*, 25(11):1476–1490.

[16] Aubert, A., Costalat, R., Magistretti, P. J., and Pellerin, L. (2005). Brain lactate kinetics: modeling evidence for neuronal lactate uptake upon activation. *Proceedings of the National Academy of Sciences*, 102(45):16448–16453.

[17] Babuška, I. (1971). Error-bounds for finite element method. *Numerische Mathematik*, 16(4):322–333.

[18] Babuška, I. and Melenk, J. M. (1997). The partition of unity method. *International journal for numerical methods in engineering*, 40(4):727–758.

[19] Balay, S., Abhyankar, S., Adams, M. F., Brown, J., Brune, P., Buschelman, K., Dalcin, L., Dener, A., Eijkhout, V., Gropp, W. D., Karpeyev, D., Kaushik, D., Knepley, M. G., May, D. A., McInnes, L. C., Mills, R. T., Munson, T., Rupp, K., Sanan, P., Smith, B. F., Zampini, S., Zhang, H., and Zhang, H. (2019). PETSc users manual. Technical Report ANL-95/11 - Revision 3.12, Argonne National Laboratory.

[20] Banerjee, P. K., Banerjee, P. K., and Butterfield, R. (1981). *Boundary element methods in engineering science*. McGraw-Hill (UK).

[21] Bardehle, S., Krüger, M., Buggenthin, F., Schwausch, J., Ninkovic, J., Clevers, H., Snippert, H. J., Theis, F. J., Meyer-Luehmann, M., Bechmann, I., et al. (2013). Live imaging of astrocyte responses to acute injury reveals selective juxtavascular proliferation. *Nature neuroscience*, 16(5):580–586.

[22] Beard, D. A. (2005). A biophysical model of the mitochondrial respiratory system and oxidative phosphorylation. *PLoS computational biology*, 1(4):e36.

[23] Béchet, É., Minnebo, H., Moës, N., and Burgardt, B. (2005). Improved implementation and robustness study of the x-fem for stress analysis around cracks. *International journal for numerical methods in engineering*, 64(8):1033–1056.

[24] Bélanger, M., Allaman, I., and Magistretti, P. J. (2011). Brain energy metabolism: focus on astrocyte-neuron metabolic cooperation. *Cell metabolism*, 14(6):724–738.

[25] Bell, M., Bartol, T., Sejnowski, T., and Rangamani, P. (2019). Dendritic spine geometry and spine apparatus organization govern the spatiotemporal dynamics of calcium. *Journal of General Physiology*, 151(8):1017–1034.

[26] Belytschko, T. and Black, T. (1999). Elastic crack growth in finite elements with minimal remeshing. *International journal for numerical methods in engineering*, 45(5):601–620.

[27] Benito, J., Urena, F., and Gavete, L. (2001). Influence of several factors in the generalized finite difference method. *Applied Mathematical Modelling*, 25(12):1039–1053.

[28] Berndt, N., Bulik, S., and Holzhütter, H.-G. (2012). Kinetic modeling of the mitochondrial energy metabolism of neuronal cells: the impact of reduced-ketoglutarate dehydrogenase activities on atp production and generation of reactive oxygen species. *International journal of cell biology*, 2012.

[29] Berndt, N., Kann, O., and Holzhütter, H.-G. (2015). Physiology-based kinetic modeling of neuronal energy metabolism unravels the molecular basis of nad (p) h fluorescence transients. *Journal of Cerebral Blood Flow & Metabolism*, 35(9):1494–1506.

[30] Berridge, M. J., Bootman, M. D., and Lipp, P. (1998). Calcium-a life and death signal. *Nature*, 395(6703):645–648.

[31] Bertram, R., Pedersen, M. G., Luciani, D. S., and Sherman, A. (2006). A simplified model for mitochondrial atp production. *Journal of theoretical biology*, 243(4):575–586.

[32] Bevington, A., Mundy, K., Yates, A., Kanis, J., Russell, R., Taylor, D., Rajagopalan, B., and Radda, G. (1986). A study of intracellular orthophosphate concentration in human muscle and erythrocytes by 31p nuclear magnetic resonance spectroscopy and selective chemical assay. *Clinical Science*, 71(6):729–735.

[33] Bigl, M., Brückner, M., Arendt, T., Bigl, V., and Eschrich, K. (1999). Activities of key glycolytic enzymes in the brains of patients with alzheimer's disease. *Journal of neural transmission*, 106(5):499–511.

[34] Blonz, E. R. (2017). Alzheimer's disease as the product of a progressive energy deficiency syndrome in the central nervous system: the neuroenergetic hypothesis. *Journal of Alzheimer's Disease*, 60(4):1223–1229.

[35] Boiveau, T., Burman, E., Claus, S., and Larson, M. (2018). Fictitious domain method with boundary value correction using penalty-free nitsche method. *Journal of Numerical Mathematics*, 26(2):77–95.

[36] Booth, H. D., Hirst, W. D., and Wade-Martins, R. (2017). The role of astrocyte dysfunction in parkinson's disease pathogenesis. *Trends in neurosciences*, 40(6):358–370.

[37] Bordas, S., Bucki, M., Chouly, F., Duprez, M., Lleras, V., Lobos, C., Lozinski, A., Rohan, P.-Y., and Tomar, S. (2017). Quantifying discretization errors for soft-tissue simulation in computer assisted surgery: a preliminary study.

[38] Bordas, S. and Menk, A. (2014). *Xfem: The Extended Finite Element Method*. John Wiley.

[39] Bordas, S. and Moran, B. (2006). Enriched finite elements and level sets for damage tolerance assessment of complex structures. *Engineering Fracture Mechanics*, 73(9):1176–1201.

[40] Bordas, S., Nguyen, P. V., Dunant, C., Guidoum, A., and Nguyen-Dang, H. (2007). An extended finite element library. *International Journal for Numerical Methods in Engineering*, 71(6):703–732.

[41] Bose, A. and Beal, M. F. (2016). Mitochondrial dysfunction in parkinson's disease. *Journal of neurochemistry*, 139:216–231.

[42] Bouvier, D. S., Fixemer, S., Heurtaux, T., Jeannelle, F., Frauenknecht, K., and Mittelbronn, M. (2022). The multifaceted neurotoxicity of astrocytes in ageing and age-related neurodegenerative diseases: A translational perspective. *Frontiers in Physiology*, page 467.

[43] Bouvier, D. S., Jones, E. V., Quesseveur, G., Davoli, M. A., A Ferreira, T., Quirion, R., Mechawar, N., and Murai, K. K. (2016). High resolution dissection of reactive glial nets in alzheimer's disease. *Scientific reports*, 6(1):1–15.

[44] Braak, H. and Braak, E. (1996). Evolution of the neuropathology of alzheimer's disease. *Acta Neurologica Scandinavica*, 94(S165):3–12.

[45] Bradley, S. J. and Challiss, R. J. (2012). G protein-coupled receptor signalling in astrocytes in health and disease: a focus on metabotropic glutamate receptors. *Biochemical pharmacology*, 84(3):249–259.

[46] Brebbia, C. A. and Dominguez, J. (1994). *Boundary elements: an introductory course*. WIT press.

[47] Brenner, S. and Scott, R. (2008). *The Mathematical Theory of Finite Element Methods*. Texts in Applied Mathematics. Springer-Verlag, New York, 3 edition.

[48] Bressloff, P. C. (2014). *Stochastic processes in cell biology*, volume 41. Springer.

[49] Brookmeyer, R., Johnson, E., Ziegler-Graham, K., and Arrighi, H. M. (2007). Forecasting the global burden of alzheimer's disease. *Alzheimer's & dementia*, 3(3):186–191.

[50] Brown, A. M. and Ransom, B. R. (2007). Astrocyte glycogen and brain energy metabolism. *Glia*, 55(12):1263–1271.

[51] Brown, A. M., Tekkök, S. B., and Ransom, B. R. (2004). Energy transfer from astrocytes to axons: the role of cns glycogen. *Neurochemistry international*, 45(4):529–536.

[52] Buckler, K. and Vaughan-Jones, R. (1990). Application of a new ph-sensitive fluoroprobe (carboxy-snarf-1) for intracellular ph measurement in small, isolated cells. *Pflügers Archiv*, 417(2):234–239.

[53] Bui, H. P., Tomar, S., Courtecuisse, H., Audette, M., Cotin, S., and Bordas, S. P. (2018). Controlling the error on target motion through real-time mesh adaptation: Applications to deep brain stimulation. *International journal for numerical methods in biomedical engineering*, 34(5):e2958.

[54] Bui, H. P., Tomar, S., Courtecuisse, H., Cotin, S., and Bordas, S. P. (2017). Real-time error control for surgical simulation. *IEEE Transactions on Biomedical Engineering*, 65(3):596–607.

[55] Bulle, R., Barrera, O., Bordas, S., Chouly, F., and Hale, J. S. (2022). An a posteriori error estimator for the spectral fractional power of the laplacian. *arXiv preprint arXiv:2202.05810*.

[56] Bulle, R., Hale, J., Lozinski, A., Bordas, S., and Chouly, F. (2021). Hierarchical a posteriori error estimation of bank-weiser type in the fenics project.

[57] Burman, E. (2010). Ghost penalty. *Comptes Rendus Mathematique*, 348(21-22):1217–1220.

[58] Burman, E., Claus, S., Hansbo, P., Larson, M. G., and Massing, A. (2015). Cutfem: discretizing geometry and partial differential equations. *International Journal for Numerical Methods in Engineering*, 104(7):472–501.

[59] Bushong, E. A., Martone, M. E., and Ellisman, M. H. (2004). Maturation of astrocyte morphology and the establishment of astrocyte domains during postnatal hippocampal development. *International Journal of Developmental Neuroscience*, 22(2):73–86.

[60] Bushong, E. A., Martone, M. E., Jones, Y. Z., and Ellisman, M. H. (2002). Protoplasmic astrocytes in ca1 stratum radiatum occupy separate anatomical domains. *Journal of Neuroscience*, 22(1):183–192.

[61] Çakır, T., Alsan, S., Saybaşılı, H., Akın, A., and Ülgen, K. Ö. (2007). Reconstruction and flux analysis of coupling between metabolic pathways of astrocytes and neurons: application to cerebral hypoxia. *Theoretical Biology and Medical Modelling*, 4(1):48.

[62] Camandola, S. and Mattson, M. P. (2017). Brain metabolism in health, aging, and neurodegeneration. *The EMBO journal*, 36(11):1474–1492.

[63] Casey, J. R., Grinstein, S., and Orlowski, J. (2010). Sensors and regulators of intracellular ph. *Nature reviews Molecular cell biology*, 11(1):50–61.

[64] Céa, J. (1964). Approximation variationnelle des problèmes aux limites. In *Annales de l'institut Fourier*, volume 14, pages 345–444.

[65] Charles, A. C., Merrill, J. E., Dirksen, E. R., and Sandersont, M. J. (1991). Intercellular signaling in glial cells: calcium waves and oscillations in response to mechanical stimulation and glutamate. *Neuron*, 6(6):983–992.

[66] Christopherson, K. S., Ullian, E. M., Stokes, C. C., Mullowney, C. E., Hell, J. W., Agah, A., Lawler, J., Mosher, D. F., Bornstein, P., and Barres, B. A. (2005). Thrombospondins are astrocyte-secreted proteins that promote cns synaptogenesis. *Cell*, 120(3):421–433.

[67] Claus, S., Bigot, S., and Kerfriden, P. (2018). Cutfem method for stefan–signorini problems with application in pulsed laser ablation. *SIAM Journal on Scientific Computing*, 40(5):B1444–B1469.

[68] Claus, S. and Kerfriden, P. (2018). A stable and optimally convergent latin-cutfem algorithm for multiple unilateral contact problems. *International Journal for Numerical Methods in Engineering*, 113(6):938–966.

[69] Claus, S. and Kerfriden, P. (2019). A cutfem method for two-phase flow problems. *Computer Methods in Applied Mechanics and Engineering*, 348:185–206.

[70] Claus, S., Kerfriden, P., Moshfeghifar, F., Darkner, S., Erleben, K., and Wong, C. (2021). Contact modeling from images using cut finite element solvers. *Advanced Modeling and Simulation in Engineering Sciences*, 8(1):1–23.

[71] Cloutier, M., Bolger, F. B., Lowry, J. P., and Wellstead, P. (2009). An integrative dynamic model of brain energy metabolism using in vivo neurochemical measurements. *Journal of computational neuroscience*, 27(3):391.

[72] Cloutier, M. and Wellstead, P. (2012). Dynamic modelling of protein and oxidative metabolisms simulates the pathogenesis of parkinson's disease. *IET systems biology*, 6(3):65–72.

[73] Cortassa, S., Aon, M. A., Marbán, E., Winslow, R. L., and O'Rourke, B. (2003). An integrated model of cardiac mitochondrial energy metabolism and calcium dynamics. *Biophysical journal*, 84(4):2734–2755.

[74] Cotto, B., Natarajaseenivasan, K., and Langford, D. (2019). Astrocyte activation and altered metabolism in normal aging, age-related cns diseases, and hand. *Journal of neurovirology*, 25(5):722–733.

[75] Csordás, G. and Hajnóczky, G. (2009). Sr/er–mitochondrial local communication: calcium and ros. *Biochimica et Biophysica Acta (BBA)-Bioenergetics*, 1787(11):1352–1362.

[76] Cunningham, C., Dunne, A., and Lopez-Rodriguez, A. B. (2019). Astrocytes: heterogeneous and dynamic phenotypes in neurodegeneration and innate immunity. *The Neuroscientist*, 25(5):455–474.

[77] da Veiga Moreira, J., Hamraz, M., Abolhassani, M., Schwartz, L., Jolicœur, M., and Pérès, S. (2019). Metabolic therapies inhibit tumor growth in vivo and in silico. *Scientific reports*, 9(1):1–10.

[78] De Pittà, M., Goldberg, M., Volman, V., Berry, H., and Ben-Jacob, E. (2009). Glutamate regulation of calcium and ip3 oscillating and pulsating dynamics in astrocytes. *Journal of biological physics*, 35(4):383–411.

[79] De Young, G. W. and Keizer, J. (1992). A single-pool inositol 1, 4, 5-trisphosphate-receptor-based model for agonist-stimulated oscillations in ca2+ concentration. *Proceedings of the National Academy of Sciences*, 89(20):9895–9899.

[80] Devine, M. J. and Kittler, J. T. (2018). Mitochondria at the neuronal presynapse in health and disease. *Nature Reviews Neuroscience*, 19(2):63–80.

[81] Donoso, P., Mill, J., O'neill, S., and Eisner, D. (1992). Fluorescence measurements of cytoplasmic and mitochondrial sodium concentration in rat ventricular myocytes. *The Journal of physiology*, 448(1):493–509.

[82] Duddu, R., Bordas, S., Chopp, D., and Moran, B. (2008). A combined extended finite element and level set method for biofilm growth. *International Journal for Numerical Methods in Engineering*, 74(5):848–870.

[83] Duddu, R., Chopp, D. L., and Moran, B. (2009). A two-dimensional continuum model of biofilm growth incorporating fluid flow and shear stress based detachment. *Biotechnology and bioengineering*, 103(1):92–104.

[84] Dudycha, S. (2000). A detailed model of the tricarboxylic acid cycle in heart cells, master of science thesis. *Department of Biomedical Engineering*, page 141.

[85] Dunant, C. F. and Scrivener, K. L. (2010). Micro-mechanical modelling of alkali–silica-reaction-induced degradation using the amie framework. *Cement and Concrete research*, 40(4):517–525.

[86] Dupont, G. and Erneux, C. (1997). Simulations of the effects of inositol 1, 4, 5-trisphosphate 3-kinase and 5-phosphatase activities on ca2+ oscillations. *Cell calcium*, 22(5):321–331.

[87] Dupont, G., Falcke, M., Kirk, V., and Sneyd, J. (2016). *Models of calcium signalling*, volume 43. Springer.

[88] Duprez, M., Bordas, S., Bucki, M., Bui, H. P., Chouly, F., Lleras, V., Lobos, C., Lozinski, A., Rohan, P.-Y., and Tomar, S. (2018). Quantifying discretization errors for soft-tissue simulation in computer assisted surgery: a preliminary study. *arXiv preprint arXiv:1806.06944*.

[89] Duprez, M., Bordas, S. P. A., Bucki, M., Bui, H. P., Chouly, F., Lleras, V., Lobos, C., Lozinski, A., Rohan, P.-Y., and Tomar, S. (2020). Quantifying discretization errors for soft tissue simulation in computer assisted surgery: A preliminary study. *Applied Mathematical Modelling*, 77:709–723.

[90] Duprez, M. and Lozinski, A. (2020). ϕ-fem: a finite element method on domains defined by level-sets. *SIAM Journal on Numerical Analysis*, 58(2):1008–1028.

[91] Eilam, R., Segal, M., Malach, R., Sela, M., Arnon, R., and Aharoni, R. (2018). A strocyte disruption of neurovascular communication is linked to cortical damage in an animal model of multiple sclerosis. *Glia*, 66(5):1098–1117.

[92] Ellingsrud, A. J., Solbrå, A., Einevoll, G. T., Halnes, G., and Rognes, M. E. (2020). Finite element simulation of ionic electrodiffusion in cellular geometries. *Frontiers in Neuroinformatics*, 14:11.

[93] Endo, M. (1970). Tanaka m, and ogawa y. *Calcium induced release of calcium from the sarcoplasmic reticulum of skinned skeletal muscle fibres. Nature*, 228:34–36.

[94] Escartin, C., Galea, E., Lakatos, A., O'Callaghan, J. P., Petzold, G. C., Serrano-Pozo, A., Steinhäuser, C., Volterra, A., Carmignoto, G., Agarwal, A., et al. (2021). Reactive astrocyte nomenclature, definitions, and future directions. *Nature neuroscience*, 24(3):312–325.

[95] Eymard, R., Gallouët, T., and Herbin, R. (2000). Finite volume methods. *Handbook of numerical analysis*, 7:713–1018.

[96] Farina, S., Claus, S., Hale, J. S., Komin, N., Skupin, A., and Bordas, S. (2020). A cutfem method for a spatially resolved energy metabolism model in complex cellular geometries. WCCM.

[97] Farina, S., Claus, S., Hale, J. S., Skupin, A., and Bordas, S. (2021). A cut finite element method for spatially resolved energy metabolism models in complex neuro-cell morphologies with minimal remeshing. *Advanced Modeling and Simulation in Engineering Sciences*, 8(1):1–32.

[98] Farina, S., Voorsluijs, V., Fixemer, S., Bouvier, D., Claus, S., Bordas, S., and Skupin, A. (2022a). 3d modelling of a spatially resolved energy metabolism in physiological astrocytic morphology. ECMTB.

[99] Farina, S., Voorsluijs, V., Fixemer, S., Bouvier, D., Claus, S., Bordas, S., and Skupin, A. (2022b). Mechanistic multiscale modelling of energy metabolism in human astrocytes indicates morphological effects in alzheimer's disease. (Under review).

[100] Farina, S., Voorsluijs, V. e., Claus, S., Skupin, A., and Bordas, S. (2022c). A cutfem method for a mechanistic modeelling of astrocytic metabolsim in 3d physiological morphologies. ECCOMAS.

[101] Ferraiuolo, L., Higginbottom, A., Heath, P. R., Barber, S., Greenald, D., Kirby, J., and Shaw, P. J. (2011). Dysregulation of astrocyte–motoneuron cross-talk in mutant superoxide dismutase 1-related amyotrophic lateral sclerosis. *Brain*, 134(9):2627–2641.

[102] Fick, A. (1855). Ueber diffusion. *Annalen der Physik*, 170(1):59–86.

[103] Flamholz, A., Noor, E., Bar-Even, A., and Milo, R. (2012). equilibrator—the biochemical thermodynamics calculator. *Nucleic acids research*, 40(D1):D770–D775.

[104] Frazier, A. E., Kiu, C., Stojanovski, D., Hoogenraad, N. J., and Ryan, M. T. (2006). Mitochondrial morphology and distribution in mammalian cells.

[105] Garcia, G. C., Bartol, T. M., Phan, S., Bushong, E. A., Perkins, G., Sejnowski, T. J., Ellisman, M. H., and Skupin, A. (2019). Mitochondrial morphology provides a mechanism for energy buffering at synapses. *Scientific reports*, 9(1):1–12.

[106] Gordon, G. R., Mulligan, S. J., and MacVicar, B. A. (2007). Astrocyte control of the cerebrovasculature. *Glia*, 55(12):1214–1221.

[107] Granchi, C., Bertini, S., Macchia, M., and Minutolo, F. (2010). Inhibitors of lactate dehydrogenase isoforms and their therapeutic potentials. *Current medicinal chemistry*, 17(7):672–697.

[108] Gupta, V., Duarte, C. A., Babuška, I., and Banerjee, U. (2015). Stable gfem (sgfem): Improved conditioning and accuracy of gfem/xfem for three-dimensional fracture mechanics. *Computer methods in applied mechanics and engineering*, 289:355–386.

[109] Halassa, M. M., Fellin, T., Takano, H., Dong, J.-H., and Haydon, P. G. (2007). Synaptic islands defined by the territory of a single astrocyte. *Journal of Neuroscience*, 27(24):6473–6477.

[110] Hale, J. S., Brunetti, M., Bordas, S. P., and Maurini, C. (2018). Simple and extensible plate and shell finite element models through automatic code generation tools. *Computers & Structures*, 209:163–181.

[111] Hansbo, A. and Hansbo, P. (2002). An unfitted finite element method, based on nitsche's method, for elliptic interface problems. *Computer methods in applied mechanics and engineering*, 191(47-48):5537–5552.

[112] Haughey, N. J. and Mattson, M. P. (2003). Alzheimer's amyloid β-peptide enhances atp/gap junction-mediated calcium-wave propagation in astrocytes. *Neuromolecular medicine*, 3(3):173–180.

[113] Hauseux, P., Hale, J. S., Cotin, S., and Bordas, S. P. (2018). Quantifying the uncertainty in a hyperelastic soft tissue model with stochastic parameters. *Applied Mathematical Modelling*, 62:86–102.

[114] Hecht, F. (2012). New development in freefem++. *J. Numer. Math.*, 20(3-4):251–265.

[115] Hodgkin, A. L. and Huxley, A. F. (1952). A quantitative description of membrane current and its application to conduction and excitation in nerve. *The Journal of physiology*, 117(4):500–544.

[116] Hughes, T. J. (2012). *The finite element method: linear static and dynamic finite element analysis*. Courier Corporation.

[117] Hughes, T. J., Cottrell, J. A., and Bazilevs, Y. (2005). Isogeometric analysis: Cad, finite elements, nurbs, exact geometry and mesh refinement. *Computer methods in applied mechanics and engineering*, 194(39-41):4135–4195.

[118] Iadecola, C. and Nedergaard, M. (2007). Glial regulation of the cerebral microvasculature. *Nature neuroscience*, 10(11):1369–1376.

[119] Jackson, J. G. and Robinson, M. B. (2018). Regulation of mitochondrial dynamics in astrocytes: mechanisms, consequences, and unknowns. *Glia*, 66(6):1213–1234.

[120] Jansari, C., Kannan, K., Annabattula, R., Natarajan, S., et al. (2019). Adaptive phase field method for quasi-static brittle fracture using a recovery based error indicator and quadtree decomposition. *Engineering Fracture Mechanics*, 220:106599.

[121] John, S., Weiss, J. N., and Ribalet, B. (2011). Subcellular localization of hexokinases i and ii directs the metabolic fate of glucose. *PloS one*, 6(3):e17674.

[122] Johri, A. and Beal, M. F. (2012). Mitochondrial dysfunction in neurodegenerative diseases. *Journal of Pharmacology and Experimental Therapeutics*, 342(3):619–630.

[123] Jolivet, R., Magistretti, P. J., and Weber, B. (2009). Deciphering neuron-glia compartmentalization in cortical energy metabolism. *Frontiers in neuroenergetics*, 1:4.

[124] Keener, J. and Sneyd, J. (2009). *Mathematical physiology: II: Systems physiology*. Springer.

[125] Khalid, M. U., Tervonen, A., Korkka, I., Hyttinen, J., and Lenk, K. (2017). Geometry-based computational modeling of calcium signaling in an astrocyte. In Eskola, H., Väisänen, O., Viik, J., and Hyttinen, J., editors, *EMBEC & NBC 2017*, pages 157–160. Springer Singapore, Singapore.

[126] Kim, E.-Y., Chung, T.-W., Han, C. W., Park, S. Y., Park, K. H., Jang, S. B., and Ha, K.-T. (2019). A novel lactate dehydrogenase inhibitor, 1-(phenylseleno)-4-(trifluoromethyl) benzene, suppresses tumor growth through apoptotic cell death. *Scientific reports*, 9(1):1–12.

[127] Kirschner, M. W. (2005). The meaning of systems biology. *Cell*, 121(4):503–504.

[128] Kitano, H. (2002). Computational systems biology. *Nature*, 420(6912):206–210.

[129] Komin, N., Moein, M., Ellisman, M. H., and Skupin, A. (2015). Multiscale modeling indicates that temperature dependent [ca2+] i spiking in astrocytes is quantitatively consistent with modulated serca activity. *Neural plasticity*, 2015.

[130] Kurz, L. C., Shah, S., Frieden, C., Nakra, T., Stein, R. E., Drysdale, G. R., Evans, C. T., and Srere, P. A. (1995). Catalytic strategy of citrate synthase: subunit interactions revealed as a consequence of a single amino acid change in the oxaloacetate binding site. *Biochemistry*, 34(41):13278–13288.

[131] Laborde, P., Pommier, J., Renard, Y., and Salaün, M. (2005). High-order extended finite element method for cracked domains. *International Journal for Numerical Methods in Engineering*, 64(3):354–381.

[132] Laughlin, S. B., de Ruyter van Steveninck, R. R., and Anderson, J. C. (1998). The metabolic cost of neural information. *Nature neuroscience*, 1(1):36–41.

[133] Lee, J. M., Gianchandani, E. P., and Papin, J. A. (2006). Flux balance analysis in the era of metabolomics. *Briefings in bioinformatics*, 7(2):140–150.

[134] Li, Y.-X. and Rinzel, J. (1994). Equations for insp3 receptor-mediated [ca2+] i oscillations derived from a detailed kinetic model: a hodgkin-huxley like formalism. *Journal of theoretical Biology*, 166(4):461–473.

[135] Liddelow, S. A., Guttenplan, K. A., Clarke, L. E., Bennett, F. C., Bohlen, C. J., Schirmer, L., Bennett, M. L., Münch, A. E., Chung, W.-S., Peterson, T. C., et al. (2017). Neurotoxic reactive astrocytes are induced by activated microglia. *Nature*, 541(7638):481–487.

[136] Lin, M. T. and Beal, M. F. (2006). Mitochondrial dysfunction and oxidative stress in neurodegenerative diseases. *Nature*, 443(7113):787–795.

[137] Liu, Y. J., McIntyre, R. L., Janssens, G. E., and Houtkooper, R. H. (2020). Mitochondrial fission and fusion: A dynamic role in aging and potential target for age-related disease. *Mechanisms of ageing and development*, 186:111212.

[138] Logg, A., Mardal, K.-A., and Wells, G. (2012). *Automated solution of differential equations by the finite element method: The FEniCS book*. Springer Science & Business Media, Heidelberg.

[139] Lund, P. and Wiggins, D. (1987). The matrix water space of mitochondriain situ in isolated hepatocytes. *Bioscience reports*, 7(1):59–66.

[140] Lynch, R. M., Fogarty, K. E., and Fay, F. S. (1991). Modulation of hexokinase association with mitochondria analyzed with quantitative three-dimensional confocal microscopy. *The Journal of cell biology*, 112(3):385–395.

[141] Magistretti, P. and Pellerin, L. (1996). Cellular mechanisms of brain energy metabolism. relevance to functional brain imaging and to neurodegenerative disorders a. *Annals of the New York Academy of Sciences*, 777(1):380–387.

[142] Magistretti, P. J. and Allaman, I. (2018). Lactate in the brain: from metabolic end-product to signalling molecule. *Nature Reviews Neuroscience*, 19(4):235–249.

[143] Magnus, G. and Keizer, J. (1997). Minimal model of beta-cell mitochondrial ca2+ handling. *American Journal of Physiology-Cell Physiology*, 273(2):C717–C733.

[144] Magnus, G. and Keizer, J. (1998a). Model of β-cell mitochondrial calcium handling and electrical activity. i. cytoplasmic variables. *American Journal of Physiology-Cell Physiology*, 274(4):C1158–C1173.

[145] Magnus, G. and Keizer, J. (1998b). Model of β-cell mitochondrial calcium handling and electrical activity. i. cytoplasmic variables. *American Journal of Physiology-Cell Physiology*, 274(4):C1158–C1173.

[146] Marot, C., Pellerin, J., and Remacle, J.-F. (2019). One machine, one minute, three billion tetrahedra. *International Journal for Numerical Methods in Engineering*, 117(9):967–990.

[147] Martín-Jiménez, C. A., Salazar-Barreto, D., Barreto, G. E., and González, J. (2017). Genome-scale reconstruction of the human astrocyte metabolic network. *Frontiers in aging neuroscience*, 9:23.

[148] Matsuoka, Y. and Srere, P. A. (1973). Kinetic studies of citrate synthase from rat kidney and rat brain. *Journal of Biological Chemistry*, 248(23):8022–8030.

[149] Mattugini, N., Merl-Pham, J., Petrozziello, E., Schindler, L., Bernhagen, J., Hauck, S. M., and Götz, M. (2018). Influence of white matter injury on gray matter reactive gliosis upon stab wound in the adult murine cerebral cortex. *Glia*, 66(8):1644–1662.

[150] McCommis, K. S. and Finck, B. N. (2015). Mitochondrial pyruvate transport: a historical perspective and future research directions. *Biochemical journal*, 466(3):443–454.

[151] Melenk, J. M. and Babuška, I. (1996). The partition of unity finite element method: basic theory and applications. *Computer methods in applied mechanics and engineering*, 139(1-4):289–314.

[152] Menk, A. and Bordas, S. P. (2011). A robust preconditioning technique for the extended finite element method. *International Journal for Numerical Methods in Engineering*, 85(13):1609–1632.

[153] Michaelis, L. and Menten, M. L. (2007). *Die Kinetik der Invertinwirkung*. Universitätsbibliothek Johann Christian Senckenberg, -.

[154] Miyakawa, T., Shimoji, A., Kuramoto, R., and Higuchi, Y. (1982). The relationship between senile plaques and cerebral blood vessels in alzheimer's disease and senile dementia. *Virchows Archiv B*, 40(1):121–129.

[155] Moein, M. (2017). *Dissecting the crosstalk between intracellular calcium signalling and mitochondrial metabolism*. PhD thesis, University of Luxembourg, Luxembourg.

[156] Motori, E., Puyal, J., Toni, N., Ghanem, A., Angeloni, C., Malaguti, M., Cantelli-Forti, G., Berninger, B., Conzelmann, K.-K., Götz, M., et al. (2013). Inflammation-induced alteration of astrocyte mitochondrial dynamics requires autophagy for mitochondrial network maintenance. *Cell metabolism*, 18(6):844–859.

[157] Moumnassi, M., Belouettar, S., Béchet, É., Bordas, S. P., Quoirin, D., and Potier-Ferry, M. (2011). Finite element analysis on implicitly defined domains: An accurate representation based on arbitrary parametric surfaces. *Computer Methods in Applied Mechanics and Engineering*, 200(5-8):774–796.

[158] Moumnassi, M., Bordas, S. P. A., Figueredo, R., and Sansen, P. (2014). Analysis using higher-order xfem: implicit representation of geometrical features from a given parametric representation. *Mechanics & Industry*, 15(5):443–448.

[159] Mulica, P., Grünewald, A., and Pereira, S. L. (2021). Astrocyte-neuron metabolic crosstalk in neurodegeneration: A mitochondrial perspective. *Frontiers in Endocrinology*, 12.

[160] Murray, J. D. (2007). *Mathematical biology: I. An introduction*, volume 17. Springer Science & Business Media.

[161] Nagele, R. G., D'Andrea, M. R., Lee, H., Venkataraman, V., and Wang, H.-Y. (2003). Astrocytes accumulate aβ42 and give rise to astrocytic amyloid plaques in alzheimer disease brains. *Brain research*, 971(2):197–209.

[162] Nguyen, V. P., Rabczuk, T., Bordas, S., and Duflot, M. (2008). Meshless methods: a review and computer implementation aspects. *Mathematics and computers in simulation*, 79(3):763–813.

[163] Nichols, E., Szoeke, C. E., Vollset, S. E., Abbasi, N., Abd-Allah, F., Abdela, J., Aichour, M. T. E., Akinyemi, R. O., Alahdab, F., Asgedom, S. W., et al. (2019). Global, regional, and national burden of alzheimer's disease and other dementias, 1990–2016: a systematic analysis for the global burden of disease study 2016. *The Lancet Neurology*, 18(1):88–106.

[164] Nitsche, J. (1971). Über ein variationsprinzip zur lösung von dirichlet-problemen bei verwendung von teilräumen, die keinen randbedingungen unterworfen sind. In *Abhandlungen aus dem mathematischen Seminar der Universität Hamburg*, volume 36, pages 9–15. Springer.

[165] Oberheim, N. A., Takano, T., Han, X., He, W., Lin, J. H., Wang, F., Xu, Q., Wyatt, J. D., Pilcher, W., Ojemann, J. G., et al. (2009). Uniquely hominid features of adult human astrocytes. *Journal of Neuroscience*, 29(10):3276–3287.

[166] Ochoa Martínez, J. Á. (2020). Computacional analysis of intracellular calcium elevations related to morphology changes in astrocytes.

[167] Oksanen, M., Lehtonen, S., Jaronen, M., Goldsteins, G., Hämäläinen, R. H., and Koistinaho, J. (2019). Astrocyte alterations in neurodegenerative pathologies and their modeling in human induced pluripotent stem cell platforms. *Cellular and Molecular Life Sciences*, 76(14):2739–2760.

[168] Oliveira, J. M. (2010). Nature and cause of mitochondrial dysfunction in huntington's disease: focusing on huntingtin and the striatum. *Journal of neurochemistry*, 114(1):1–12.

[169] Oschmann, F., Berry, H., Obermayer, K., and Lenk, K. (2018). From in silico astrocyte cell models to neuron-astrocyte network models: A review. *Brain research bulletin*, 136:76–84.

[170] Osher, S. and Sethian, J. A. (1988). Fronts propagating with curvature-dependent speed: algorithms based on hamilton-jacobi formulations. *Journal of computational physics*, 79(1):12–49.

[171] Parri, H. and Crunelli, V. (2003). The role of ca2+ in the generation of spontaneous astrocytic ca2+ oscillations. *Neuroscience*, 120(4):979–992.

[172] Pathak, D., Berthet, A., and Nakamura, K. (2013). Energy failure: does it contribute to neurodegeneration? *Annals of neurology*, 74(4):506–516.

[173] Patrick, K. L., Bell, S. L., Weindel, C. G., and Watson, R. O. (2019). Exploring the "multiple-hit hypothesis" of neurodegenerative disease: bacterial infection comes up to bat. *Frontiers in Cellular and Infection Microbiology*, 9:138.

[174] Pekny, M. and Pekna, M. (2014). Astrocyte reactivity and reactive astrogliosis: costs and benefits. *Physiological reviews*, 94(4):1077–1098.

[175] Pellerin, L. and Magistretti, P. J. (1994). Glutamate uptake into astrocytes stimulates aerobic glycolysis: a mechanism coupling neuronal activity to glucose utilization. *Proceedings of the National Academy of Sciences*, 91(22):10625–10629.

[176] Perea, G. and Araque, A. (2005). Glial calcium signaling and neuron–glia communication. *Cell calcium*, 38(3-4):375–382.

[177] Perea, G., Navarrete, M., and Araque, A. (2009). Tripartite synapses: astrocytes process and control synaptic information. *Trends in neurosciences*, 32(8):421–431.

[178] Picone, P., Nuzzo, D., Caruana, L., Scafidi, V., and Di Carlo, M. (2014). Mitochondrial dysfunction: different routes to alzheimer's disease therapy. *Oxidative medicine and cellular longevity*, 2014.

[179] Pierre, M. (2010). Global existence in reaction-diffusion systems with control of mass: a survey. *Milan Journal of Mathematics*, 78(2):417–455.

[180] Pietrobon, D. and Caplan, S. R. (1985). Flow-force relationships for a six-state proton pump model: intrinsic uncoupling, kinetic equivalence of input and output forces, and domain of approximate linearity. *Biochemistry*, 24(21):5764–5776.

[181] Pihlaja, R., Koistinaho, J., Malm, T., Sikkilä, H., Vainio, S., and Koistinaho, M. (2008). Transplanted astrocytes internalize deposited β-amyloid peptides in a transgenic mouse model of alzheimer's disease. *Glia*, 56(2):154–163.

[182] Polson, A. (1950). The some aspects of diffusion in solution and a definition of a colloidal particle. *The Journal of Physical Chemistry*, 54(5):649–652.

[183] Pooler, A. M., Noble, W., and Hanger, D. P. (2014). A role for tau at the synapse in alzheimer's disease pathogenesis. *Neuropharmacology*, 76:1–8.

[184] Powell, E. M. and Geller, H. M. (1999). Dissection of astrocyte-mediated cues in neuronal guidance and process extension. *Glia*, 26(1):73–83.

[185] Quarteroni, A. and Valli, A. (2008). *Numerical approximation of partial differential equations*. Springer Science & Business Media, Heidelberg.

[186] Quesseveur, G., d'Hérouël, A. F., Murai, K. K., and Bouvier, D. S. (2019). A specialized method to resolve fine 3d features of astrocytes in nonhuman primate (marmoset, callithrix jacchus) and human fixed brain samples. In Benedetto, B. D., editor, *Astrocytes*, pages 85–95. Springer, Regensburg, Germany.

[187] Raman, K. and Chandra, N. (2009). Flux balance analysis of biological systems: applications and challenges. *Briefings in bioinformatics*, 10(4):435–449.

[188] Ramón y Cajal, S. (1928). Degeneration and regeneration of the nervous system.

[189] Rappel, H. and Beex, L. (2019). Estimating fibres' material parameter distributions from limited data with the help of bayesian inference. *European Journal of Mechanics-A/Solids*, 75:169–196.

[190] Rappel, H., Beex, L. A., and Bordas, S. P. (2018). Bayesian inference to identify parameters in viscoelasticity. *Mechanics of Time-Dependent Materials*, 22(2):221–258.

[191] Rappel, H., Beex, L. A., Hale, J. S., and Bordas, S. (2016). Bayesian inference for the stochastic identification of elastoplastic material parameters: introduction, misconceptions and insights. *arXiv preprint arXiv:1606.02422*.

[192] Rappel, H., Beex, L. A., Hale, J. S., Noels, L., and Bordas, S. (2019a). A tutorial on bayesian inference to identify material parameters in solid mechanics. *Archives of Computational Methods in Engineering*, pages 1–25.

[193] Rappel, H., Beex, L. A., Noels, L., and Bordas, S. (2019b). Identifying elastoplastic parameters with bayes' theorem considering output error, input error and model uncertainty. *Probabilistic Engineering Mechanics*, 55:28–41.

[194] Renard, Y. and Pommier, J. (2007). Getfem finite element library. *URL: http://home. gna. org/getfem*.

[195] Requicha, A. A. and Voelcker, H. B. (1977). Constructive solid geometry.

[196] Rizzuto, R., De Stefani, D., Raffaello, A., and Mammucari, C. (2012). Mitochondria as sensors and regulators of calcium signalling. *Nature reviews Molecular cell biology*, 13(9):566–578.

[197] Rose, J., Brian, C., Pappa, A., Panayiotidis, M. I., and Franco, R. (2020). Mitochondrial metabolism in astrocytes regulates brain bioenergetics, neurotransmission and redox balance. *Frontiers in neuroscience*, page 1155.

[198] Saks, V., Kuznetsov, A., Andrienko, T., Usson, Y., Appaix, F., Guerrero, K., Kaambre, T., Sikk, P., Lemba, M., and Vendelin, M. (2003). Heterogeneity of adp diffusion and regulation of respiration in cardiac cells. *Biophysical Journal*, 84(5):3436–3456.

[199] Salamanca, L., Mechawar, N., Murai, K. K., Balling, R., Bouvier, D. S., and Skupin, A. (2019). Mic-mac: An automated pipeline for high-throughput characterization and classification of three-dimensional microglia morphologies in mouse and human postmortem brain samples. *Glia*, 67(8):1496–1509.

[200] Salsa, S. (2016). *Partial differential equations in action: from modelling to theory*. Springer.

[201] Sánchez-Alvarez, R., Tabernero, A., and Medina, J. M. (2004). Endothelin-1 stimulates the translocation and upregulation of both glucose transporter and hexokinase in astrocytes: relationship with gap junctional communication. *Journal of neurochemistry*, 89(3):703–714.

[202] Savtchenko, L. P., Bard, L., Jensen, T. P., Reynolds, J. P., Kraev, I., Medvedev, N., Stewart, M. G., Henneberger, C., and Rusakov, D. A. (2018). Disentangling astroglial physiology with a realistic cell model in silico. *Nature communications*, 9(1):1–15.

[203] Schurr, A., West, C. A., and Rigor, B. M. (1988). Lactate-supported synaptic function in the rat hippocampal slice preparation. *Science*, 240(4857):1326–1328.

[204] Scofano, H., Vieyra, A., and De Meis, L. (1979). Substrate regulation of the sarcoplasmic reticulum atpase. transient kinetic studies. *Journal of Biological Chemistry*, 254(20):10227–10231.

[205] Sertbaş, M., Ülgen, K., and Çakır, T. (2014). Systematic analysis of transcription-level effects of neurodegenerative diseases on human brain metabolism by a newly reconstructed brain-specific metabolic network. *FEBS open bio*, 4(1):542–553.

[206] Sethian, J. A. (1999). *Level set methods and fast marching methods: evolving interfaces in computational geometry, fluid mechanics, computer vision, and materials science*. Cambridge university press, Cambridge.

[207] Siegmund, S. E., Grassucci, R., Carter, S. D., Barca, E., Farino, Z. J., Juanola-Falgarona, M., Zhang, P., Tanji, K., Hirano, M., Schon, E. A., et al. (2018). Three-dimensional analysis of mitochondrial crista ultrastructure in a patient with leigh syndrome by in situ cryoelectron tomography. *Iscience*, 6:83–91.

[208] Siess, E., Brocks, D., and Wieland, O. (1976). Subcellular distribution of key metabolites in isolated liver cells from fasted rats. *Febs Letters*, 69(1-2):265–271.

[209] Smith, G. D., Smith, G. D., and Smith, G. D. S. (1985). *Numerical solution of partial differential equations: finite difference methods*. Oxford university press.

[210] Sofroniew, M. V. and Vinters, H. V. (2010). Astrocytes: biology and pathology. *Acta neuropathologica*, 119(1):7–35.

[211] Soman, S., Keatinge, M., Moein, M., Da Costa, M., Mortiboys, H., Skupin, A., Sugunan, S., Bazala, M., Kuznicki, J., and Bandmann, O. (2017). Inhibition of the mitochondrial calcium uniporter rescues dopaminergic neurons in pink1-/- zebrafish. *European Journal of Neuroscience*, 45(4):528–535.

[212] Stein, W. D. and Litman, T. (2014). *Channels, carriers, and pumps: an introduction to membrane transport*. Elsevier.

[213] Stichel, C. C. and Müller, H. W. (1998). The cns lesion scar: new vistas on an old regeneration barrier. *Cell and tissue research*, 294(1):1–9.

[214] Strouboulis, T., Babuška, I., and Copps, K. (2000). The design and analysis of the generalized finite element method. *Computer methods in applied mechanics and engineering*, 181(1-3):43–69.

[215] Strouboulis, T., Copps, K., and Babuška, I. (2001). The generalized finite element method. *Computer methods in applied mechanics and engineering*, 190(32-33):4081–4193.

[216] Swartz, B. and Wendroff, B. (1969). Generalized finite-difference schemes. *Mathematics of Computation*, 23(105):37–49.

[217] Tantama, M., Martínez-François, J. R., Mongeon, R., and Yellen, G. (2013). Imaging energy status in live cells with a fluorescent biosensor of the intracellular atp-to-adp ratio. *Nature communications*, 4(1):1–11.

[218] Tantama, M. and Yellen, G. (2014). Imaging changes in the cytosolic atp-to-adp ratio. In *Methods in enzymology*, volume 547, pages 355–371. Elsevier.

[219] Turing, A. M. (1990). The chemical basis of morphogenesis. *Bulletin of mathematical biology*, 52(1):153–197.

[220] Turner, D. A. and Adamson, D. C. (2011). Neuronal-astrocyte metabolic interactions: understanding the transition into abnormal astrocytoma metabolism. *Journal of Neuropathology & Experimental Neurology*, 70(3):167–176.

[221] Tyn, M. T. and Gusek, T. W. (1990). Prediction of diffusion coefficients of proteins. *Biotechnology and bioengineering*, 35(4):327–338.

[222] Verisokin, A. Y., Verveyko, D. V., Postnov, D. E., and Brazhe, A. R. (2021). Modeling of astrocyte networks: toward realistic topology and dynamics. *Frontiers in cellular neuroscience*, 15:645068.

[223] Vinters, H. V. (1987). Cerebral amyloid angiopathy. a critical review. *Stroke*, 18(2):311–324.

[224] Von Bartheld, C. S., Bahney, J., and Herculano-Houzel, S. (2016). The search for true numbers of neurons and glial cells in the human brain: A review of 150 years of cell counting. *Journal of Comparative Neurology*, 524(18):3865–3895.

[225] Voorsluijs, V., Avanzini, F., Falasco, G., Esposito, M., and Skupin, A. (2022). Nonequilibrium calcium signaling optimises the energetic efficiency of mitochondrial metabolism. (Under review).

[226] Waage, P. and Gulberg, C. M. (1986). Studies concerning affinity. *Journal of chemical education*, 63(12):1044.

[227] Wacquier, B., Combettes, L., Van Nhieu, G. T., and Dupont, G. (2016). Interplay between intracellular ca2+ oscillations and ca2+-stimulated mitochondrial metabolism. *Scientific reports*, 6(1):1–16.

[228] Walz, W. (2000). Role of astrocytes in the clearance of excess extracellular potassium. *Neurochemistry international*, 36(4-5):291–300.

[229] Wei, A.-C., Aon, M. A., O'Rourke, B., Winslow, R. L., and Cortassa, S. (2011). Mitochondrial energetics, ph regulation, and ion dynamics: a computational-experimental approach. *Biophysical journal*, 100(12):2894–2903.

[230] Wiemerslage, L. and Lee, D. (2016). Quantification of mitochondrial morphology in neurites of dopaminergic neurons using multiple parameters. *Journal of neuroscience methods*, 262:56–65.

[231] Wu, F., Yang, F., Vinnakota, K. C., and Beard, D. A. (2007). Computer modeling of mitochondrial tricarboxylic acid cycle, oxidative phosphorylation, metabolite transport, and electrophysiology. *Journal of Biological Chemistry*, 282(34):24525–24537.

[232] Wu, Z., Yin, J., and Wang, C. (2006). *Elliptic & parabolic equations*. World Scientific.

[233] Yamanaka, K., Chun, S. J., Boillee, S., Fujimori-Tonou, N., Yamashita, H., Gutmann, D. H., Takahashi, R., Misawa, H., and Cleveland, D. W. (2008). Astrocytes as determinants of disease progression in inherited amyotrophic lateral sclerosis. *Nature neuroscience*, 11(3):251–253.

[234] Yasemi, M. and Jolicoeur, M. (2021). Modelling cell metabolism: a review on constraint-based steady-state and kinetic approaches. *Processes*, 9(2):322.

[235] Zhou, Z.-H. (2021). *Machine learning*. Springer Nature.

[236] Zhu, X., Lee, H.-g., Perry, G., and Smith, M. A. (2007). Alzheimer disease, the two-hit hypothesis: an update. *Biochimica et Biophysica Acta (BBA)-Molecular Basis of Disease*, 1772(4):494–502.

[237] Zlokovic, B. V. (2008). The blood-brain barrier in health and chronic neurodegenerative disorders. *Neuron*, 57(2):178–201.

[238] Zulfiqar, S., Garg, P., and Nieweg, K. (2019). Contribution of astrocytes to metabolic dysfunction in the alzheimer's disease brain. *Biological chemistry*, 400(9):1113–1127.

APPENDIX A

Supplementary Information 1

A.1 Asymptotic Solution

The system of ordinary differential equations is obtained applying the law of mass action to Equations (4.1)-(4.5). To avoid misinterpretation, we denote the concentration $A = [\text{GLC}]$, $B = [\text{ATP}]$, $C = [\text{ADP}]$, $D = [\text{GLY}]$, $E = [\text{PYR}]$, $F = [\text{LAC}]$ and we obtain the system

$$\begin{cases} \frac{dA}{dt} = -K_{HXK}AB^2 \\ \frac{dB}{dt} = -2K_{HXK}AB^2 + 2K_{PYRK}C^2D + 28K_{Mito}E - K_{act}B \\ \frac{dC}{dt} = 2K_{HXK}AB^2 - 2K_{PYRK}C^2D + K_{act}B \\ \frac{dD}{dt} = 2K_{HXK}AB^2 - K_{PYRK}C^2D \\ \frac{dE}{dt} = K_{PYRK}C^2D - K_{LDH}E - K_{Mito}E \\ \frac{dF}{dt} = K_{LDH}E \end{cases} \tag{A.1}$$

The initial condition for Equation(A.1) are chosen using the solution of the PDEs system Equation (4.6). We compute the integral over the domain Ω

using Equation (3.18) of the solutions of the PDEs when the source term ends, making stable the total amount of concentrations inside the domain

$$\begin{cases} A(t=0) = \int_\Omega [GLC](t=1)\mathrm{d}x := A_0 \\ B(t=0) = \int_\Omega [ATP](t=1)\mathrm{d}x := B_0 \\ C(t=0) = \int_\Omega [ADP](t=1)\mathrm{d}x := C_0 \\ D(t=0) = \int_\Omega [GLY](t=1)\mathrm{d}x := D_0 \\ E(t=0) = \int_\Omega [PYR](t=1)\mathrm{d}x := E_0 \\ F(t=0) = \int_\Omega [LAC](t=1)\mathrm{d}x := F_0 \end{cases} \tag{A.2}$$

Considering abundance of ATP and ADP inside the domain, this lead to only a possible system of steady state solution, that is when all the GLC is consumed by reaction HXK Equation (4.1), GLY is consumed by reaction PYRK Equation (4.2) and ATP is fully transformed into ADP from Equation (4.5):

$$\begin{cases} A_\infty = 0 \\ B_\infty = 0 \\ C_\infty = C_0 + B_0 + 28(E_0 + D_0 + 2A_0)\alpha \\ D_\infty = 0 \\ E_\infty = 0 \\ F_\infty = F_0 + (E_0 + 2A_0 + D_0)(1-\alpha) \end{cases} \tag{A.3}$$

In the solutions we have introduced a parameter $\alpha \in [0,1]$ which take into account the fact that the concentration of PYR is transformed not in equal part to LAC and ATP from the reaction LDH Equation (4.3) and reaction Mito Equation (4.4).

APPENDIX B

Supplementary Information 2

B.1 Spatial Arrangements for 2D Simulations in Rectangular Shape

In the rectangular domain we set up our simulation with ten reaction sites per reaction type. We define the entrance of GLC at the origin, the bottom left corner and the exits of LAC on the opposite vertex $(4, 140)\,\mu$m. The subregions of entrance and exits have been defined as the intersection of the rectangle and the circle with center the origin or the top right corner and radius $1.0\,\mu$m.

We present in Supplementary Table B.1, the different distributions used to define the x and y coordinates of the enzyme arrangements inside the 2D rectangle ($[0, l_1] \times [0, l_2]$). As presented in the main text, each setting has 10 reaction sites per reaction type. The uniform cells have all their sites sorted from a uniform distribution, noted $\mathcal{U}[a, b]$ covering the whole rectangular domain.

In polarised cells, we assumed the enzymes to be distributed according to normal distribution ($\mathcal{N}(m, \sigma')$, where m and σ' are the mean and standard deviation, respectively) or log-normal ($\log \mathcal{N}(m, \sigma')$) distributions. Close to the

	Reaction site distributions					
	Uniform		Polarised		Polarised $\log\mathcal{N}(2)$	
	x	y	x	y	x	y
HXK	$\mathcal{U}_{[0,l_1]}$	$\mathcal{U}_{[0,l_2]}$	$\mathcal{N}(\frac{l_1}{2},2)$	$\mathcal{N}(10,5)$	$\mathcal{N}(\frac{l_1}{2},2)$	$\mathcal{N}(10,5)$
PYRK	$\mathcal{U}_{[0,l_1]}$	$\mathcal{U}_{[0,l_2]}$	$\mathcal{N}(\frac{l_1}{2},2)$	$\mathcal{N}(10,5)$	$\mathcal{N}(\frac{l_1}{2},2)$	$\mathcal{N}(10,5)$
LDH	$\mathcal{U}_{[0,l_1]}$	$\mathcal{U}_{[0,l_2]}$	$\mathcal{N}(\frac{l_1}{2},2)$	$\mathcal{N}(l_2-10,5)$	$\mathcal{N}(\frac{l_1}{2},2)$	$\mathcal{N}(l_2-10,5)$
Mito	$\mathcal{U}_{[0,l_1]}$	$\mathcal{U}_{[0,l_2]}$	$\mathcal{N}(\frac{l_1}{2},2)$	$\mathcal{N}(10,5)$ or $\mathcal{U}[60,l_2]^*$	$\mathcal{N}(\frac{l_1}{2},2)$	$\log\mathcal{N}(2,2)$

Table B.1 The table shows the distributions chosen for x and y coordinates for each metabolites for the simulations in the 2D rectangle for the Uniform, Polarised and Polarised $\log\mathcal{N}(2)$ cells. * indicates that we sorted the Mito sites from two distributions: six from the normal and four from the uniform. In this way, we ensure the probability of having four Mito sites on the top of the rectangle.

GLC influx we place HXK and PYRK reactions, using $\mathcal{N}(\frac{l_1}{2},2)$ and $\mathcal{N}(10,5)$ to select the x and y coordinates, respectively. The ten enzymes of LDH are located close to the LAC efflux with $(x,y)\in(\mathcal{N}(\frac{l_1}{2},2)),\mathcal{N}(l_2-10,5)$. For the ten mitochondria, we select the x coordinate as for the other reaction sites with a normal distribution $\mathcal{N}(\frac{l_1}{2},2)$. For polarized cells, one option consists in locating six reacting sites with y selected from a normal law $\mathcal{N}(10,5)$ and distributing the remaining four uniformly within the top part of the cell ($y>60$). We refer to this setting as the "Polarised" one. We also consider a different sampling where mitochondrial locations are distributed according to a log-normal law $\log\mathcal{N}(2.,2)$. We call this setting "Polarised $\log\mathcal{N}(2)$".

Typical polarised configurations are although lacking mitochondria in the middle part of the cell as shown in the corresponding figure of the main text.

B.2 Significance Test for 2D Realisation

We run 200 realisations for each of these configurations (*i.e.* uniform, polarised and polarised $\log\mathcal{N}(2)$ for the purpose of statistical testing. In order to find out if the three types of spatial arrangements lead to statistically significant differences in the realisations, we perform a multiple comparison Holm-Bonferroni method since we consider simultaneously the distribution of the different concentrations. The Bonferroni method is applied to a parametric independent T-test to evaluate if there is a significant distance between the means of the concentrations of the three configurations and to a non-parametric

Wilcoxon-Mann-Whitney test to verify if two statistical samples come from the same population. The results of the significance tests were presented in Table 2. When the $p-$value is smaller than 0.05 then the hypothesis of the tests is rejected, meaning that our samples describe different populations, which is mainly the case.

The p-value results show that only GLY for the uniform and polarised cell, and PYR for the two polarised configurations are not significantly impacted by the spatial arrangements where GLY exhibits a high $p-$value only in the t-test but not in the non-parametric one. This finding is consistent with the similar average of the steady state concentration but the distinct underlying distribution (Fig. 4.3 **c**). For PYR, the distributions for the two polarised cells exhibit a similar range (Fig. 4.3 **c**) but since the two polarised cells only differ by the distribution of mitochondria it is expected that the distribution of PYR is similar, since it is produced in PYRK reaction.

B.3 Spatial Arrangement for 3D Simulations

We present in detail the settings of the simulation shown in Figs. 4.6 **a**-**c**. For the control, C, and the reactive, R, LDH and PYRK sites were sorted by a uniform distribution defined in the boxes that contains the two astrocytes, see Fig. B.1. While HXK sites were sorted from a normal distribution centered in each Mito site and with variance $0.03 \times L$ where L is a dimensionless parameter (see belowB.5). In particular, $1.38\,\mu$m for the control and $2.75\,\mu$m for R.

The polarised settings were arranged colocalising HXK and PYRK enzymes from a uniform distribution that cover the endfeet of the astrocyte ($\mathcal{U}_{[0,l_x]\times[y_1,l_y]\times[0,l_z]}$, where l_x, l_y, l_z are the dimensions of the box that contains the control astrocyte). LDH were sorted from the opposite side of the box containing the LAC export sub-regions of the astrocyte from another uniform distribution $\mathcal{U}_{[0,l_x]\times[0.,y_2]\times[0,l_z]}$. While the Mito were sorted from a log-normal distribution $\log\mathcal{N}(l_x, 0.64, l_z, 0.2)$ in the manner that colocalise HXK and PYRK.

Last, the three sub-regions chosen for the GLC entrance and the four LAC exits were selected manually and they are defined as the intersection of the cellular morphology with a sphere with a radius of $1.0\,\mu$m.

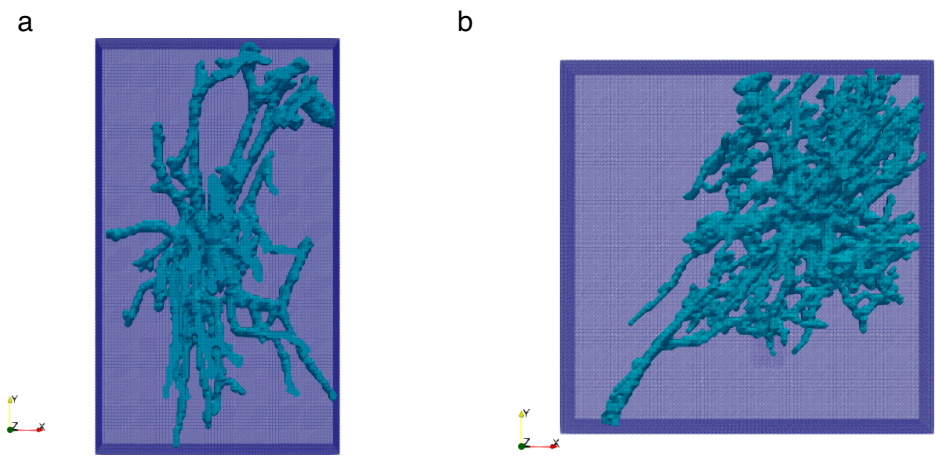

Fig. B.1 **Astrocytic morphologies embedded into a finite element background mesh. a** control and **b** reactive AD astrocytes are implicitly defined using a level set function and embedded in a structured background mesh. This is how we separated the finite element mesh from the geometries of the objects. Moreover, we used the dimensions of the background meshes to define the bounds of the uniform distributions to sort some of the reaction site centers.

B.4 Additional Figure for AD Simulations

We present in Supplementary Fig. B.2 an extension of Figure 4.7, where we show the trajectories of the average concentrations of the metabolites. This plot highlights the behaviour of the system in response to different AD related conditions.The systems reach the steady state in ≈ 50(s).

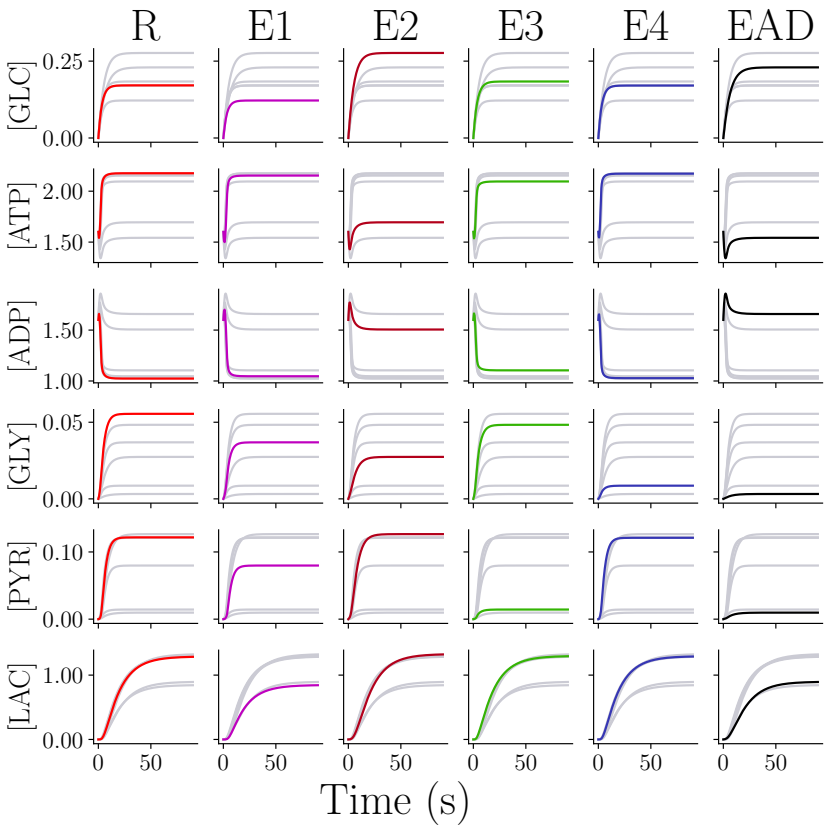

Fig. B.2 **Effects of AD conditions on metabolite dynamics in 3D reactive astrocyte.** Dynamics of the average concentration of each metabolites the simulations are solved inside the reactive astrocyte in AD with the setting presented in Figure 6 **c** of the main manuscript. R is the solution obtained with healthy parameters presented in Table 1 (red). E1 describes the deficiency of GLC uptake (magenta); E2, the mitochondria dysfunction (dark red); E3, the LDH overwork (green); E4, PYRK overwork (blue) and EAD, the four conditions combined (black).

B.5 Dimensionless System

To obtain the dimensionless system from the RDS Eq. 6, we impose $[\bar{\text{GLC}}] = \frac{[\text{GLC}]}{\alpha}, [\bar{\text{ATP}}] = \frac{[\text{ATP}]}{A_{tot}}, [\bar{\text{ADP}}] = \frac{[\text{ADP}]}{A_{tot}}, [\bar{\text{GLY}}] = \frac{[\text{GLY}]}{\alpha}, [\bar{\text{PYR}}] = \frac{[\text{PYR}]}{\alpha}, [\bar{\text{LAC}}] = \frac{[\text{LAC}]}{\alpha}$, where A_{tot} is the total amount of ATP and ADP inside the cell and α a constant that we set to 0.16. The spatial dimensionless is $\bar{x} = \frac{x}{L}$ $\bar{y} = \frac{y}{L}$ and

$\bar{z} = \frac{z}{L}$ where L is a parameter based on the volume of the astrocyte:

$$L = \frac{V}{V_\Omega}$$

where V is the real volume of the astrocyte segmented and V_Ω is the volume of the astrocyte in the dimensionless box with fixed x size of 1.0. We also define the dimensionless time parameter as $\bar{t} = \frac{t}{t_c}$ and we choose $t_c = \frac{L^2}{D_{\mathrm{GLC}}}$. So, we have that the dimensionless system is:

$$\begin{cases}
\frac{\partial[\mathrm{G\bar{L}C}]}{\partial\bar{t}} = & \nabla^2[\mathrm{G\bar{L}C}] - \mathcal{K}_{\mathrm{HXK}}\beta_{[\mathrm{G\bar{L}C}]}[\mathrm{G\bar{L}C}][\mathrm{A\bar{T}P}]^2 + \delta_{[\mathrm{G\bar{L}C}]}J_{\mathrm{in}} \\
\frac{\partial[\mathrm{A\bar{T}P}]}{\partial\bar{t}} = & \frac{D_{[\mathrm{ATP}]}}{D_{[\mathrm{GLC}]}}\nabla^2[\mathrm{A\bar{T}P}] - 2\mathcal{K}_{\mathrm{HXK}}\beta_{[\mathrm{A\bar{T}P}]}[\mathrm{G\bar{L}C}][\mathrm{A\bar{T}P}]^2 + \\
& +2\mathcal{K}_{\mathrm{PYRK}}\gamma_{[\mathrm{A\bar{T}P}]}[\mathrm{A\bar{D}P}]^2[\mathrm{G\bar{L}Y}] \\
& +28\mathcal{K}_{\mathrm{Mito}}\xi_{[\mathrm{A\bar{T}P}]}[\mathrm{P\bar{Y}R}][\mathrm{A\bar{D}P}]^{28} - \mathcal{K}_{\mathrm{act}}\tau_{[\mathrm{A\bar{T}P}]}[\mathrm{A\bar{T}P}] \\
\frac{\partial[\mathrm{A\bar{D}P}]}{\partial\bar{t}} = & \frac{D_{[\mathrm{ADP}]}}{D_{[\mathrm{GLC}]}}\nabla^2[\mathrm{A\bar{D}P}] + 2\mathcal{K}_{\mathrm{HXK}}\beta_{[\mathrm{A\bar{D}P}]}[\mathrm{G\bar{L}C}][\mathrm{A\bar{T}P}]^2 + \\
& -2\mathcal{K}_{\mathrm{PYRK}}\gamma_{[\mathrm{A\bar{T}P}]}[\mathrm{A\bar{D}P}]^2[\mathrm{G\bar{L}Y}] \\
& +\mathcal{K}_{Act}\tau_{[\mathrm{A\bar{D}P}]}[\mathrm{A\bar{T}P}] - 28\mathcal{K}_{\mathrm{Mito}}\xi_{[\mathrm{A\bar{D}P}]}[\mathrm{P\bar{Y}R}][\mathrm{A\bar{D}P}]^{28} \\
\frac{\partial[\mathrm{G\bar{L}Y}]}{\partial\bar{t}} = & \frac{D_{[\mathrm{GLY}]}}{D_{[\mathrm{GLC}]}}\nabla^2[\mathrm{G\bar{L}Y}] + 2\mathcal{K}_{\mathrm{HXK}}\beta_{[\mathrm{G\bar{L}Y}]}[\mathrm{G\bar{L}C}][\mathrm{A\bar{T}P}]^2 + \\
& -\mathcal{K}_{\mathrm{PYRK}}\gamma_{[\mathrm{A\bar{T}P}]}[\mathrm{A\bar{D}P}]^2[\mathrm{G\bar{L}Y}] \\
\frac{\partial[\mathrm{P\bar{Y}R}]}{\partial\bar{t}} = & \frac{D_{[\mathrm{PYR}]}}{D_{[\mathrm{GLC}]}}\nabla^2[\mathrm{P\bar{Y}R}] + \mathcal{K}_{\mathrm{PYRK}}\gamma_{[\mathrm{A\bar{T}P}]}[\mathrm{A\bar{D}P}]^2[\mathrm{G\bar{L}Y}] + \\
& -\mathcal{K}_{\mathrm{LDH}}\mu_{[\mathrm{P\bar{Y}R}]}[\mathrm{P\bar{Y}R}] - \mathcal{K}_{\mathrm{Mito}}\xi_{[\mathrm{P\bar{Y}R}]}[\mathrm{P\bar{Y}R}][\mathrm{A\bar{D}P}]^{28} \\
\frac{\partial[\mathrm{L\bar{A}C}]}{\partial\bar{t}} = & \frac{D_{[\mathrm{LAC}]}}{D_{[\mathrm{GLC}]}}\nabla^2[\mathrm{L\bar{A}C}] + \mathcal{K}_{\mathrm{LDH}}\mu_{[\mathrm{L\bar{A}C}]}[\mathrm{P\bar{Y}R}] - \eta_{[\mathrm{L\bar{A}C}]}[\mathrm{L\bar{A}C}]
\end{cases} \tag{B.1}$$

where the dimensionless coefficients are shown in the Table B.2:

Dimensionless coefficients					
HXK	PYRK	LDH	Mito	act	
$\beta_{[\bar{\text{GLC}}]} = t_c A_{\text{tot}}^2$					$\delta_{[\bar{\text{GLC}}]} = \frac{t_c}{\alpha}$
$\beta_{[\bar{\text{ATP}}]} = t_c \alpha A_{\text{tot}}$	$\gamma_{[\bar{\text{ATP}}]} = A_{\text{tot}} \alpha t_c$		$\xi_{[\bar{\text{ATP}}]} = t_c \alpha A_{\text{tot}}^{27}$	$\tau_{[\bar{\text{ATP}}]} = t_c$	
$\beta_{[\bar{\text{ADP}}]} = t_c \alpha A_{\text{tot}}$	$\gamma_{[\bar{\text{ADP}}]} = A_{\text{tot}} \alpha t_c$		$\xi_{[\bar{\text{ADP}}]} = t_c \alpha A_{\text{tot}}^{27}$	$\tau_{[\bar{\text{ATP}}]} = t_c$	
$\beta_{[\bar{\text{GLY}}]} = t_c A_{\text{tot}}^2$	$\gamma_{[\bar{\text{GLY}}]} = A_{\text{tot}}^2 t_c$				
	$\gamma_{[\bar{\text{PYR}}]} = A_{\text{tot}}^2 t_c$	$\mu_{[\bar{\text{PYR}}]} = t_c$	$\xi_{[\bar{\text{PYR}}]} = t_c A_{\text{tot}}^{28}$		
		$\mu_{[\bar{\text{LAC}}]} = t_c$			$\eta_{[\bar{\text{LAC}}]} = \eta t_c$

Table B.2 The table present the dimensionless coefficients for the dimensionless system B.1.

In this way, we define a dimensionless system that depends only on the dimensionless volume of the cell.

B.6 Detail on Numerical Methods for 2D Simulations

The 2D experiments were solved using standard finite element method (FEM) implemented in Python with the open source finite element solver DOLFIN from FEniCS [138, 9]. The domains are explicitly meshed using the package *mshr*, which generate a finite element mesh that conforms to the boundary of the domains. The solution of the weak problem is defined on the space of piece wise Lagrange finite elements of degree one. We solve the non-linear equation using a Newton-Raphson scheme, where the Jacobian is calculated automatically by the automatic differentation capabilities of UFL [10]. The linear system at each time step of the Newton-Raphson algorithm is solved using standard linear solvers from the *PETSc* library. For further details [97].

B.7 Details on Numerical Methods for 3D Simulations

To solve the system on the 3D astrocytic domains, we use a cut finite element [58] approach able to deal with the complexity of the cellular geometry, as shown

in [97]. The difference between FEM and CutFEM lies in the fact that FEM requires to generate a mesh conformed to the boundary of the domains. This can be a difficult task and CutFEM removes this need. In CutFEM, we describe the boundaries implicitly through a level set function [170, 206] that can be extracted from images. In particular, the level set function Φ is a scalar function that has negative values inside the domain, positive outside and zero on the boundary of the object. We obtained the level set, Φ, of the final segmented image f solving the following system in the domain B which is a three dimensional box where we have mapped the image f:

$$\begin{cases} -\epsilon^2 \triangle \Phi + \Phi = f & \text{in } B \\ \nabla \Phi \cdot n = 0 & \text{on } \partial B \end{cases}$$

where ϵ is a smoothing parameter that we set to 0.001. This step smooth the boundary of the cells to reduce the mesh size and related computational complexity respectively. In Supplementary Fig. B.1, we show the regular background mesh of finite element covering the two astrocytic domains. To solve the weak formulation of the RDS using CutFEM, we define the fictitious domain as all the cells of the background mesh that have a non-zero intersection with the cellular domain (Supplementary Fig. B.3). We apply a ghost-penalty stabilisation term [57] to all the edges that are intersected by the interface and all the edges that connect the intersected cells with the interior of the cellular domain. These stabilisation terms extend the solution from the physical domain Ω onto the fictitious domain. This is of fundamental importance to ensure the stability and accuracy of the numerical solution as the ghost-penalty stabilisation prevents ill-conditioning of the system matrices in case intersected cells contain very little of the cellular domain [58]. In this case, the linear system arising in the numerical experiments are solved using a direct (*MUMPS*) solver.

For further reading we address the reader to our previous work [97] and alternative proposed for enriched FEM [18, 38, 5, 3].

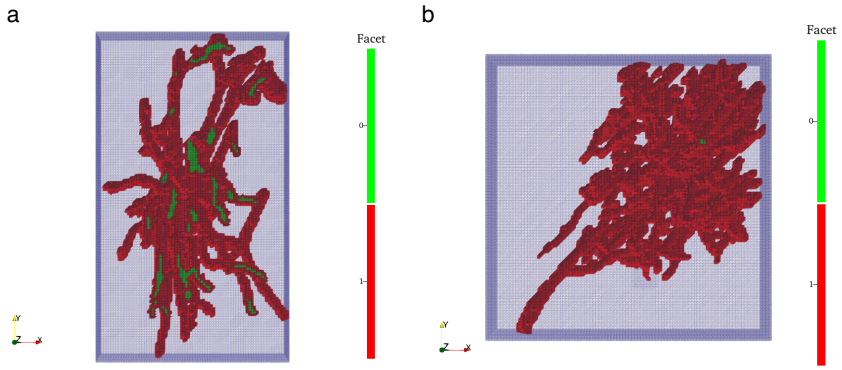

Fig. B.3 **Fictitious domain and facet markers for the two astrocytic morphologies.** Fictitious domain for the two astrocytic shape **a** control and **b** reactive, defined as the non-zero intersection of the finite elements with the cellular domain. We apply the stabilization term to the facets marked in red.

B.8 Numerical Parameters

The parameters used for the 2D experiments are presented in Supplementary Table B.3 and for the 3D experiments in Supplementary Table B.4. The penalty parameter γ used to ensure stability on the cut cells is set to 0.1. Convergence study were done extensively in the 2 dimensional experiments.

2D Numerical parameters				
geometry	# cells	# dofs	max cell diameter	Δt
circle	88768	44856 *	0.93	0.25
star	51046	26164 *	0.77	0.25
rectangle	25298	13207*	0.33	0.17

Table B.3 The table presents the numerical parameters used in the 2D experiments for the three domains: circle, star and rectangle. We show the number of cells in the finite element mesh, the number of degrees of freedom (dofs), the maximum diameter of the finite element cell and the time step used for the time discretisation. * In the table the number of dofs refers to one subspace. The total number of dofs for all the six subspaces is 269136 for the circle, 156984 for the star and 79242 for the rectangle.

3D Numerical parameters					
astrocyte	# cells in bg mesh	# cells on Ω	# dofs	max cell diameter	Δt
control	1000008	158938	37742	0.022	0.08
reactive	1301760	162579	39143	0.018	0.026

Table B.4 The table presents the numerical parameters used in the 3D experiments for the control and reactive astrocytes. We show the number of cells in the background finite element mesh, the number of cell covering the astrocyte domains Ω, the number of degrees of freedom (dofs), the maximum diameter of the finite element cell and the time step used for the time discretisation.

APPENDIX C

Supplementary Information 3

C.1 Fluxes

Fluxes used in Equation (5.5) are defined in Table C.1, taken from [225].

In Table C.1, V_{ref} is the volume of reference with respect to which each reaction rate, J_κ, and the corresponding entropy production rate, σ_κ, are normalised. Starting from the corresponding pseudoisomer concentrations, Magnus and Keizer [143] estimate that $\left[\text{ATP}^{4-}\right]_{\text{c}} = 0.05\ [\text{ATP}]_{\text{c}}$, $\left[\text{ATP}^{4-}\right]_{\text{m}} = 0.05\ [\text{ATP}]_{\text{m}}$, $\left[\text{ADP}^{3-}\right]_{\text{c}} = 0.45\ [\text{ADP}]_{\text{c}}$ and $\left[\text{ADP}^{3-}\right]_{\text{m}} = 0.36\ [\text{ADP}]_{\text{m}}$.

Table C.1 Fluxes of the system.

Process	V_{ref}	J_κ ($\text{mM}\,\text{s}^{-1}$)	**Ref**
ACO	V_m	$J_{\text{ACO}} = k_{\text{f}}^{\text{ACO}}\left([\text{CIT}]_{\text{m}} - \frac{[\text{ISOC}]_{\text{m}}}{K_{\text{ACO}}}\right)$	[73]
ANT	V_m	$J_{\text{ANT}} = V_{max}^{\text{ANT}} \frac{1 - \frac{[\text{ATP}^{4-}]_{\text{c}}}{[\text{ATP}^{4-}]_{\text{m}}}\frac{[\text{ADP}^{3-}]_{\text{m}}}{[\text{ADP}^{3-}]_{\text{c}}} e^{\frac{-\Delta\Psi}{RT}}}{\left(1+\frac{[\text{ATP}^{4-}]_{\text{c}}}{[\text{ADP}^{3-}]_{\text{c}}} e^{\frac{-f F\Delta\Psi}{RT}}\right)\left(1+\frac{[\text{ADP}^{3-}]_{\text{m}}}{[\text{ATP}^{4-}]_{\text{m}}}\right)}$	[143]
CS	V_m	$J_{\text{CS}} = \frac{V_{max}^{\text{CS}}}{1+\frac{K_{\text{M,AcCoA}}}{[\text{AcCoA}]_{\text{m}}} + \frac{K_{\text{M,OAA}}^{\text{CS}}}{[\text{OAA}]_{\text{m}}}\left(1+\frac{[\text{AcCoA}]_{\text{m}}}{K_{\text{i,AcCoA}}}\right) + \frac{K_{\text{s,AcCoA}} K_{\text{M,OAA}}^{\text{CS}}}{[\text{OAA}]_{\text{m}}[\text{AcCoA}]_{\text{m}}}}$	[84]
ERout	V_c	$J_{\text{ERout}} = \left(V_{max}^{\text{IP3R}} \frac{[\text{IP}_3]^2}{[\text{IP}_3]^2 + K_{\text{a,IP}_3}^2} \frac{\left[\text{Ca}^{2+}\right]_{\text{c}}^2}{\left[\text{Ca}^{2+}\right]_{\text{c}}^2 + K_{\text{a,Cac}}^2} \frac{K_{\text{i,Ca}}^4}{K_{\text{i,Ca}}^4 + \left[\text{Ca}^{2+}\right]_{\text{c}}^4} + V^{\text{LEAK}}\right)\left(\left[\text{Ca}^{2+}\right]_{\text{ER}} - \left[\text{Ca}^{2+}\right]_{\text{c}}\right)$	[129]
F1	V_m	$J_{\text{F1}} = -\rho_{\text{f1}} \frac{\left[p_a 10^{3\Delta\text{pH}} + p_{c1} e^{\frac{3F\Delta\Psi_B}{RT}}\right] A_{\text{F1}} - p_a e^{\frac{3F\Delta\Psi}{RT}} + p_{c2} A_{\text{F1}} e^{\frac{3F\Delta\Psi}{RT}}}{[1+p_1 A_{\text{F1}}] e^{\frac{3F\Delta\Psi_B}{RT}} + [p_2 + p_3 A_{\text{F1}}] e^{\frac{3F\Delta\Psi}{RT}}}$	[143]
		with $A_{\text{F1}} = K_{\text{F1}} \frac{[\text{ATP}]_{\text{m}}}{[\text{ADP}]_{\text{m}}[\text{Pi}]_{\text{m}}}$	
FH	V_m	$J_{\text{FH}} = k_{\text{f}}^{\text{FH}}\left([\text{FUM}]_{\text{m}} - \frac{[\text{MAL}]_{\text{m}}}{K_{\text{FH}}}\right)$	[73]
Hl	V_m	$J_{\text{Hl}} = g_{\text{H}}\left(\Delta\Psi - 2.303\frac{RT}{F}\Delta\text{pH}\right)$	[143]
Hyd	V_c	$J_{\text{Hyd}} = k_{\text{Hyd}} \frac{[\text{ATP}]_{\text{c}}}{[\text{ATP}]_{\text{c}} + K_{\text{M,ATPc}}}$	[227]
IDH	V_m	$J_{\text{IDH}} = \frac{V_{max}^{\text{IDH}}}{1+\frac{[\text{H}]_{\text{m}}}{k_{\text{h,1}}} + \frac{k_{\text{h,2}}}{[\text{H}]_{\text{m}}} + \frac{\left(\frac{K_{\text{M,ISOC}}}{[\text{ISOC}]_{\text{m}}}\right)^{n_i}}{\left(1+\frac{[\text{ADP}]_{\text{m}}}{K_{\text{a,ADP}}}\right)\left(1+\frac{[\text{Ca}^{2+}]_{\text{m}}}{K_{\text{a,Cam}}}\right)} + \frac{K_{\text{M,NAD}}^{\text{IDH}}}{[\text{NAD}]_{\text{m}}}\left(1+\frac{[\text{NADH}]_{\text{m}}}{K_{\text{I,NADH}}}\right) + \frac{\left(\frac{K_{\text{M,ISOC}}}{[\text{ISOC}]_{\text{m}}}\right)^{n_i} K_{\text{M,NAD}}^{\text{IDH}}}{[\text{NAD}]_{\text{m}}}\frac{\left(1+\frac{[\text{NADH}]_{\text{m}}}{K_{\text{I,NADH}}}\right)}{\left(1+\frac{[\text{ADP}]_{\text{m}}}{K_{\text{a,ADP}}}\right)\left(1+\frac{[\text{Ca}^{2+}]_{\text{m}}}{K_{\text{a,Cam}}}\right)}}$	[73]
KGDH	V_m	$J_{\text{KGDH}} = \frac{V_{max}^{\text{KGDH}}}{1+\frac{K_{\text{M,}\alpha\text{KG}}}{[\alpha\text{KG}]_{\text{m}}}\left(\frac{K_{\text{M,NAD}}^{\text{KGDH}}}{[\text{NAD}]_{\text{m}}}\right)^{n_{\alpha\text{KG}}}\left(1+\frac{[\text{Mg}^{2+}]_{\text{m}}}{K_{\text{D,Mg}}}\right)\left(1+\frac{[\text{Ca}^{2+}]_{\text{m}}}{K_{\text{D,Ca}}}\right)}$	[84]
MDH	V_m	$J_{\text{MDH}} = V_{max}^{\text{MDH}} \frac{[\text{MAL}]_{\text{m}}[\text{NAD}]_{\text{m}} - \frac{[\text{OAA}]_{\text{m}}[\text{NADH}]_{\text{m}}}{K_{\text{MDH}}}}{\left(1+\frac{[\text{MAL}]_{\text{m}}}{K_{\text{M,MAL}}}\right)\left(1+\frac{[\text{NAD}]_{\text{m}}}{K_{\text{M,NAD}}^{\text{MDH}}}\right) + \left(1+\frac{[\text{OAA}]_{\text{m}}}{K_{\text{M,OAA}}^{\text{MDH}}}\right)\left(1+\frac{[\text{NADH}]_{\text{m}}}{K_{\text{M,NADH}}}\right) - 1}$	[29]
NCX	V_m	$J_{\text{NCX}} = V_{max}^{\text{NCX}} \frac{e^{\frac{bF(\Delta\Psi - \Delta\Psi^*)}{RT}}}{\left(1+\frac{K_{\text{M,Na}}}{[\text{Na}^+]_{\text{c}}}\right)^n\left(1+\frac{K_{\text{M,Ca}}}{[\text{Ca}^{2+}]_{\text{m}}}\right)}$	[143]
Ox	V_m	$J_{\text{Ox}} = \frac{1}{2}\rho_{\text{res}} \frac{\left[r_a 10^{6\Delta\text{pH}} + r_{c1} e^{\frac{6F\Delta\Psi_B}{RT}}\right] A_{\text{res}} - r_a e^{\frac{g6F\Delta\Psi}{RT}} + r_{c2} A_{\text{res}} e^{\frac{g6F\Delta\Psi}{RT}}}{[1+r_1 A_{\text{res}}] e^{\frac{6F\Delta\Psi_B}{RT}} + [r_2 + r_3 A_{\text{res}}] e^{\frac{g6F\Delta\Psi}{RT}}}$	[143]
		with $A_{\text{res}} = K_{\text{res}}\sqrt{\frac{[\text{NADH}]_{\text{m}}}{[\text{NAD}]_{\text{m}}}}$	
SDH	V_m	$J_{\text{SDH}} = \frac{V_{max}^{\text{SDH}}}{1+\frac{K_{\text{M,SUC}}}{[\text{SUC}]_{\text{m}}}\left(1+\frac{[\text{OAA}]_{\text{m}}}{K_{\text{i,OAA}}}\right)\left(1+\frac{[\text{FUM}]_{\text{m}}}{K_{\text{i,FUM}}}\right)}$	[73]
SERCA	V_c	$J_{\text{SERCA}} = V_{max}^{\text{SERCA}} \frac{\left[\text{Ca}^{2+}\right]_{\text{c}}^2}{\left[\text{Ca}^{2+}\right]_{\text{c}}^2 + K_{\text{Ca}}^2} \frac{[\text{ATP}]_{\text{c}}}{[\text{ATP}]_{\text{c}} + K_{\text{ATPc}}}$	[227]
SL	V_m	$J_{\text{SL}} = k_{\text{f}}^{\text{SL}}\left([\text{SCoA}]_{\text{m}}[\text{ADP}]_{\text{m}}[\text{Pi}]_{\text{m}} - \frac{[\text{SUC}]_{\text{m}}[\text{ATP}]_{\text{m}}[\text{CoA}]_{\text{m}}}{K_{\text{SL}}}\right)$	[229]
MCU	V_m	$J_{\text{MCU}} = V_{max}^{\text{MCU}} \frac{2F(\Delta\Psi - \Delta\Psi^*)}{RT\left(1 - e^{-\frac{2F(\Delta\Psi - \Delta\Psi^*)}{RT}}\right)} \frac{\frac{\left[\text{Ca}^{2+}\right]_{\text{c}}}{K_{\text{trans}}}\left(1+\frac{\left[\text{Ca}^{2+}\right]_{\text{c}}}{K_{\text{trans}}}\right)^3}{\left(1+\frac{[\text{Ca}^{2+}]_{\text{c}}}{K_{\text{trans}}}\right)^4 + \frac{L}{\left(1+\frac{[\text{Ca}^{2+}]_{\text{c}}}{K_{\text{act}}}\right)^{na}}}$	[143]
PyrEx		$J_{\text{PyrEx}} = V_{\text{max}}^{\text{PyrEx}} \frac{([\text{PYR}]_c[\text{H}]_c - [\text{PYR}]_m[\text{H}]_m)}{(1+\frac{[\text{PYR}]_c}{K_{M,\text{PYR}_c}})(1+\frac{[\text{PYR}]_m}{K_{M,\text{PYR}_m}^{\text{PyrEx}}})}$	[28, 29]
pdh		$J_{\text{pdh}} = V_{max}^{\text{pdh}}(1 + A_{max}^{\text{Ca}_m^{2+}} \frac{[\text{Ca}^{2+}]_m}{[\text{Ca}^{2+}]_m + K_{A,\text{Ca}_m^{2+}}})(\frac{[\text{PYR}]_m}{[\text{PYR}]_m + K_{M,\text{PYR}_m}^{\text{pdh}}})(\frac{[\text{NAD}]_m}{[\text{NAD}]_m + K_{M,\text{NAD}_m}})(\frac{[\text{CoA}]_m}{[\text{CoA}]_m + K_{M,\text{CoA}_m}})$	[28, 29]

C.2 Parameters

The parameters for the model have been chosen based on literature. The metabolic model's parameters are taken from our previous work shown in Table 4.1. The parameters used in [225] for the calcium model are presented in Table C.2.

Table C.2 Reference parameter values.

Parameter	Definition	Value (units)	Reference
α	Ratio between ER and cytosol volumes	0.10	[227]
A_{tot}	Total concentration of cytosolic adenine nucleotides	3 mM	[155]
$A_{\text{m,tot}}$	Total concentration of mitochondrial adenine nucleotides	15 mM	[143]
b	Dependence of electrogenic Na^+/Ca^{2+} exchanger on $\Delta\Psi$	0.5	[143]
C_m	Mitochondrial membrane capacitance	1.812×10^{-3} mM mV^{-1}	[73]
$[CO_2]$	Total CO_2 concentration in mitochondrial matrix	21.4 mM	[231]
[CoA]	CoA concentration in mitochondrial matrix	0.02 mM	[73]
[CoQ]	CoQ concentration in mitochondrial matrix	0.97 mM	[231]
$[CoQH_2]$	CoQ_2 concentration in mitochondrial matrix	0.38 mM	[231]
c_{tot}	Total free Ca^{2+} concentration of the cell normalised by V_c	1500 μM	[225]
c_{Ktot}	Total concentration of TCA cycle intermediates	1 mM	[73]
δ	Ratio between mitochondrial matrix and cytosol volumes	0.15	[208, 139]
ΔpH	pH difference between cytosol and mitochondrial matrix ($pH_c - pH_m$)	-0.80	[52, 63]
$\Delta\Psi^*$	Membrane potential offset for Ca^{2+} transport	91 mV	[143]
$\Delta\Psi_B$	Total phase boundary potential	50 mV	[143]
F	Faraday constant	96.485 kC mol^{-1}	
f	Fraction of $\Delta\Psi$ responsible for the behaviour of ANT in energised mitochondria	0.5	[143]
f_c	Fraction of free cytosolic Ca^{2+}	0.01	[227]
f_e	Fraction of free Ca^{2+} in the ER	0.01	[227]
f_m	Fraction of free mitochondrial Ca^{2+}	0.0003	[143]
γ	Conversion factor between mM and μM	1000 μM mM^{-1}	
g	Fitting factor for voltage in respiration rate	0.85	[143]
g_{H}	Ionic conductance of the mitochondrial inner membrane	10^{-5} mM mV^{-1} s^{-1}	[73]
$[H^+]_c$	Cytosolic proton concentration	6.31×10^{-5} mM	[52, 63]
$[H^+]_m$	Concentration of proton in the mitochondrial matrix	10^{-5} mM	[52, 63]
$K_{\text{a,Cac}}$	Activation constant of IP_3Rs for cytosolic Ca^{2+}	0.60 μM	[225]
K_{ACO}	Equilibrium constant of ACO	0.067	[103, 29]
K_{act}	Dissociation constant of mitochondrial uniporter for activating Ca^{2+}	0.38	[143]
K_{ATPc}	Dissociation constant of SERCA for cytosolic ATP	0.05 mM	[204, 155]
$K_{\text{a,ADP}}$	Activation constant of IDH for ADP_m	0.062 mM	[84, 73]
$K_{\text{a,Cam}}$	Activation constant of IDH for mitochondrial Ca^{2+}	1.41 μM	[73]
$K_{\text{a,IP}_3}$	Activation constant of IP_3Rs for IP_3	1.00 μM	[86, 227]
K_{Ca}	Dissociation constant of SERCA for Ca^{2+}	0.35 μM	[86, 227]
$K_{\text{D,Ca}}$	Dissociation constant of KGDH for mitochondrial Ca^{2+}	1.27 μM	[84, 73]
$K_{\text{D,Mg}}$	Dissociation constant of KGDH for mitochondrial Mg^{2+}	0.0308 mM	[73]
K_{F1}	Equilibrium constant for ATP hydrolysis in mitochondrial matrix	1.71×10^6	[180, 73]
K_{FH}	Equilibrium constant for FH	3.942	[103]
$k_{\text{f}}^{\text{ACO}}$	Forward rate constant of ACO	12.5 s^{-1}	[73]
k_{f}^{FH}	Forward rate constant of FH	8.3 s^{-1}	[225]
k_{f}^{SL}	Forward rate constant of SL	0.127 mM^{-2} s^{-1}	[73]
$k_{\text{h,1}}$	First ionisation constant of IDH	8.1×10^{-5} mM	[84, 73]
$k_{\text{h,2}}$	Second ionisation constant of IDH	5.98×10^{-5} mM	[84, 73]
k_{Hyd}	Hydrolysis rate of ATP_c due to cellular activity	0.088 mM s^{-1}	This work
$K_{\text{i,AcCoA}}$	Inhibition constant of CS for AcCoA	3.7068×10^{-2} mM	[84]
$K_{\text{i,Ca}}$	Inhibition constant of IP_3Rs for cytosolic Ca^{2+}	1.00 μM	[225]
$K_{\text{i,FUM}}$	Inhibition constant of SDH for fumarate	1.3 mM	[73]
$K_{\text{i,OAA}}$	Inhibition constant of SDH for oxaloacetate	0.15 mM	[73]
$K_{\text{i,NADH}}$	Inhibition constant of IDH for NADH	0.19 mM	[73]

Table A2 (continued). Reference parameter values.

Parameter	Definition	Value (units)	Reference
$K_{\mathrm{M,AcCoA}}$	Michaelis constant of CS for acetyl-CoA	1.2614×10^{-2} mM	[84, 73]
$K_{\mathrm{M},\alpha\mathrm{KG}}$	Michaelis constant of KGDH for α-ketoglutarate	1.94 mM	[73]
$K_{\mathrm{M,ATPc}}$	Michaelis constant for $\mathrm{ATP_c}$ hydrolysis due to cellular activity	1 mM	[227]
$K_{\mathrm{M,Ca}}$	Michaelis constant of $\mathrm{Na^+/Ca^{2+}}$ exchanger for $\mathrm{Ca^{2+}}$	0.375 μM	[73]
$K_{\mathrm{M,ISOC}}$	Michaelis constant of IDH for isocitrate	1.52 mM	[84, 73]
$K_{\mathrm{M,MAL}}$	Michaelis constant of MDH for malate	0.145 mM	[29]
$K_{\mathrm{M,Na}}$	Michaelis constant of $\mathrm{Na^+/Ca^{2+}}$ exchanger for $\mathrm{Na^+}$	9.4 mM	[143]
$K_{\mathrm{M,NAD}}^{\mathrm{IDH}}$	Michaelis constant of IDH for NAD	0.923 mM	[84, 73]
$K_{\mathrm{M,NAD}}^{\mathrm{KGDH}}$	Michaelis constant of KGDH for NAD	3.87×10^{-2} mM	[225]
$K_{\mathrm{M,NAD}}^{\mathrm{MDH}}$	Michaelis constant of MDH for NAD	0.06 mM	[29]
$K_{\mathrm{M,NADH}}$	Michaelis constant of MDH for NADH	0.044 mM	[73]
$K_{\mathrm{M,OAA}}^{\mathrm{CS}}$	Michaelis constant of CS for oxaloacetate	5×10^{-3} mM	[148, 130, 29]
$K_{\mathrm{M,OAA}}^{\mathrm{MDH}}$	Michaelis constant of MDH for oxaloacetate	0.017 mM	[29]
$K_{\mathrm{M,SUC}}$	Michaelis constant of SDH for succinate	3×10^{-2} mM	[73]
K_{MDH}	Equilibrium constant of MDH	2.756×10^{-5}	[103]
K_{res}	Equilibium constant of $\mathrm{O_2}$ reduction by NADH in mitochondrial matrix	1.35×10^{18}	[143]
$K_{\mathrm{s,AcCoA}}$	Other binding constant of citrate synthase for AcCoA	8.0749×10^{-2} mM	[84]
K_{SL}	Equilibrium constant for SL	0.724	[103]
K_{trans}	Dissociation constant of mitochondrial uniporter for translocated $\mathrm{Ca^{2+}}$	19 μM	[145]
L	Equilibrium constant for mitochondrial uniporter conformations	110	[145]
$[\mathrm{Mg^{2+}}]_{\mathrm{m}}$	Mg concentration in the mitochondrial matric	0.4 mM	[73]
n	Number of $\mathrm{Na^+}$ binding to electrogenic $\mathrm{Na^+/Ca^{2+}}$ exchanger	3	[143]
n_a	Mitochondrial uniporter activation cooperativity	2.8	[143]
$[\mathrm{Na^+}]_{\mathrm{c}}$	Cytosolic $\mathrm{Na^+}$ concentration	10 mM	[73]
$[\mathrm{Na^+}]_{\mathrm{m}}$	Mitochondrial $\mathrm{Na^+}$ concentration	5 mM	[81]
$n_{\alpha\mathrm{KG}}$	Hill coefficient of KGDH for αKG	1.2	[73]
n_i	Hill coefficient of IDH for isocitrate	2	[229]
N_{tot}	Total concentration of mitochondrial pyridine nucleotides	0.8 mM	[225]
$[\mathrm{O_2}]$	$\mathrm{O_2}$ concentration in mitochondrial matrix	2.6×10^{-5} M	[22]
p_1	Combination of elementary kinetic constants for the 6-state ATPase model	1.346×10^{-8}	[143]
p_2	Combination of elementary kinetic constants for the 6-state ATPase model	7.739×10^{-7}	[143]
p_3	Combination of elementary kinetic constants for the 6-state ATPase model	6.65×10^{-15}	[143]
p_a	Combination of elementary kinetic constants for the 6-state ATPase model	1.656×10^{-5} $\mathrm{s^{-1}}$	[143]
p_{c1}	Combination of elementary kinetic constants for the 6-state ATPase model	9.651×10^{-14} $\mathrm{s^{-1}}$	[143]
p_{c2}	Combination of elementary kinetic constants for the 6-state ATPase model	4.845×10^{-19} $\mathrm{s^{-1}}$	[143]
$[\mathrm{P_i}]_{\mathrm{c}}$	Inorganic phosphate concentration in cytosol	1 mM	[32]
$[\mathrm{P_i}]_{\mathrm{m}}$	Inorganic phosphate concentration in mitochondrial matrix	20 mM	[143]
R	Gas constant	8.314 J $\mathrm{mol^{-1}}$ $\mathrm{K^{-1}}$	
ρ_{fl}	Density of ATPase pumps	1.5	[225]
ρ_{res}	Density of $\mathrm{H^+}$ pumps in mitochondrial membrane	1.00	[225]
r_1	Combination of elementary kinetic constants for the 6-state respiration model	2.077×10^{-18}	[143]
r_2	Combination of elementary kinetic constants for the 6-state respiration model	1.728×10^{-9}	[143]
r_3	Combination of elementary kinetic constants for the 6-state respiration model	1.059×10^{-26}	[143]
r_a	Combination of elementary kinetic constants for the 6-state respiration model	6.394×10^{-10} $\mathrm{s^{-1}}$	[143]
r_{c1}	Combination of elementary kinetic constants for the 6-state respiration model	2.656×10^{-19} $\mathrm{s^{-1}}$	[143]
r_{c2}	Combination of elementary kinetic constants for the 6-state respiration model	8.632×10^{-27} $\mathrm{s^{-1}}$	[143]

Table A2 (continued). Reference parameter values.

Parameter	Definition	Value (units)	Reference
T	Temperature	310 K	[73]
V_{max}^{ANT}	Limiting rate of adenine nucleotide translocator (ANT)	15 mM s^{-1}	[73]
V_{max}^{CS}	Limiting rate of CS	52 mM s^{-1}	[225]
V_{max}^{IDH}	Limiting rate of IDH	0.15 mM s^{-1}	[225]
$V_{max}^{\mathrm{IP_3R}}$	Limiting release rate of Ca^{2+} through IP_3Rs	15 s^{-1}	[225]
V_{max}^{KGDH}	Limiting rate of KGDH	5 mM s^{-1}	[225]
V^{LEAK}	Leak rate of Ca^{2+} from ER	0.15 s^{-1}	[225]
V_{max}^{MDH}	Limiting rate of MDH	32 mM s^{-1}	[225]
V_{max}^{NCX}	Limiting rate of Na^{+}/Ca^{2+} exchanger	2×10^{-3} mM s^{-1}	[225]
V_{max}^{SDH}	Limiting rate of SDH	1 mM s^{-1}	[225]
V_{max}^{SERCA}	Limiting rate of SERCA pumps	0.12 mM s^{-1}	[227]
V_{max}^{MCU}	Limiting rate of mitochondrial uniporter	0.30 mM s^{-1}	[225]

The additional parameters to merge the two models are shown in Table C.3.

Table C.3 Reference parameter values.

Parameter	Definition	Value (units)	Reference
K_{M,PYR_c}	Michaelis constant of PyrEx for cytosolic pyruvate	0.15 mM	[29]
$K_{M,\mathrm{PYR}_m}^{\mathrm{PyrEx}}$	Michaelis constant of PyrEx for mitochondrial pyruvate	0.15 mM	[29]
$V_{\mathrm{max}}^{\mathrm{PyrEx}}$	Limiting rate of pyruvate exchanger	128 mM s^{-1}	[29]
$V_{\mathrm{max}}^{\mathrm{pdh}}$	Limiting rate of pdh	13.1 mM s^{-1}	[29]
$A_{\mathrm{max}}^{\mathrm{Ca}_m}$	Modulator factor for Ca^{2+} regulation	1.7	[28, 29]
K_{A,Ca_m}	Activation constant of pdh for mitochondrial Ca^{2+}	1.e-3 μM	[28, 29]
$K_{M,\mathrm{PYR}_m}^{\mathrm{pdh}}$	Michaelis constant of pdh for mitochondrial pyruvate	0.090 mM	[28]
$K_{M,\mathrm{NAD}}$	Michaelis constant of pdh for NAD	0.036 mM	[28]
K_{M,CoA_m}	Michaelis constant of pdh for coa_m	0.0047 mM	[28, 29]
$[\mathrm{IP}^3]$	IP^3 concentration	0.5 μM	[225]

C.3 Initial Conditions

Th initial conditions have been selected using the one in [99, 225] as initial selection for the ODE system associated to the two models combined. We then selected initial conditions closer to the steady state oscillations (Table C.4).

Table C.4 Reference parameter values.

Species	**Definition**	**Value (units)**
GLC	Initial condition for cytosolic glucose	1.023e-01 mM
ATP_c	Initial condition for cytosolic ATP	2.79 mM
ADP_c	Initial condition for cytosolic ADP	3.05e-01 mM
GLY_c	Initial condition for cytosolic glycerhalderaide	5.20e-01 mM
PYR_c	Initial condition for cytosolic pyruvate	1.38e-01 mM
LAC_c	Initial condition for cytosolic lactate	2.75e+00 mM
PYR_m	Initial condition for mitochondrial pyruvate	1.87e-06 mM
$AcCoA_m$	Initial condition for mitochondrial acetyl coenzyme A	1.60e-07 mM
ADP_m	Initial condition for mitochondrial ADP	1.28e+01 mM
αKG	Initial condition mitochondrial α-ketoglutarate	6.65e-06 mM
ATP_m	Initial condition for mitochondrial ATP	2.15 mM
Ca_c^{2+}	Initial condition for cytosolic calcium	5.76e-01 μM
Ca_m^{2+}	Initial condition for mitochondrial calcium	1.62 μM
CIT_m	Initial condition for mitochondrial citrate	9.61e-02 mM
FUM_m	Initial condition for mitochondrial fumarate	1.36e-01 mM
ISOC	Initial condition for mitochondrial isocitrate	6.43e-03 mM
MAL_m	Initial condition for mitochondrial malate	5.36e-01 mM
$NADH_m$	Initial condition for mitochondrial NADH	5.70e-05 mM
NAD_m	Initial condition for mitochondrial NAD	7.99e-01 mM
OAA_m	Initial condition for mitochondrial oxaloacetate	2.25e-01 mM
$\Delta\psi$	Initial condition for membrane potential	1.02e+02 mM
$SCoA_m$	Initial condition for mitochondrial succinyl coenzyme A	1.67e-05 mM
SUC_m	Initial condition for mitochondrial succinate	4.41e-05 mM